Controlling, evading, and maximising quantum thermalisation

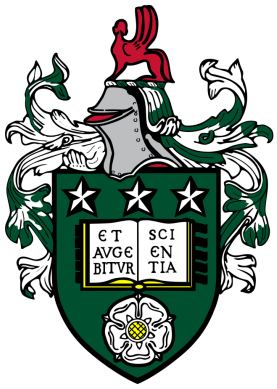

Aiden Luke Daniel

The University of Leeds
School of Physics and Astronomy

Submitted in accordance with the requirements for the degree of
Doctor of Philosophy

June, 2025

The candidate confirms that the work submitted is his own, except where work which has formed part of jointly-authored publications has been included. The contribution of the candidate and the other authors to this work has been explicitly indicated below. The candidate confirms that appropriate credit has been given within the thesis where reference has been made to the work of others.

Chapter 3 of this thesis includes work appearing in

- Aiden Daniel, Andrew Hallam, Matthew D. Horner, and Jiannis K. Pachos. Optimally scrambling chiral spin-chain with effective black hole geometry *Scientific Reports*, 15(1), March 2025.

In this paper, I presented the preliminary results. Computed and analysed all the numerical results. Contributed to writing all sections of the manuscript except sections detailing the analytical derivation of black hole geometry, and was involved in all aspects of the research.

Chapter 3 of this thesis includes work appearing in

- Aiden Daniel, Tanmay Bhore, Jiannis K. Pachos, Chang Liu, and Andrew Hallam. Quantum teleportation between simulated binary black holes. arXiv:2503.10761, March 2025

In this paper, I presented the preliminary results and performed all calculations and numerics related to the Hayden-Preskill protocol. Contributed to the discussion in every aspect of the paper and writing the first draft. I also contributed to the final draft of the research.

The background of the PXP model in Chapter 4 of this thesis includes work appearing in

- Jean-Yves Desaules, Kieran Bull, Aiden Daniel, and Zlatko Papić. Hypergrid subgraphs and the origin of scarred quantum walks in the many-body Hilbert space. *Physical Review B*, 105(24), June 2022.

In this paper, I carried out research into the relevant background literature of the research and verified numerical results regarding the hypergraph structure of PXP. I also verified and computed results related to the 2-3 model. Finally I contributed to redaction of the final draft of the manuscript.

Chapter 4 of this thesis includes work appearing in

- Aiden Daniel, Andrew Hallam, Jean-Yves Desaules, Ana Hudomal, Guo-Xian Su, Jad C. Halimeh, and Zlatko Papić. Bridging quantum criticality via many-body scarring. *Physical Review B*, 107(23), June 2023

In this paper, I computed the draft numerical results and wrote the original draft of the manuscript. Computation and analysis of the phase diagram results. I also contributed to writing the final draft of all aspects of the manuscript.

Chapter 5 of this thesis includes work from

- Aydin Deger, Aiden Daniel, Zlatko Papić, and Jiannis K. Pachos. Persistent non-Gaussian correlations in out-of-equilibrium Rydberg atom arrays. *PRX Quantum*, 4(4), December 2023.

In this paper, I contributed to research and numerical simulation of the manuscript. I verified all numerical simulations of the original results. Provided numerical data for all results except the original Gaussianity phase diagram results. Contributed to writing the final draft of the manuscript in all sections.

Acknowledgments

I would like to start by thanking my supervisors, Zlatko Papić and Jiannis Pachos, for the generous time, wisdom, and consideration they provided. The advice and knowledge they've given has shaped me and will always be invaluable. I would also like to thank all my collaborators and colleagues throughout my research, whose insight and tremendous resolve pushed me to be better.

It would be an injustice not to thank my loving parents. While they might not quite understand the physics I do, they have never hesitated in their support, care, and attention. Their love has never faltered and without them, I would never have been able to begin my journey through university. They've provided me with the life they never had, and for that I am truly grateful.

I would also like to thank my partner, Ida, for the unending love and support she has given me throughout my degree. Words fail to express how fortunate and thankful I am. My time throughout the degree would not have been the same without her.

Last, but not least, it would feel wrong not to thank my little ginger cat, Todd, who was there for over half of my life but passed away near the start of my degree. Thanks for everything buddy.

Publications

- Jean-Yves Desaules, Kieran Bull, Aiden Daniel, and Zlatko Papić. Hypergrid subgraphs and the origin of scarred quantum walks in the many-body Hilbert space. *Physical Review B*, 105(24), June 2022.
- Aiden Daniel, Andrew Hallam, Jean-Yves Desaules, Ana Hudomal, Guo-Xian Su, Jad C. Halimeh, and Zlatko Papić. Bridging quantum criticality via many-body scarring. *Physical Review B*, 107(23), June 2023
- Aydin Deger, Aiden Daniel, Zlatko Papić, and Jiannis K. Pachos. Persistent non-Gaussian correlations in out-of-equilibrium Rydberg atom arrays. *PRX Quantum*, 4(4), December 2023.
- Aiden Daniel, Andrew Hallam, Matthew D. Horner, and Jiannis K. Pachos. Optimally scrambling chiral spin-chain with effective black hole geometry *Scientific Reports*, 15(1), March 2025.
- Aiden Daniel, Tanmay Bhore, Jiannis K. Pachos, Chang Liu, and Andrew Hallam. Quantum teleportation between simulated binary black holes. arXiv:2503.10761, March 2025

Abstract

Quantum thermalisation is the process by which generic interacting many-body systems evolve such that local observables relax to their thermal equilibrium values, regardless of the system's initial state. While progress has been made through the Eigenstate Thermalisation Hypothesis – a powerful conjecture describing thermalisation in closed quantum systems – practical methods to control or exploit this process remain elusive. This is a crucial challenge if we aim to use interacting many-body systems as a foundation for quantum technologies. After providing introduction to quantum thermalisation and many-body chaos in Chapters 1-2, the core of this thesis explores theoretical frameworks for controlling quantum thermalisation using tunable quantum systems, with a strong emphasis on experimental realisability. In Chapter 3, we introduce a chiral spin-chain model and demonstrate that, when tuned to the appropriate coupling regime, it exhibits maximally thermalising behaviour, similar to the well-known Sachdev-Ye-Kitaev model. Leveraging this property, we implement the Hayden–Preskill teleportation protocol, showing that maximal scrambling can improve the protocol's timescales. In Chapter 4, we step back and introduce quantum many-body scarring as a mechanism for evading thermalisation. We showcase how the PXP model – a limit of the experimentally realised Rydberg atom platform – allows for tunable quantum many-body scars by means of varying the detuning or chemical potential. This approach unveils a continuous family of scarred initial states that extends beyond low-entangled product states. Finally, in Chapter 5, we investigate a distinct information-scrambling process – "Gaussification". In this process, which bears some resemblance to thermalisation, the states which are initially interacting, i.e., possess non-Gaussian correlations and violate Wick's theorem, progressively evolve into Gaussian ones. We demonstrate that Rydberg atom arrays can retain non-Gaussian correlations after a quantum quench in a way that is robust against experimental errors. Our conclusions are presented in Chapter 6 where we argue that the results presented in this thesis challenge the notion that thermalisation is an inevitable destructive force by offering several strategies to both resist it and harness it for applications in quantum-information processing.

Contents

List of Figures

List of Abbreviations

ETH	Eigenstate thermalisation hypothesis
QMBS	Quantum many-body scar
DOS	Density of states
TDVP	Time-dependent variational principle
OTOC	Out-of-time order correlators
PBC	Periodic boundary conditions
OBC	Open boundary conditions
ED	Exact diagonalisation
MPS	Matrix product state
MF	Mean field
H.c	Hermitian conjugate
TEBD	Time-evolving block decimation
GOE	Gaussian orthogonal ensemble
GUE	Gaussian unitary ensemble
GSE	Gaussian symplectic ensemble
EPT	Equilibrium phase transition
1D	One-dimensional
2D	Two-dimensional

Chapter 1

Introduction

1.1 Motivation

Thermalisation is a fundamental area of research, with chaos often regarded as a driving force of the universe. However, the continuous growth of entropy and ultimate loss of information in a generic system still presents several open questions. One particularly compelling question is: to what extent do closed quantum many-body systems thermalise? From a classical perspective, the idea of memory loss in quantum systems appears paradoxical, given the unitary nature of quantum dynamics.

An effort to address this question was first presented by Deutsch and Srednicki through the Eigenstate Thermalisation Hypothesis (ETH) [1,2]. ETH proposes thermalisation in quantum mechanical systems is defined with respect to the eigenstates. While rigorous analytical proof remains elusive and current evidence is largely empirical, it has proven to be a powerful conjecture used to accurately underpin the nature of chaos in a wide variety of interacting many-body quantum systems [1–5]. ETH surmises that for generic interacting quantum many-body systems, measurable observables tend towards their thermal value predicted by a Gibbs ensemble (while still conserving energy) and remain near those values over time, irrelevant of initial state. In this way, a quantum system effectively loses memory of its initial wavefunction over time, mirroring its classical analogue. For quantum technologies, particularly quantum computing, preserving coherence over time is essential. Thus, the inevitable onset of thermalisation in interacting systems poses a significant challenge, motivating the search to understand thermalisation in a quantum setting and methods to control it. Beyond practical implications, the process of quantum thermalisation is also of fundamental interest in the context of understanding quantum gravity and quantum black holes. In particular, black holes are expected to act as maximally thermalising systems, as shown by the black hole information paradox [6,7].

To that end, several questions arise. First, to what extent can a quantum system be

thermal? If thermalisation is indeed inevitable, can the inherent thermality of a quantum system be utilised in a practical setting? Second, is it possible to evade thermalisation? Extremal solutions to the latter problem exist, such as integrable systems or many-body localisation; however, these are either fine-tuned or limited to systems in one spatial dimension. This thesis explores the following challenge: how does one control quantum thermalisation in generic, interacting many-body systems that lack special symmetry structure, such as integrability? In particular, we investigate how thermalisation can be both maximised and evaded in the setting of interacting spin systems, with a particular emphasis on experimental realisability.

A well-established method of quantifying 'thermality' in a quantum system is through out-of-time-order correlators, which serve as a powerful tool to unify concepts of quantum ergodicity and information scrambling [8–10]. The extent to which these correlators spread over time quantifies thermality in the system by extracting a Lyapunov exponent – an approach reminiscent of classical chaos. An upper bound on the Lyapunov exponent has been rigorously established for quantum many-body systems [11], thereby defining what it means for a system to be "maximally thermal". An important question is what types of physical systems saturate this bound. Classically, black holes are believed to be the ultimate scramblers of information. Thus, any quantum system claiming to emulate a black hole should exhibit maximally thermal behaviour and saturate the bound on chaos.

In this work, we explore a realisation of maximal chaos in Chapter 3 by taking the recently proposed chiral spin-chain model [12, 13], which takes the form

$$H_{\text{Chiral}} = \frac{1}{2}\sum_{i=1}^{N}\left[-u\left(S_i^x S_{i+1}^x + S_i^y S_{i+1}^y\right) + \frac{v}{2}\boldsymbol{S}_i \cdot \boldsymbol{S}_{i+1} \times \boldsymbol{S}_{i+2}\right], \tag{1.1}$$

where u and v are real numbers and $\boldsymbol{S}_i = (\sigma_i^x/2, \sigma_i^y/2, \sigma_i^z/2)$ with σ_i^α $(\alpha = x, y, z)$ is the α-Pauli matrix of the ith spin. The second term in Eq. (1.1) will be denoted as the chiral term:

$$\chi_i = \boldsymbol{S}_i \cdot \boldsymbol{S}_{i+1} \times \boldsymbol{S}_{i+2}. \tag{1.2}$$

In the chiral phase, when $v > 2u$, the system effectively describes Dirac fermions in a black hole background geometry. As a result, we expect the model to exhibit maximal information scrambling in the quantum sense. We find that as the model parameters are tuned from the non-chiral to the chiral phase, the Lyapunov exponent behaviour transitions from free to one that saturates the bound on chaos. This behaviour demonstrates that our chiral model provides a tunable and experimentally accessible platform for accessing a maximally thermal quantum system. Also, unlike other maximally scrambling

models – such as the SYK model – the model is both local and is not based on disordered couplings, enhancing its experimental feasibility.

In fact, the property of maximal thermalisation also makes the model (Eq. (1.1)) an ideal candidate for implementing the Hayden-Preskill teleportation protocol [14]. Although maximal thermalisation might initially appear detrimental to quantum information protocols, scrambling is, in this case, used to improve the fidelity of the teleportation. A striking consequence emerges from implementing the teleportation protocol due to the chiral models underlying black hole geometry. Remarkably, the required choice of couplings allows the protocol to be interpreted as a qubit teleporting between a binary black hole system. This, alongside key features of the chiral model such as Hawking radiation and optimal scrambling, offers a compelling motive for experimentally studying the protocol. Ultimately, these findings provide a controllable and practical means of accessing and leveraging maximal thermalisation in quantum systems.

In generic chaotic systems, robust state transfer that resists thermalisation is expected to be exceptionally rare, if not impossible. Nevertheless, as recent experiments on arrays of Rydberg atoms have shown [15–17], a potential solution to evading thermalisation may lie in systems that display "quantum many-body scarring". Here, a select few initial states were found to evade thermalisation and retain memory of their initial wavefunction over time, despite the presence of interactions in an otherwise thermalising system. The driving force behind this phenomena is a small subset of non-thermal eigenstates embedded in the energy spectrum [18–22]. These special eigenstates were shown to approximately form an emergent su(2) algebra [23,24], leading to near-equal energy spacing between them. As a result, quantum states with predominant overlap on this subspace exhibit atypical, non-thermalising dynamics. This is the core of quantum many-body scarring, a many-body analogue of the single-particle scarring phenomenon observed in chaotic billiard systems [25]. Despite several experimental studies [16, 17, 26–28], it remains natural to question whether scarring is a finely-tuned, fragile phenomenon and how accessible these select initial states truly are.

Here, we consider a limiting case of the experimentally accessible Rydberg model: the detuned PXP model in Chapter 4, where we demonstrate the ubiquity of many-body scarring. The PXP model is defined by the Hamiltonian

$$H_{\mathrm{PXP}}(\mu) = \Omega \sum_{j=0}^{N-1} P_{j-1}\sigma_j^x P_{j+1} + \mu \sum_{j=0}^{N-1} n_j, \tag{1.3}$$

where Ω is the Rabi frequency and μ is the chemical potential. The projector onto the Rydberg ground state is defined as $P_j = (1-\sigma_j^z)/2$, while $n_j = 1-P_j = (1+\sigma_j^z)/2$ projects onto the Rydberg excited state. Notably, due the chemical potential term, the detuned

PXP model hosts a quantum phase transition which leads one to question the interplay between quantum criticality and quantum many-body scarring. Quantum criticality is typically associated with ground-state physics while many-body scarring involves atypical dynamics stemming from mid-spectrum eigenstates. At first glance, these two phenomena may seem unrelated. However, recent investigations into the PXP model suggest that scarring may break down in the critical regime of PXP [29], highlighting the need for further study.

We address the previous questions by constructing a "scarring phase diagram", identifying families of experimentally accessible ground states that lead to scarring under continuous deformation of the model's parameter, μ/Ω. This provides a concrete and robust protocol for exploring tunable scarring regimes in the lab. Our findings further reveal that scarring is accessible from a wide variety of initial conditions – not just low-entangled product states, as considered in previous work. In particular, we uncover scarring from a highly-entangled critical ground state, thereby establishing a connection between quantum criticality and many-body scarring. This demonstrates the robustness of scarring and serves as a new method for evading thermalisation in Rydberg atom platforms.

Intriguingly, a cousin process to thermalisation, known as Gaussification, has also been numerically observed in fermionic systems, including the critical Ising chain [30] and – as we will showcase – Rydberg atom arrays [31]. Gaussification is a form of quantum information scrambling in which closed systems – often governed by non-interacting Hamiltonians – rapidly relax to Gaussian states, irrespective of their initial conditions [30,32]. A Gaussian state in this context refers to a non-interacting, uncorrelated state whose parent Hamiltonian is quadratic [33]. Therefore – much like thermalisation – in systems with a Gaussian ground state, non-Gaussian states tend to lose memory of their initial wavefunction and correlations over time. Given the rich phase structure of the Rydberg model, several regimes support a Gaussian ground state, making Gaussification equally prevalent. This proves detrimental as non-Gaussian states are crucial for universal quantum computing, enhancing a range of key quantum information protocols such as quantum teleportation, sensing, metrology, and communication [33–45]. As such, the decoherence of these states due to Gaussification poses a significant challenge.

We demonstrate in Chapter 5 that Rydberg platforms not only offer a means to evade thermalisation, but also Gaussification. To this end, we employ the so-called UV model – another limit of the Rydberg model closely related to detuned PXP by

$$H_{\mathrm{UV}} = H_{\mathrm{PXP}} + V \sum_{j=0}^{N} n_i n_{i+2}. \tag{1.4}$$

In contrast to PXP, we now allow for next-nearest neighbour interactions governed by V. This induces a much richer phase diagram into the model which is closer to that of the full Rydberg Hamiltonian. By quenching across specific regimes of the phase diagram, we observe persistent non-Gaussian correlations that resist both thermal and Gaussian equilibration. These correlations are found to be robust against experimental imperfections, making the protocol feasible in modern Rydberg platforms [15, 16, 46, 47]. These findings aim to highlight the versatility of Rydberg arrays as a powerful platform to evade scrambling processes.

In summary, the work in this thesis is guided by three primary motivations:

1. Can a *local* quantum system exhibit tunable maximal information scrambling? If so, can this scrambling be harnessed for practical quantum protocols?

2. How practical are quantum many-body scars as a mechanism to evade thermalisation? Can we demonstrate that scarring is more prevalent than previously assumed in models like PXP, and identify experimentally accessible regimes to robustly study it?

3. Can the strategies used to control thermalisation also be applied to experimentally access other information scrambling mechanisms, such as Gaussification?

1.2 Thesis outline

To address these motivations, we begin by introducing the broader background of quantum thermalisation. We then separate into three independent chapters, each dedicated to tackling one of the aforementioned general questions by including the related research and relevant background. The thesis is thus organised as follows.

Chapter 2

We begin in this chapter by outlining what it means to be thermal in a quantum system by introducing the Eigenstate Thermalisation Hypothesis. We also discuss how thermalisation can be diagnosed using a system's mean level statistics. Then, we explore the connection between thermalisation and black holes: specifically, how quantum models of black holes are expected to exhibit maximal scrambling of quantum information, motivated by the black hole information paradox. This leads to the need for a more precise measure of thermality in quantum systems – the Lyapunov exponent – which has a well-known upper bound, thereby quantifying what it means to be maximally thermal. We present the Sachdev-Ye-Kitaev (SYK) model, which saturates the bound on chaos and has a relation to black holes due to the notion of holographic duality. We finish this

chapter by introducing quantum many-body scarring – a mechanism that weakly violates ETH – as a means of evading thermalisation.

Chapter 3

In this chapter, the success of the SYK model serves as inspiration for investigating scrambling in the recently proposed chiral spin-chain model, which, like the SYK model, exhibits features reminiscent of black hole physics. We demonstrate that, by tuning the model parameters to the chiral phase (where the system mimics black hole physics), the system saturates the bound on chaos, therefore achieving maximal thermalisation. Having quantified the scrambling behaviour, we highlight how it can be harnessed to implement the Hayden-Preskill quantum teleportation protocol. The fast scrambling properties of the model allow us to optimise the protocol's performance while at the same time we can determine key quantities such as the butterfly velocity and the Page time. Finally, by comparing the chiral spin-chain model to other commonly chaotic local models – like the transverse field Ising model or the XY ladder – we illustrate its superiority in executing the protocol with greater efficiency and reduced timescales.

Chapter 4

Recently, the detuned PXP model – a limit of the Rydberg model – has been shown to host rich quantum many-body scarring. This provides a viable mechanism for evading thermalisation and introduces a new paradigm known as "weak" ergodicity breaking. In this chapter, we first begin by reviewing the phenomenology of quantum many-body scarring (QMBS) in the Rydberg model. Taking the strong Rydberg blockade limit, we investigate the extent of scarring in the PXP model and its connection with quantum criticality. In particular, we construct the dynamical phase diagram of the detuned PXP model under a quenched chemical potential and identify a continuous family of initial states that give rise to QMBS. We further demonstrate that this family can undergo a smooth evolution across the system's equilibrium phase transition, revealing scarring from the critical ground state of the PXP model. These results aim to address our second motivation by showing the ubiquity of scarring in the PXP model and highlighting its intriguing interplay with quantum criticality.

Chapter 5

In this chapter, we continue our investigation using the Rydberg model, focusing on a different limit known as the UV model – an extension of the PXP model that includes next-nearest-neighbour interactions. After introducing the concept of Gaussification, we

construct a "Gaussianity phase diagram" of the UV model similar to the previous scarring diagram, identifying regions characterised by Gaussian and non-Gaussian ground states. We then demonstrate that quenching from a non-Gaussian regime into a Gaussian one yields persistent non-Gaussian correlations. This behaviour is due to the evolution of the eigenspace overlap with the change in parameters following the global quench. While this analysis was conducted with the UV Hamiltonian, we find that these results hold even in the full Rydberg model, persisting with the addition of spatial disorder and single-site imperfections. These results directly support our third motivation, demonstrating that Rydberg platforms not only allow for the evasion of thermalisation, but also provide the necessary tools to evade other information-scrambling mechanisms like Gaussification.

Chapter 6

In this chapter, we briefly summarise our main findings and discuss future outlooks.

Chapter 2

Quantum thermalisation and maximising quantum chaos

In this chapter, we define what it means for a closed quantum system to be thermal and, in particular, for it to be *maximally* thermal – akin to the behaviour of a black hole. As a background for the remainder of the thesis, we first formulate the Eigenstate Thermalisation Hypothesis and introduce a common diagnostic of thermality in quantum systems: the energy level statistics and its similarity with a random matrix ensemble. Importantly, while level statistics are a useful tool for diagnosing thermalisation, they only offer a crude measure and do not quantify the degree of chaos present. To address this limitation, we utilise a concept from classical chaos theory: the Lyapunov exponent. To illustrate this, we review the non-local Sachdev-Ye-Kitaev (SYK) model [48–53] – a paradigmatic model known to exhibit maximal quantum chaos. We conclude this chapter by introducing a particular mechanism of weakly violating the ETH known as quantum many-body scarring [20–22,54]. The latter is responsible for a weak breakdown of thermalisation in Rydberg atom arrays, one of the central experimental platforms studied in this thesis.

2.1 Quantum thermalisation

Thermalisation is a fundamental physical process where systems naturally tend towards a state of thermal equilibrium through interactions. The continual growth of entropy and resulting loss of information due to thermalisation are fundamental phenomena, especially in the widely studied context of the black hole information paradox. However, a rigorous and universally accepted definition of thermalisation in quantum systems remains elusive. This lack of clarity poses a significant challenge for any quantum system aiming to emulate the behaviour of black holes. A valiant effort has been made through

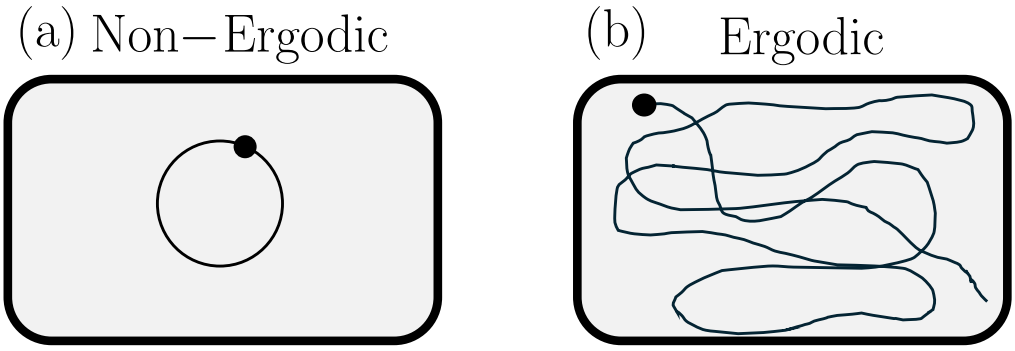

Figure 2.1: A sketch of the different trajectories possible in a classical phase space with a defined position and momenta coordinate. (a) A sketch of a (typically unstable) periodic trajectory found in non-ergodic systems. In such a system, the particle will remain in its orbit and consequently fail to explore the entirety of the phase space over time. (b) In contrast, an ergodic trajectory explores the whole phase space if given enough time, uniformly covering the space. As a result, values obtained by averaging over the trajectory over time can be equivalently obtained by averaging over the entire phase space.

the eigenstate thermalisation hypothesis which attempts to define what it is to be a thermalising quantum system.

2.1.1 Eigenstate thermalisation hypothesis (ETH) and Ergodicity

Before diving into what it means to be thermal quantum mechanically, it is useful to first consider its classical counterpart and, in particular, the notion of ergodicity as thermalisation and ergodicity are often used interchangeably. First, consider a Hamiltonian system with many degrees of freedom where points in phase space are characterised by $\mathbf{x} = (\mathbf{q}, \mathbf{p})$. Here, $\mathbf{q}$ and $\mathbf{p}$ are the generalised position and momentum respectively. The ergodic hypothesis states that, for an initial system at $\mathbf{q}_0$ with corresponding energy E_0, the system will explore *all* possible configurations with the same energy over a long period of time [55] – as sketched in Fig. 2.1. These will all be explored uniformly due to to Liouville's theorem [56]. As a consequence, for any local observable O, the long-time average is equal to the microcanonical average on all states with the same energy E_0. This is known as the ergodic principle and is more formally written as

$$\lim_{T\to\infty} \frac{1}{T} \int_0^T O(t)dt = \frac{\int_{\mathbf{x}\in MC} O(\mathbf{x})d\mathbf{x}}{\int_{\mathbf{x}\in MC} d\mathbf{x}} = O_{MC}. \tag{2.1}$$

MC is the microcanonical ensemble, where one assigns an equal probability to every microstate with equal energy, and T is the total time. Crucially, the average of the

microcanonical ensemble is irrelevant of any other details of the initial configuration and depends only on the energy, E_0.

With that, we can now begin thinking about the analogous statement in quantum systems. Consider a quantum system with a Hamiltonian H and N degrees of freedom whose eigenstates are $|E_k\rangle$ with corresponding energies E_k. A typical state of the system is denoted via the wavefunction $|\psi\rangle$ which has a corresponding energy $E_0 = \langle\psi| H |\psi\rangle$. The state will naturally evolve in time as $|\psi(t)\rangle = e^{-iHt} |H\rangle$ and any local operator $\hat{O}$ will have an expectation value of $O(t) = \langle\psi| \hat{O} |\psi\rangle$. Any state can be decomposed as a sum of the eigenstates of the system such that

$$|\psi\rangle = \sum_k c_k |E_k\rangle \tag{2.2}$$

where $c_k = \langle\psi|E_k\rangle$. With this, we can expand the expectation value $O(t)$ as

$$O(t) = \sum_j |c_j|^2 O_{jj} + \sum_{j\neq k} c_j^* c_k O_{jk} e^i (E_j - E_k)t, \tag{2.3}$$

where $O_{jk} = \langle E_j| \hat{O} |E_k\rangle$. If we assume that the eigenspectrum has no symmetries and therefore no special structure such as the clustering of states around certain energies or exact degeneracies, then at late times the phases of $e^i(E_j - E_k)t$ will cancel, leaving

$$\lim_{T\to\infty} \frac{1}{T} \int_0^T O(t)dt = \sum_j |c_j|^2 O_{jj}. \tag{2.4}$$

The diagonal term on the right hand side is typically known as the diagonal ensemble [57]. It is important to note that, for this to hold, we assume that $|\psi\rangle$ is generic in the sense that is does not have high overlap with only a small number of eigenstates which is typically the case for low entanglement states such as product states. The standard deviation of the energy of these states with respect to H will scale as $\sqrt{N}$ in contrast to the energy range of the full system scales as N. Therefore, for such generic states, there will be strong overlap with eigenstates within a small energy window relative to the full spectrum. The states in this energy window $[E_0 - \delta, E_0 + \delta]$ where $\delta \approx \sqrt{N}$ is the microcanonical ensemble.

By taking the result from Eq. (2.4) and using the ergodic hypothesis in Eq. (2.1), we can see that

$$\sum_j |c_j|^2 O_{jj} = O_{MC} = \frac{1}{M} \sum_{j\in MC} O_{jj}, \tag{2.5}$$

where the number of states in the microcanonical ensemble is denoted by M. This equation implies, much like the classical analogue, that the late-time value of any physical

observable only depends on the original energy of the state.

How to relate this quantum notion of ergodicity to quantum thermalisation, however, is a non-trivial question. In a closed quantum system – such as those we consider in this thesis – the classical notion of thermalisation becomes inadequate. Since the dynamics are unitary and the system lacks an external thermal bath, one might naively conclude that thermalisation is impossible. This necessitates a redefinition of what it means for an isolated quantum system to thermalise [1, 2, 21]. For such a system, thermalisation is defined with respect to the eigenstates of the Hamiltonian which are themselves classified as "thermal" or "non-thermal". In that sense, for Hamiltonians with thermal eigenstates, a subsystem of the initial state can effectively act as a thermal bath for the rest of the system. The ETH encapsulates this observation by asserting that individual eigenstates of the Hamiltonian encode thermal properties.

More specifically, it requires that the distribution of $|c_j|^2$ for all E_j in the energy window of the microcanonical ensemble must not matter. For this to be the case, O_{jj} in Eq. (2.5) must be equal to O_{MC} for all states within the energy window and this must hold for any different initial state as the energy window will move. As a result, both O_{MC} and O_{MC} must be smooth as a function of energy. This is ultimately the foundation of ETH – the equivalence between diagonal and microcanonical ensembles and the smooth variation of local observables of the eigenstates as one varies the energy.

A thermal system that obeys the ETH is expected to exhibit several properties [3–5]:

1. For a thermal system, the expectation values of local observables in mid-spectrum eigenstates are expected to be thermal, i.e., they are identical to the value calculated using the microcanonical ensemble. In other words, the excited eigenstates can be viewed as random vectors in the many-body Hilbert space, whose expectation values of physical observables are a smooth function of energy.

2. Regardless of the initial state (assumed to be sufficiently far from an eigenstate), when the system is left to evolve under the Hamiltonian dynamics, the observables are expected to approach their equilibrium value at late times. Moreover, they should remain stationary, with fluctuations suppressed exponentially in the thermodynamic entropy. The entropy is defined as the von Neumann entanglement entropy,

$$S = -\mathrm{Tr}\left(\rho_A \ln \rho_A\right), \tag{2.6}$$

   of the reduced density matrix, $\rho_A = \mathrm{Tr}_B|\psi\rangle\langle\psi|$, obtained by tracing out degrees of freedom belonging to one half of the chain (denoted B).

3. For a given eigenstate $|\psi\rangle$, the reduced density matrix, ρ_A, obtained by tracing out a large finite subsystem, is equal to the thermodynamic density matrix, $\rho_{\mathrm{th}} =$

$e^{-H_A/T}/\mathrm{Tr}(e^{-H_A/T})$, with an effective temperature, T, set by the energy of the state and H_A denoting the Hamiltonian restricted to the subsystem.

Notably, the fact that the eigenstates behave like random vectors (1), and the reduced density matrices are thermal (3), implies that the entanglement entropy, S (or S_E), of highly-excited eigenstates will scale with the volume of the system. Specifically, $S \propto L^d$ where L is the size of the subsystem and d is the spatial dimension of the system. This supports the intuition the eigenstates in a thermal Hamiltonian are highly-entangled, and that information becomes effectively irretrievable over time. For systems obeying the ETH, we generally expect *all* eigenstates – except the unique cases at the edge of the spectrum – to act thermal.

Consequently, any generic initial state can be viewed as a superposition of such thermal eigenstates and entropy is expected to grow rapidly under quench dynamics. As the system approaches equilibrium, in line with the postulate (2), any sense of its initial wavefunction will be lost at late times. This mirrors classical thermalisation, where systems evolve toward memoryless equilibrium states, and is what it means to be strongly ergodic in a quantum sense. It was long believed that only maximal violations of the ETH could occur, through systems that are integrable or many-body localised [58, 59]. However, recent developments have introduced a new paradigm: the discovery of systems that weakly violate ETH through a mechanism known as quantum many-body scarring, as we discuss further at the end of this Chapter.

2.1.2 Measures of ergodicity and ergodic quantum systems

Having defined the properties exhibited by thermal Hamiltonians, a natural question arises: how can one practically determine whether a given Hamiltonian is thermal? For this purpose, one can borrow tools from random matrix theory [60]. The notions of chaos are closely related to that of ergodicity and thermalisation, stemming from the fact that the eigenstates of thermal Hamiltonians can be thought of as random vectors. In thermalising systems, one expects level repulsion between adjacent energy levels [61], a hallmark of quantum chaos that can be systematically diagnosed. The chaotic nature of a Hamiltonian can thus be quantified by comparing its eigenspectrum to that of known random matrix ensembles in the same symmetry class [60].

For our purposes, there are three commonly used random matrix ensembles which were introduced by Wigner [62]. First, there is the Gaussian Orthogonal Ensemble (GOE) for rotationally-symmetric systems that are invariant under time-reversal. Such Hamiltonians can be represented by real symmetric matrices $H_{i,j} = H_{j,i}$. Secondly, the Gaussian Unitary Ensemble (GUE) is used for Hamiltonians that violate time-reversal invariance. In such cases, the Hamiltonians are Hermitian where $H_{i,j} = H^\dagger_{j,i}$. Finally

there is the Gaussian Symplectic Ensemble (GSE) for half-integer spin systems that are time-reversal invariant but break rotational symmetry.

For convenience, the GOE, GUE, and GSE ensembles can be classified by the Dyson index $\beta = 1$, $\beta = 2$, and $\beta = 4$ respectively [63]. Taking energy spacing between two consecutive eigenstates as $s_i = (E_{i+1} - E_i)$, it can be shown for the random matrix ensembles that the probability distribution of the energy spacing is given by

$$P(s) = s a_\beta e^{-s^2 b_\beta}, \tag{2.7}$$

with $a_1 = \pi/2$, $a_2 = 32/\pi^2$, $a_4 = 2^{18}/(3^6\pi^3)$, $b_1 = \pi/4$, $b_2 = 4/\pi$ and $b_4 = 64/(9\pi)$. Such a probability distribution is colloquially known as the Wigner-Dyson distribution or Wigner surmise.

Therefore, to decide whether a Hamiltonian is indeed thermal (or chaotic), one can take the distribution of the spacings of the energy eigenvalues and compare it to the expected Wigner-Dyson distribution depending on the system's symmetries. If a Hamiltonian is found to match this well, it can be labelled as thermal. In practice, however, it can often be tedious to use s as a diagnostic due to a need to "unfold" the spectrum. This is necessary to allow for a homogeneous density of states across the whole spectrum. An alternative quantity that we will more often employ instead of s is the level spacing ratio defined as

$$r_i = \frac{\min\{s_{i+1}, s_i\}}{\max\{s_{i+1}, s_i\}}, \tag{2.8}$$

such that $0 \leq r_i \leq 1$, irrelevant of the system studied [64, 65]. Similarly, one can also compute the Wigner-Dyson distribution in terms of r,

$$P(r) = \frac{2}{c_\beta} \frac{(r + r^2)^\beta}{(1 + r + r^2)^{1+r\beta/2}}, \tag{2.9}$$

where $c_1 = 8/27$, $c_2 = 4\pi/81\sqrt{3}$ and $c_4 = 4\pi/729\sqrt{3}$. In fact, with the use of r, one can take it a step further and compute the expected *average* level spacing ratio $\langle r \rangle$ for a given ensemble. Doing so, one finds approximately that $\langle r \rangle_{\beta=1} = 0.5307$, $\langle r \rangle_{\beta=2} = 0.5996$, and $\langle r \rangle_{\beta=4} = 0.6744$ [65]. Thus, for a given Hamiltonian, we typically numerically compute $P(r)$ and $\langle r \rangle$ and compare these to the expected values for a random ensemble in order to see if the model indeed behaves like a random matrix. Meanwhile, for a non-chaotic system, one expects to find the Poisson distribution of level spacings and ratio, where $P(s) = e^{-s}$ $P(r) = e^{-r}$ and $\langle r \rangle = 0.3863$.

It is important to note another caveat when computing $P(r)$ in practice. One must be cautious of the effect of symmetries on the Hamiltonian. It is expected that for a chaotic Hamiltonian, the number of symmetries should remain small and finite, independent of

the system size, however, there may still exist a select few such as translational symmetry or some discrete spatial symmetries. In this case, one must reduce down to the symmetry sectors of a Hamiltonian with a fixed value for the conserved quantum numbers. Only then can we expect to truly see a Wigner-Dyson distribution due to the level repulsion existing within a given symmetry sector, and not between them.

2.2 From thermalisation to scrambling

2.2.1 Quantum mechanics and black holes

When one considers a thermal system, an immediate example that often comes to thought is that of a black hole. Black holes pose direct challenges to our understanding of fundamental laws of nature. Central to these open questions is the black hole information paradox, first articulated by Stephen Hawking in the 1970s [6, 7]. According to general relativity, the gravitational pull of black holes is so intense that it creates a region known as the event horizon, beyond which information appears to be irretrievably lost. However, the unitarity of quantum mechanics suggests information cannot be destroyed, leading to the question of what happens to the information of an object that falls into a black hole. This apparent contradiction between quantum physics and general relativity has given rise to intense theoretical investigations and remains unresolved to this day.

This destructive disposition of information posed a great challenge for the idea of a quantum system that could emulate a black hole. Within the ETH framework, we understand how information can be irrevocably lost in a quantum system akin to the behaviour expected from the black hole information paradox. There is a caveat, however. In essence, black holes are the *ultimate* thermalising system. Thus far, we have discussed thermalisation in a quantum system as a binary property: a system either is or is not chaotic. In the thermodynamic limit (where system size $N \to \infty$), it is expected that all non-integrable models display Wigner-Dyson statistics. This begs the question: if a quantum mechanical system is chaotic, how chaotic is it? What is a maximally chaotic system? Only such a system could truly be representative of a quantum mechanical black hole [6, 7].

2.2.2 A bound on chaos

To more precisely categorise how chaotic a system is, we make use of the close relation between thermalisation and chaos. It is intuitive to consider a chaotic system of only two particles separated by distance $\delta(0)$ at time $t = 0$. As the system is chaotic, one expects

the distance between the particles to diverge exponentially over time such that

$$\delta(t) = e^{\lambda t}\delta(0). \tag{2.10}$$

This is known as the butterfly effect. The degree of chaos in the system can therefore be quantified by the parameter λ, dubbed the Lyapunov exponent after Aleksandr Lyapunov, which quantifies how quickly the system diverges from its initial state [66,67].

This idea can be extended to a quantum mechanical framework where λ is calculated through the decay of the out-of-time order correlators (OTOCs) [8–10] defined as

$$O_{n,m}(t) = \left\langle [W_n(t), V_m]^\dagger [W_n(t), V_m] \right\rangle = \mathrm{Tr}\left(\rho [W_n(t), V_m]^\dagger [W_n(t), V_m]\right). \tag{2.11}$$

Here, $W_n(t) = e^{-iHt}W_n e^{iHt}$, where W_n and V_n are local operators acting on sites n and m of a 1D chain governed by the Hamiltonian H. While ρ is typically taken as the density matrix, $\rho = e^{-\beta H}/\mathrm{Tr}(e^{-\beta H})$ with temperature $T = 1/\beta$, it can be an arbitrary initial state as well.

In the case when operators W and V are Hermitian, the OTOC simplifies to $O_{n,m}(t) = 1 - \mathrm{Tr}\,(\rho W_n(t)V_m W_n(t)V_m)$, where the constant term is often neglected. Similar to the classical case, this function in essence measures the spread of an operator over time when perturbed by another operator at a different position at a given temperature [11, 68]. Alternatively, from a thermalisation stand point, one could view it as the degree to which local operators become hidden over time, equivalent to that of a loss of memory of the initial conditions [9, 50, 69]. The leading order behaviour of the OTOCs is then given by an exponentially diverging function $e^{\lambda t}$, where one again quantifies the spread of correlations via the Lyapunov exponent, λ [11, 70–72]. Therefore, typically, the larger the value of λ, the more chaotic a system is.

A quantum system that emulates a black whole is then expected to maximise λ. This saturation value is well known for low temperatures and was first proposed by Maldacena, Shenker, and Stanford in [11], where it was found to be

$$\lambda_{\max} = J2\pi T, \tag{2.12}$$

with J being the overall energy scale of the system. This result is often referred to as the bound on chaos. Therefore, to identify whether a system maximally scrambles information, one can extract $\lambda(T)$ at low temperatures, fit λ vs T to a linear function and compare the gradient against $2\pi J$.

2.2.3 Maximal scrambling in the SYK model

Next, we present a quantum model that saturates the bound on chaos, thereby maximally scrambling information and serving as a quantum analogue of a black hole. This paradigmatic model at the intersection of quantum many-body and black hole physics is known as the Sachdev-Ye-Kitaev (SYK) model. The model is defined in terms of Majorana fermions, χ_i, which obey the canonical commutation relation $\{\chi_i, \chi_j\} = \delta_{ij}$. For N Majorana fermions, the SYK Hamiltonian is given by

$$H = \frac{6}{N^3} \sum_{i<j<k<l}^{N} J_{ijkl} \chi_i \chi_j \chi_k \chi_l, \tag{2.13}$$

where J_{ijkl} are random real coefficients, drawn from a Gaussian distribution with standard deviation $\sigma = J$ [49, 50, 73]. In the spin language, the SYK model can be mapped onto $N/2$ Pauli spin$-1/2$ operators given by

$$\chi_i \to \begin{cases} \left(\prod_{j<k} \sigma_j^z\right) \sigma_k^x, & i \text{ even} \\ \left(\prod_{j<k} \sigma_j^z\right) \sigma_k^y, & i \text{ odd} \end{cases} \tag{2.14}$$

through a Jordan-Wigner transformation where $k = \text{floor}(i/2)$.

The connection between the SYK model and black holes lies is rooted in the model's holographic duality via the AdS/CFT correspondence [74]. Specifically, a correspondence has been established between the low-temperature dynamics of the SYK model and a universal theory of near-extremal black holes, described by Jackiw–Teitelboim gravity [51, 74–76]. It has been directly shown that the bound on chaos is saturated in theories of quantum gravity and their holographic duals in [68]. As such, the SYK model is expected to be a prime example of a quantum model that exhibits optimal scrambling and maximally thermalising behaviour.

This saturation of the bound on chaos was demonstrated in [73]. Using the same methodology outlined in section. 2.2.2, one first computes the *regularised* OTOC for the SYK model of the form

$$\tilde{F}(t) = \left\langle \chi_i(t) \rho^{\frac{1}{4}} \chi_j(0) \rho^{\frac{1}{4}} \chi_i(t) \rho^{\frac{1}{4}} \chi_j(0) \rho^{\frac{1}{4}} \right\rangle, \tag{2.15}$$

where $i \neq j$ and $\rho = e^{-\beta H}$. Due to the random nature of the couplings, this quantity is also averaged of many realisations of the couplings. Eq. (2.15) is a simplification of Eq. (2.11) that arises when the operators are Hermitian with the addition that the density matrix is now evenly smeared across the four operators. The benefit of the regularised version is faster convergence in much smaller system sizes compared to the unregularised

version. In the large-N limit, however, both expressions are expected to yield equivalent results.

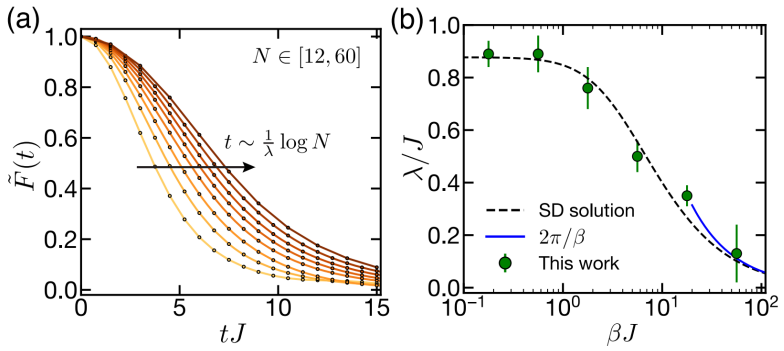

Figure 2.2: Computation of the regularised OTOCs in the SYK model and extraction of the Lyapunov exponent. (a) The early time behaviour of the regularised OTOC (Eq. (2.15)) over time (scaled by J) for different system sizes N. All system sizes are approximately related via a scaling relation, proportional to $\log(N)$. (b) By fitting an exponential-like function to $\tilde{F}(t)$, one can extract the Lyapunov exponent as a function of temperature $1/\beta$ (green dots). This is compared to the bound on chaos, Eq. (2.12), for low temperatures (blue line). Dashed black line indicates the solutions predicted from the Schwinger-Dyson equations, derived from the Green's functions in the large $N \to \infty$ limit. Figure reprinted from Ref. [73] with permission under the terms of the Creative Commons Attribution 4.0 International license.

For Eq.2.15, one expects a period of exponential decay over time analogous to the classical butterfly effect [71, 72] until the function eventually saturates due to a finite system size. The early-time behaviour of the OTOC is shown in Figure 2.2(a), where we see this expected behaviour and convergence with system size is clearly observed. From there, the Lyapunov exponent can be extracted by fitting an exponential-like function $\propto e^{\lambda t}/N$ to $\tilde{F}(t)$ for different temperatures. The results are shown in Figure. 2.2(b) alongside the bound on chaos (blue). As expected, the SYK model is found to saturate the bound on chaos, confirming its status as a maximally scrambling system – a hallmark of quantum black holes. This makes SYK a perfect candidate for a quantum representation of a black hole. The SYK model is not without its limitations, however. Being a non-local model, it poses significant challenges for experimental realisation in cold-atom platforms or quantum circuits [77]. For practical implementations and circuit-based descriptions, a local model with a black hole description, whose properties converge at smaller system sizes, would be most ideal. In the next chapter, we will present a local chiral spin-chain model that successfully captures a wide range of black hole properties, the most pertinent being the optimal scrambling behaviour.

2.3 Evading thermalisation through quantum scarring

Thus far, we have discussed quantum thermalisation in interacting many-body systems and what it means to maximally thermalise. However, our second goal is to explore tunable methods for evading thermalisation in such systems. Based on our previous discussion, this may seem unlikely due to the strong criteria imposed by the Eigenstate Thermalisation Hypothesis. In particular, ETH — through property (2) in Section 2.1.1 — suggests that all initial states are expected to undergo thermalisation. Nevertheless, since the 2017 experiments on Rydberg atom quantum simulators [16], it has become apparent that *weak* violations of the ETH are possible, such the system only violates the ETH with a small fraction of its states, while overall it still remains chaotic and its behaviour consistent with the ETH predictions.

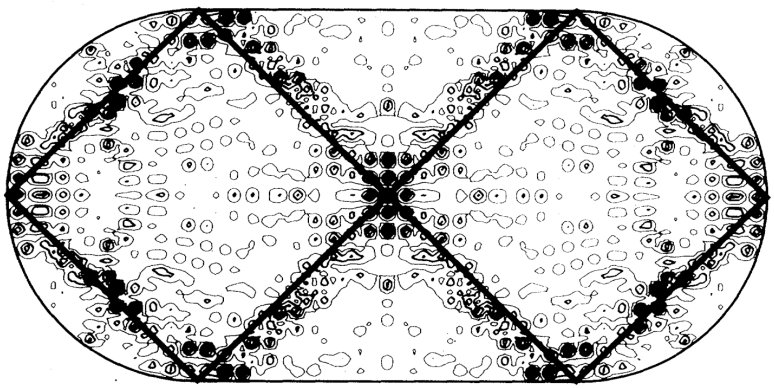

Figure 2.3: Quantum scarring of a single particle inside the Bunimovich stadium. The Hamiltonian is composed purely of the free-particle kinetic energy. Due to the geometry of the stadium, the particle generically exhibits chaotic behaviour. However, a select few eigenfunctions exist that have high support around unstable periodic trajectories that exist in the corresponding classical system (in this case, the diamond shown in the solid line). This is an example of a scarred eigenfunction which is indicated by the contours clustered around the periodic orbit. This figure is reprinted with permission from Ref. [25], American Physical Society.

An example of weak violation of thermalisation in *single-particle* systems was first identified by Heller in 1984 and dubbed *quantum scarring* [25]. Consider a billiard ball bouncing inside the Bunimovich stadium in Fig. 2.3. Due to the stadium geometry, most classical trajectories of such a ball are chaotic, lacking periodicity. Nevertheless, the classical system exhibits a few unstable periodic orbits [78], see the black line in Fig. 2.3.

A similar effect occurs in the quantum analogue of a free particle, described by the Schrödinger equation with the boundary conditions that match the stadium geometry. While most eigenstates in this system are ergodic – exhibiting probability distributions

that are uniformly spread across the billiard – a special subset of the wavefunctions show pronounced concentration around the unstable periodic orbits of the corresponding classical system. In this sense, the classical trajectories leave a 'scar' on quantum eigenstates, as illustrated in Fig. 2.3. This phenomenon has a profound effect on select initial states that have high overlap with the scarred eigenstates. Unlike generic initial states, which are expected to delocalise and uniformly spread over time, these special scarred initial states remain concentrated near the classical trajectory for an extended duration, seemingly resisting thermalisation.

2.3.1 Quantum many-body scarring

Quantum many-body scarring (QMBS) is a form of weak ergodicity breaking found in some chaotic many-body systems, reminiscent of the quantised billiards discussed above. In QMBS systems, a small number of atypical states retain memory of their initial conditions, defying the generic expectation of thermalisation (see recent reviews [20–22, 54]). As in the single-particle case, this behaviour originates from the state's significant overlap with a special subset of eigenstates embedded within the system's eigenspectrum. These are typically highly excited states that violate the ETH and are generally known as quantum many-body scars.

The number of scarred eigenstates typically scales polynomially with system size N, thus they form a vanishing fraction of the entire Hilbert space that grows exponentially with N. Because of this, systems exhibiting QMBS still display many hallmarks of quantum chaos, such as level repulsion and information scrambling. Nevertheless, scarred eigenstates are often approximately equally spaced in energy and have enhanced overlap on certain product states. Hence, when the system is initialised in such a product state, one can observe nearly-perfect revivals in the quench dynamics. Furthermore, the QMBS eigenstates also exhibit suppressed entanglement (subvolume law scaling), in contrast to the volume-law scaling typical of thermal bulk eigenstates.

The Hamiltonian of a large class of QMBS models can be expressed in the form

$$\mathcal{H} = \mathcal{H}_{\text{Thermal}} \oplus \mathcal{H}_{\text{Scar}} + \mathcal{V}, \tag{2.16}$$

where $\mathcal{H}_{\text{Scar}}$ denotes the Hamiltonian of the scarred subspace that violates the ETH, $\mathcal{H}_{\text{Thermal}}$ is the Hamiltonian of the (much larger) thermal subspace, and $\mathcal{V}$ denotes weak coupling between the two subspaces. This effective decoupling of the Hilbert space (for the special case $\mathcal{V} = 0$) is illustrated in Fig. 2.4(a). The decoupling in Eq. (2.16) is clearly not a feature of all chaotic models, therefore one may wonder about the possible underlying origins of such a decoupling.

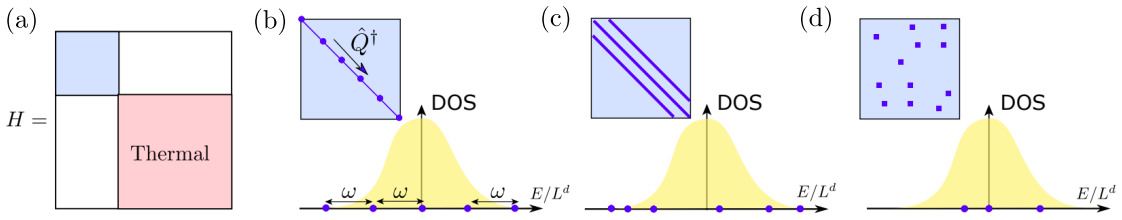

Figure 2.4: (a) Illustration of the Hamiltonian, $\mathcal{H}$, in Eq. (2.16) where the Hilbert space is split into a thermal subspace (red) and scar subspace (blue). (b)-(d) show the density of states (DOS) of $\mathcal{H}$ where the scarred eigenstates (blue dots) are highlighted within the continuum of thermal eigenstates. In particular, the plots schematically show the difference between three possible mechanisms of QMBS. (b) The DOS due to a spectrum generating algebra which embeds eigenstates in the spectrum with equidistant energy separation ω. (c) A disconnected subspace due to an exact Krylov subspace – represented with a tridiagonal matrix. (d) The DOS as a result of general projector embedding where the special eigenstates are sporadically placed throughout the eigenspectrum. Figure reprinted with permission from Ref. [20], Springer Nature Ltd.

In the single-particle case, the origin of scarred eigenstates can be traced back to unstable periodic orbits in the corresponding classical system. However, in the many-body context, no clear classical analogue exists to account for the emergence of such non-thermal eigenstates. Several mechanisms have been proposed to explain their presence: these include spectrum-generating algebras [23, 24, 79–82], Krylov-restricted thermalisation [83], and projector embedding [84]. Each of these mechanisms results in a special subset of non-thermal eigenstates embedded within an otherwise thermal spectrum, as schematically illustrated in Fig. 2.4(b)–(d).

For the spectrum generating algebra, one can define a local ladder operator, $Q^\dagger$, satisfying the relation $([H, Q^\dagger] - \omega Q^\dagger)W = 0$. Here ω is some energy scale and W is a subspace of the full Hilbert space that remains invariant under the action of $Q^\dagger$. Starting from a state $|\psi_0\rangle$ – for example, the ground state of H – one can construct a tower of states $|\psi_n\rangle = (Q^\dagger)^n |\psi_0\rangle$ which are eigenstates of H with equally spaced energies $E_0 + n\omega$ (for integer n). The eigenstates $|\psi_n\rangle$ are candidates for many-body scars due to their potentially non-thermal properties, despite being eigenstates of a globally chaotic Hamiltonian. Because of their equal spacing, any state formed as a superposition of these eigenstates will exhibit perfect revivals when evolved under H. This constitutes one way to effectively decouple a scarred subspace from the thermal bulk, as shown in Fig. 2.4(b).

Krylov restricted thermalisation is another method of disconnecting the subspace. Unlike the spectrum generating algebra, this method does not require prior knowledge of a ladder operator like $Q^\dagger$. Consider a general Hamiltonian H and an initial state $|\psi_0\rangle$.

By repeatedly acting H on $|\psi_0\rangle$, one generates the Krylov subspace

$$\mathcal{K} = \text{span}\left\{|\psi_0\rangle, H|\psi_0\rangle, H^2|\psi_0\rangle, ...\right\}. \tag{2.17}$$

In the special case where $\mathcal{K}$ is finite – i.e., there exists some n such that $H^n|\psi_0\rangle = 0$ – a dynamical fracture occurs in the Hilbert space. Any state $|v\rangle \in \mathcal{K}$ will then remain confined to this subspace under time evolution: $e^{-iHt}|v\rangle \in \mathcal{K}$. Through performing a Gram-Schmidt orthogonalisation, $\mathcal{K}$ can be transformed into a tridiagonal matrix, fully decoupled from the rest of the spectrum of H, see Fig. 2.4(c). This subspace can exhibit non-thermal behaviour. However, unlike the spectrum-generating algebra, the special eigenstates are not necessarily equally spaced in energy, so the dynamical revivals are not guaranteed.

Finally, a more systematic method for constructing a thermalising Hamiltonian with an embedded non-thermal subspace is projector embedding. This approach begins with an arbitrary set of non-thermal states $|\psi_i\rangle$ defining the scarred subspace as $H_{\text{Scar}} = \text{span}\{|\psi_i\rangle\}$. The goal is to then embed H_{Scar} into a thermalising Hamiltonian of the form shown in Eq. (2.16). Shiraishi and Mori [84] proposed such a means through projector embedding. This method assumes that each $|\psi_i\rangle$ are annihilated by local projectors P_i such that $P_i|\psi_i\rangle = 0$, where i indexes lattice sites. The Hamiltonian is then constructed as $H = \sum_i P_i h_i P_i + H'$, where h_i is an arbitrary local operator and H' a general Hamiltonian. Assuming that $\left[H', P_i\right] = 0$, it follows that $P_i H|\psi_i\rangle = P_i H'|\psi_i\rangle = H' P_i|\psi_i\rangle = 0$, so $[H, P_i] = 0$, and the Hamiltonian becomes block diagonal. With a suitable choice of H', the scarred states $|\psi_i\rangle$ can be embedded at arbitrary energies in the spectrum. As with the Krylov method, this construction produces a decoupled, non-thermal subspace – but again, it does not inherently lead to revivals, unlike the spectrum-generating algebra.

Numerous models exhibiting these scarring mechanisms have been identified, with several examples shown in Fig. 2.5. The catalogue of systems hosting QMBS states continues to grow rapidly [18,79,85–98], and includes experimental realisations in several cold atom platforms [16,17,26–28]. It is important to note that for non-thermal behaviour to persist, the embedded scarred subspace does not need to be perfectly decoupled from the rest of the Hilbert space, i.e., $\mathcal{V}$ can be non-zero in Eq. (2.16). A canonical example of this is the PXP model, which will be studied in detail in Chapter 4. Additionally, while these three frameworks offer an avenue for understanding the origin of scarred eigenstates, they are not exhaustive. The underlying origin of memory-retaining initial states ultimately remains the subject of on-going work. Moreover, the connection between quantum many-body scarring and its single-particle analogue, whose origin is better understood, is still not fully resolved. One promising approach to bridging this gap is through the time-dependent variational principle (TDVP), which will be discussed in

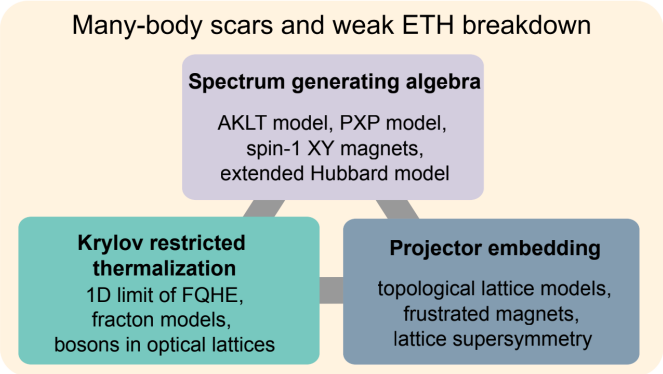

Figure 2.5: Three methods of generating a scarred subspace in a Hamiltonian and examples of models which exhibit each mechanism. Figure reprinted with permission from Ref. [20], Springer Nature Ltd.

Section. 4.2.3 in the context of the PXP model.

2.4 Chapter conclusions

In this chapter, we have explored what it is to be (maximally) thermal in a quantum setting and how this motivates condensed matter toy models of black holes. We began by defining thermalisation in quantum many-body systems and explaining how it can be diagnosed through the distribution of level statistics. We then introduced a more precise metric of thermality through the Lyapunov exponent, which is used to measure the degree of thermality in a system. Following this, we presented the SYK Hamiltonian as a paradigmatic example of a chaotic system, demonstrating how it saturates the upper bound on the Lyapunov exponent. In this sense, black holes are the ultimate scramblers of information, and so this saturation is an essential feature for any quantum system aiming to emulate black hole dynamics. We also reviewed a form of weak ergodicity breaking through quantum many-body scars – a mechanism for weakly violating the ETH and evading thermalisation using select initial states.

This background sets the foundation for the remainder of the thesis. In particular, in Chapter 3, we explore the idea of maximal thermalisation further by presenting a maximally scrambling chiral spin-chain model. Like the SYK model, the chiral spin-chain exhibits black hole phenomena due to an emergent effective black hole geometry in the continuum limit [12]. As a result, it is expected to manifest maximal scrambling behaviour. By analysing the saturation of the Lyapunov exponent, using the methodology established with the SYK model, we can assess whether this system exhibits maximal thermalisation. In contrast to the SYK model, this would provide a more experimentally

accessible route to maximal thermalisation due to being a disorder-free, local model.

Similarly, the definition of the ETH will enable us to investigate mechanisms for evading thermalisation (and similar information scrambling processes) in Chapter 4 and Chapter 5. Specifically, diagnosing thermality through level statistics has recently proven insufficient due to the discovery of "weak" violations of ETH via quantum many-body scarring [18], a phenomenon in which select initial states exhibit robust memory retention in an otherwise chaotic system. This will allow us to demonstrate an experimentally viable method for evading the loss of information in an interacting many-body system.

Chapter 3

Maximising thermalisation in a local quantum model of a black hole

3.1 Chapter introduction

In Chapter 2, we defined what it meant to be thermal in the setting of an isolated quantum system, and we introduced the SYK model as an example of a maximally thermalising model. Recently, the paradigmatic SYK model, whose holographic dual acts as a black hole, is found to saturate the bound on chaos and therefore maximally scramble information [51, 74–76]. This primes SYK to act as a perfect candidate for a quantum representation of a black hole.

This model, however, is related to a $(1+1)$D black hole only indirectly, through the $\mathrm{AdS}_{1+1}/\mathrm{CFT}_{0+1}$ correspondence [74]. Thus, it is useful to explore alternative models that may have a more direct connection to black holes. Here we study a recently introduced chiral spin-chain model [12,13]. The mean-field theory limit of this model describes Dirac fermions in a black hole background geometry, which is similar to the semiclassical limit of quantum gravity [99]. However, within the region of the chain representing the black hole's interior, the mean field theory description breaks down due to the dominance of strong correlations. One question that arises is if this strongly correlated region gives rise to optimal scrambling behaviour, as one would hope for a black hole model.

After introducing the background of the chiral spin model, we begin our work by demonstrating through new data that the model thermalises and also has maximal scrambling capacity. To probe the scrambling behaviour of the chiral spin-chain, we numerically investigate its Out-of-Time-Order correlators. OTOCs are a special class of

quantum correlation functions that determine the Lyapunov exponent, capable of diagnosing early-time chaotic behaviour [9, 69].

This naturally motivates the question if there is a use for this maximally-scrambling system, besides its conceptual connection to black holes. Remarkably, a use arises for this through quantum teleportation – a central concept of quantum information that highlights the stark contrast between classical and quantum physics [100–102]. In particular, many-body teleportation through the Hayden-Preskil protocol acts as a remarkable avenue wherein the chaotic nature of interacting quantum systems is utilised for greater success, making it amenable to realistic simulators of quantum systems [14, 103–107]. This protocol is an extension of the well-known single particle teleportation scheme. In this case, however, part of the wavefunction is now scrambled in order to increase the success fidelity of the protocol.

Our novel results arise from investigating the Hayden-Preskill protocol with the chiral-spin chain thereby utilising a maximally-thermalising system to perform a many-body quantum state teleportation. Using the chiral model, we demonstrate how the Hawking radiation and optimal scrambling behaviour can be used to model two of the physical process related to the black hole teleportation: the Page curve that gives the time after which the teleportation can take place to the butterfly velocity used to prepare information before optimal scrambling can take place. Our numerical simulations allow us to quantify the key timescales governing the teleportation process, including the Page time, radiation time, scrambling time, and butterfly velocity, showing their universal dependence on the chiral coupling strength. Comparing these timescales against other chaotic local models, demonstrates the supremacy of the chiral spin-chain as it successfully outperforms other systems which are commonly studied in the context of black hole quantum teleportation.

3.2 An optimally scrambling chiral model with effective black hole geometry

3.2.1 The chiral spin-chain model

The chiral spin-chain model, first introduced in Refs. [12, 13], is shown in Fig. 3.1. It describes an interacting chain of spin-1/2 particles with the Hamiltonian

$$H = \frac{1}{2}\sum_{i=1}^{N}\left[-u\left(S_i^x S_{i+1}^x + S_i^y S_{i+1}^y\right) + \frac{v}{2}\boldsymbol{S}_i \cdot \boldsymbol{S}_{i+1} \times \boldsymbol{S}_{i+2}\right], \tag{3.1}$$

where u and v are in general position dependent real numbers and $\boldsymbol{S}_i = (\sigma_i^x/2, \sigma_i^y/2, \sigma_i^z/2)$ where σ_i^α ($\alpha = x, y, z$) is the α-Pauli matrix of the ith spin. Notably, this is the XY model with an additional three-spin chirality term

$$\chi_i = \boldsymbol{S}_i \cdot \boldsymbol{S}_{i+1} \times \boldsymbol{S}_{i+2}, \tag{3.2}$$

that introduces interactions [12, 13, 108, 109]. The enumeration of the sites in the chiral interaction term causes the chirality to alternate along the chain, as shown in Fig. 3.1. Unless otherwise stated we adopt open boundary conditions.

As v is increased, the model undergoes a quantum phase transition from a gapless XY-phase to a gapless chirally-ordered phase, where the total chirality $\langle\chi\rangle = \sum_i \langle\chi_i\rangle$ acts as an order parameter. The critical point is located at $\frac{v}{2} \approx 1.12u$ [12, 13]. For $\frac{v}{2} \leq 1.12u$, the ground state is in a free XY phase with $\langle\chi\rangle = 0$. Using standard bosonisation techniques [110–112] we found that the interactions were irrelevant and the low energy physics is described by free fermions with renormalised Fermi velocities. On the other hand, for $\frac{v}{2} \geq 1.12u$ the chiral interaction dominates the XY term and the model transitions to a chiral phase with $\langle\chi\rangle \neq 0$. In this phase bosonisation is more complicated due to the system possessing two Fermi points. We find that in this phase, the model does not remain at the free fermion point, revealing the dominance of the interactions [13].

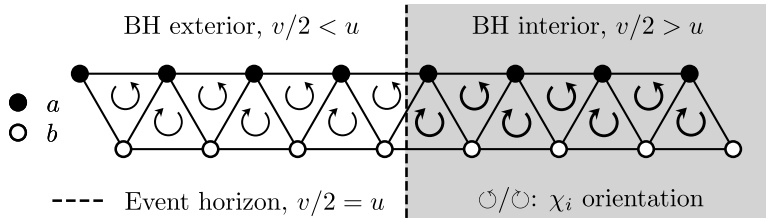

Figure 3.1: The chiral spin-chain (3.1) with position dependent chiral coupling v, while u is constant. Here, the chiral interaction, χ_i, acts on three successive spins and has alternating orientation. The fermionic sites a and b represent the unit cell of the mean field theory (MFT), where the spin of the Dirac field is encoded. The MFT gives the black hole (BH) geometry with v small on the left of the chain ($\frac{v}{2} < u$, outside BH) or large on the right ($\frac{v}{2} > u$, inside BH), with the horizon positioned at $\frac{v}{2} = u$ – for more details see Appendix A.1.

3.2.2 Black hole geometry

Intriguingly, the chiral model has a geometric interpretation in terms of black hole physics [12]. We first apply the Jordan-Wigner transformation that maps the spins into

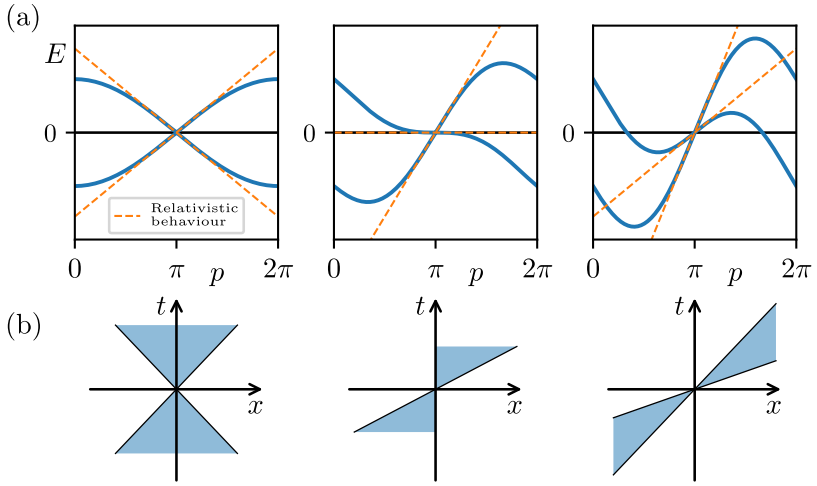

Figure 3.2: (a) The dispersion relation $E(p)$ obtained from the MFT description of homogeneous periodic chains. In the low energy limit it faithfully reproduces the behaviour of Dirac fermions in black hole geometry given by (3.4). (b) The lightcones, reciprocal to the dispersion relation that describe the effective metric (3.5) of the system for various values of v. From left to right, we take $v = 1$, $v = 2$ and $v = 10$ for the three panels respectively in btoh (a) and (b). $u = 1$ for all panels.

fermions. While the system is a 1D chain, one can equivalently view the system as a triangular ladder by sketching out the sites which exhibit XY and Chiral interactions. The system then has a unit cell of two fermion sites, a and b, sitting at opposite ranks of a triangular ladder, shown in Fig. 3.1 (see Appendix. A.1 for further information). By employing self-consistent mean field theory (MFT), one can map the interacting spin model to a model of free fermions on a lattice. In this limit the fermionic Hamiltonian becomes

$$H_{MFT} = \sum_{n=1}^{N} \left(u c_n^\dagger c_{n+1} + \frac{iv}{4} c_n^\dagger c_{n+2} + \text{h.c.} \right). \tag{3.3}$$

When $|v| \lesssim 2|u|$ the model is in a *non-chiral* phase with $\langle \sum_n \chi_n \rangle = 0$. The low-energy behaviour of the model is essentially equivalent to the XY model, since the interactions are irrelevant in a renormalisation group sense [12]. Therefore the non-interacting MFT accurately captures its physics. When $|v| > 2|u|$, the system undergoes a quantum phase transition to a *chiral* phase where $\langle \chi \rangle \neq 0$. In this coupling regime the MFT breaks down since the low-energy physics becomes strongly interacting, therefore the model must be described using the chiral spin-chain Hamiltonian (3.1) [13].

We can investigate the behaviour of the model by taking homogeneous coupling v and adopting periodic boundary conditions to extract the dispersion relation. This description faithfully captures the phase diagram of the model, albeit with critical point at

$\frac{v}{2} = u$. The dispersion relation of the model, shown in Fig. 3.2(a), at low energies, i.e., in the continuum limit, can be faithfully reproduced by the Dirac action on a fixed curved spacetime background

$$S_{\mathrm{MFT}} = \int \mathrm{d}^{1+1}x|e|\bar{\psi}(x)\left(ie_a{}^{\mu}\gamma^a\overleftrightarrow{\partial}_{\mu}\right)\psi(x), \tag{3.4}$$

where $a = 0, 1$ are local inertial frame indices, $\mu = t, x$ are coordinate indices; the spinor field is given in terms of the unit cell fermions as $\psi(x) = (a(x), b(x))^T/\sqrt{|e|}$ as shown in Fig. 3.1; $A\overleftrightarrow{\partial}_{\mu}B = \frac{1}{2}\left(A\partial_{\mu}B - (\partial_{\mu}A)B\right)$; $\gamma^a = (\sigma^z, -i\sigma^x)$; and $|e| = \det(e^a{}_{\mu})$. The zweibein $e_a{}^{\mu}$ are related to the spacetime metric by $g_{\mu\nu} = e^a{}_{\mu}e^b{}_{\nu}\eta_{ab}$, where $\eta_{ab} = \mathrm{diag}(1, -1)$ is the Minkowski metric and $g_{\mu\nu}$ is given by [12]

$$\mathrm{d}s^2 = \left(1 - \frac{v^2}{4u^2}\right)\mathrm{d}t^2 - \frac{4v}{u^2}\mathrm{d}t\mathrm{d}x - \frac{16}{u^2}\mathrm{d}x^2. \tag{3.5}$$

This is the Schwarzschild metric of a black hole expressed in Gullstrand-Painlevé coordinates [113–116] (see Appendix A.1 for more background details), which has also been observed in other synthetic black hole systems [117–120].

We now take the coupling v to be a function of position, $v(x)$, varying monotonically from small to large values. If it is slowly-varying compared to the lattice spacing, then the continuum description in terms of the Dirac equation remains valid. In this case the event horizon is located at $\frac{v}{2} = u$, where $\frac{v}{2} < u$ corresponds to the outside of the black hole and $\frac{v}{2} > u$ corresponds to the inside, as shown in Fig. 3.2(b). In Gullstrand-Painlevé coordinates the light cone tilts when approaching the black hole, having eventually both light directions pointing towards its centre inside the black hole, as shown in Fig. 3.2(b) (Right). We see that the event horizon aligns well with the boundary between the two phases of the spin-chain, where the chiral phase is inside the black hole and the XY phase outside. Using the mean field description it was shown in Ref. [12] that a free particle that passes through the phase boundary of our model emerges as a thermal radiation with the Hawking temperature, similar to other models [121–134]. We expect the thermalisation to Hawking temperature to be valid in the fully interacting model as the MFT is still valid around the horizon, only breaking down deep inside the black hole where the chiral interactions are dominant.

Apart from reproducing the semiclassical behaviour of a black hole, our model also exhibits a chaotic behaviour, as we shall see in the subsequent sections. This can be quantified by the Lyapunov exponent where for small v we obtain a Lyapunov exponent $\lambda \propto T^2$, as expected from perturbative interactions [135]. For large v, i.e. inside the black hole, the numerically obtained Lyapunov exponent exhibits linear behaviour $\lambda \propto$

T [11], with a slope which is in excellent agreement with the predicted optimal scrambling behaviour.

3.2.3 Quantum chaos inside the black hole

A natural question to ask is if this black hole geometric analogy of Eq. (3.1) extends to the thermalising dynamics expected at the interior of a black hole. In particular, we investigate whether the spin model is chaotic for $\frac{v}{2} > u$ (with homogeneous v along the chain) and, more importantly, whether it exhibits maximal information scrambling as expected of a black hole.

As we discussed in Section 2.1.2, one of the most effective methods for diagnosing the chaotic behaviour of a many-body quantum system is to study its energy level statistics, provided all relevant symmetries have been resolved. We consider the chain with periodic boundary conditions which has translational symmetry, U(1) symmetry and global spin flip symmetry $X = \prod_i \sigma_i^x$. We restrict to the symmetry sector with quantum numbers $k = 0, z = 0, x = +1$ of these symmetries, respectively, and determine the eigenvalues, $\{E_n\}$ of (3.1). We then take the set $\{s_n\}$, where $s_n = E_n - E_{n-1}$, and evaluate [64]

$$r_n = \frac{\min\{s_n, s_{n-1}\}}{\max\{s_n, s_{n-1}\}}. \tag{3.6}$$

The probability distribution over all r_n and average of this value, $\langle r \rangle$, are shown in Fig. 3.3. For $v \neq 0$, we find Wigner-Dyson statistics indicating that this model is chaotic, a characteristic that becomes more prominent with system size. Notably, we find $\langle r \rangle \approx 0.53$ [65], which corresponds to the GOE ensemble. This is perhaps unexpected since H possesses complex matrix elements. Despite this, the model retains time-reversal symmetry due to satisfying the relation $PH^TP = H$ where P is the parity operator, reminiscent of Ref. [136].

3.2.4 Extracting optimal scrambling via the Lyapunov exponent

The average level spacing $\langle r \rangle$ is a crude measure of the chaotic behaviour of a quantum system, in the thermodynamic limit we expect Wigner-Dyson statistics for all models except fine-tuned integrable systems. Therefore, we need a more precise measure of the chaotic behaviour of the system inside the black hole to determine whether the scrambling of quantum information is optimal, as it is the case for the SYK model [73].

As a diagnostic tool we will employ the Lyapunov exponent that we first introduced in Section 2.2.2, λ, that quantifies the rate of thermalisation of a chaotic system [137]. In the quantum mechanical framework, λ is calculated using the decay in out-of-time-order correlators (OTOCs) with respect to some local operator O_i on site i, as a function of

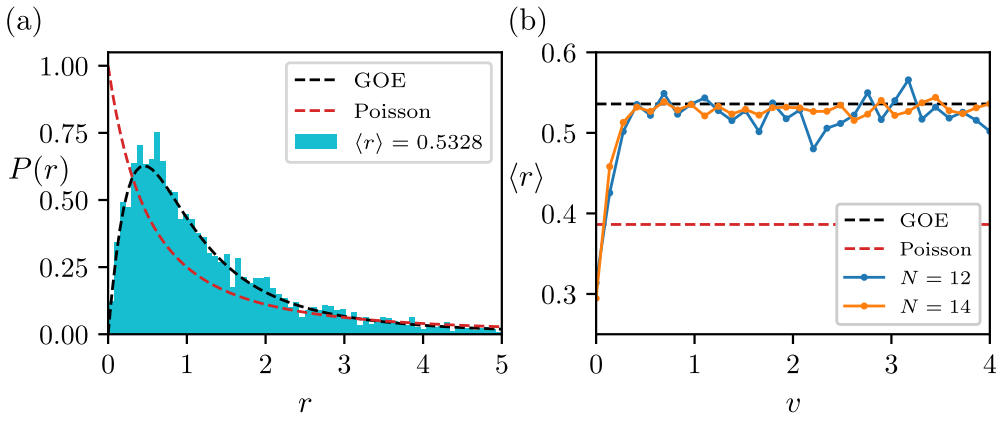

Figure 3.3: (a) The probability distribution of all r-values in the reduced symmetry sector at $N = 20, v = 4, u = 1$. In both cases we see the model matches the Gaussian orthogonal ensemble (GOE) indicating a non-integrable model [65]. (b) The average r-value (3.6) of the eigenspectrum of Hamiltonian (3.1) for different values of v and N ($u = 1$). Results were computed in the $k = 0, z = 0, x = +1$ symmetry sector.

time, t. We primarily focus on the regularised OTOC

$$C(t) = \langle O_i(t)\rho^{1/4}O_j(0)\rho^{1/4}O_i(t)\rho^{1/4}O_j(0)\rho^{1/4}\rangle, \tag{3.7}$$

where $\rho = \exp(-\beta H)/\mathcal{Z}$, with the partition function $\mathcal{Z} = \mathrm{Tr}\exp(-\beta H)$ and $\beta = 1/T$ is the inverse temperature. We also scale such that $C(0) = 1$.

The regularised version of OTOCs is suitable for investigating small temperature behaviours and exhibits fast convergence even for small system sizes [73]. This should be contrasted to the unregularised correlator which is subject to stronger finite-size corrections at low temperatures [138]. Using the regularised version, $C(t)$, we are restricted to exact diagonalisation techniques. Further restrictions are placed on system size $N \leq 13$ due to the need of time evolution. Fortunately, due to the fast convergence of our model with system size, we find this to be sufficient for our study. Unless otherwise stated, we take $O_i = S^x_{N/2}$ and $O_j = S^x_{N/2-2}$ for N even and $O_i = S^x_{(N+1)/2}$, $O_j = S^x_{(N-3)/2}$, for N odd. While the choice of $O = S^x$ restricts the use of system's symmetries, it is reminiscent of the Majorana fermionic operators in the SYK model and successfully unearths the desired optimality behaviour. We show below that the regularised correlators we choose, allow us to faithfully extract the chaotic behaviour of the model even with moderate system sizes.

With maximally quantum information scrambling models, one expects an exponential decay in the OTOCs defined in Eq. (3.7) with an associated Lyapunov exponent, λ, indicating the rate of decay. The numerical recipe we employ here is identical to that

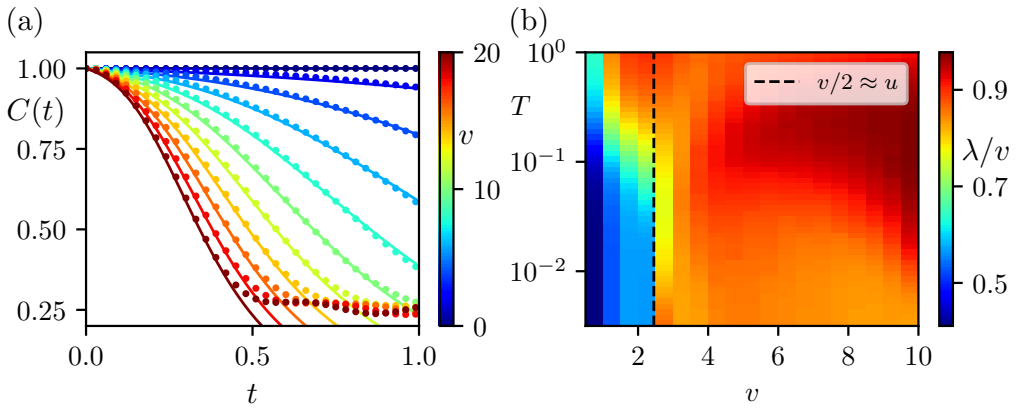

Figure 3.4: Out-of-time-ordered correlators, $C(t)$, and Lyapunov exponent, λ, of the chiral spin-chain for various coupling regimes. (a) Coloured dots show the numerically evaluated $C(t)$ given in Eq. (3.7) for various values of v (shown in the colour bar), and $T = \infty$. Lines show the fit of Eq. (3.8) with $\lambda = 0.78v$, which improves for v deep in the chiral phase. (b) Using the same process and parameters as in (a), we compute the OTOCs, while varying both T and v and extract λ via fitting (3.8). Large values of λ are observed for large v (chiral regime) and large temperatures T that probe the full spectrum of the Hamiltonian. Black dashed line indicates the phase transition at $v/2 \approx u$, where a clear change in behaviour at low temperatures is witnessed. Both plots are computed with $N = 10$, $u = 1$.

presented in Ref. [73] in the context of SYK. We find that the same method is effective at identifying the scrambling behaviour of our model. Mirroring this study of the SYK model, we fit the numerical data of Eq. (3.7) to the semiclassical function of the OTOC at low temperatures

$$C(t) = U\left(\frac{1}{2}, 1, Ne^{-\lambda t}\right)\sqrt{N}e^{-\lambda t/2}, \tag{3.8}$$

where U is the Kummer's confluent hypergeometric function and λ is the fitted Lyapunov exponent. This function is justified at low temperatures and provides a phenomenological model for capturing the higher-order effects that occur after the initial period of exponential growth and is demonstrated in [76]. In general, we expect λ to depend on the coupling v and the temperature T of the model, while we keep $u = 1$. Fig. 3.4 (a) shows the behaviour of OTOCs for various values of coupling v when $u = 1$ and the system size is $N = 10$. We verify that the OTOCs exponentially decrease in time as seen by the fit (solid lines) in Fig. 3.4 (a) with $\lambda = 0.78v$. This exponential scrambling behaviour is present for large v, that take the spin-chain in the chiral regime, i.e. inside the black hole. These results remain largely unchanged as we vary the system size demonstrating the fast convergence in the properties of the chiral spin-chain.

With the confirmed presence of exponential decrease in the OTOCs with time, we

have already substantiated the argument for the presence of exponential scrambling characterised by the Lyapunov exponent. We now investigate the change in the Lyapunov exponent with temperature where temperature defines the average energy of the density matrix. Zero temperature corresponds to the ground state while infinite temperature corresponds to a uniform superposition of all eigenstates. Due to expected thermal behaviour of mid spectrum eigenstates in chaotic models, one expects the Lyapunov exponent, λ, to increase with T to some maximal bound. The behaviour of λ as a function of the coupling v and the temperature T is given in Fig. 3.4 (b), where the increase in λ is observed with v and T, as expected. We also note a sudden change in the behaviour of λ/v as v crosses the phase transition point $\frac{v}{2} \approx u$ at small temperatures, revealing the corresponding dramatic change in the scrambling behaviour of the model.

It is predicted that the Lyapunov exponent, describing the scrambling behaviour in quantum systems, satisfies the universal bound $\lambda/J \leq 2\pi T$, where J is a characteristic coupling of the system [11]. The quantum gravity description of black holes and their holographic duals, such as the SYK model, are known to saturate this bound [68], when λ is normalised by appropriately chosen coupling J. This optimal scrambling behaviour is analytically and numerically identified in the SYK model for low temperatures [11], and has been investigated in an experimentally realisable context [139]. We will now investigate whether the chiral spin-chain is optimally scrambling or not. To achieve that we will quantitatively determine the functional dependence of the Lyapunov exponent on temperature, T, for various regimes of v that correspond to the inside and outside of the black hole. Again, we employ the same method seen in [73] when fitting with Eq. (3.8).

In the low temperature limit we expect that in the weakly-interacting regime, described by $\frac{v}{2} < u$, the Lyapunov exponent will grow quadratically with temperature. This is due to the T^2 dependence on the resistivity typically expected in Fermi liquids in the absence of interactions [135, 140, 141]. In Fig. 3.5(a) we observe that the Lyapunov exponent obtains the quadratic behaviours as T goes to zero, when v is small, i.e. outside the black hole. Note that odd system sizes have a zero offset, i.e. $\lambda \to 0$ as $T \to 0$, while for even N there is a non-zero offset. This offset is a finite system size effect that tends to zero as N increases.

If the strongly interacting regime, $\frac{v}{2} > u$, exhibits black hole phenomena, then optimal scrambling is expected, witnessed by a linear growth of the Lyapunov exponent, $\lambda/J = 2\pi T$. In Fig. 3.5(b) we observe that, similar to the SYK model [73], the numerically obtained Lyapunov exponent has a liner dependence on temperature. Hence, we anticipate that the chiral spin-chain exhibits optimal scrambling at the coupling regime that describes the inside of a black hole. To quantify how accurately the quadratic and linear behaviours are manifested in our system we module a fit in the data of the form

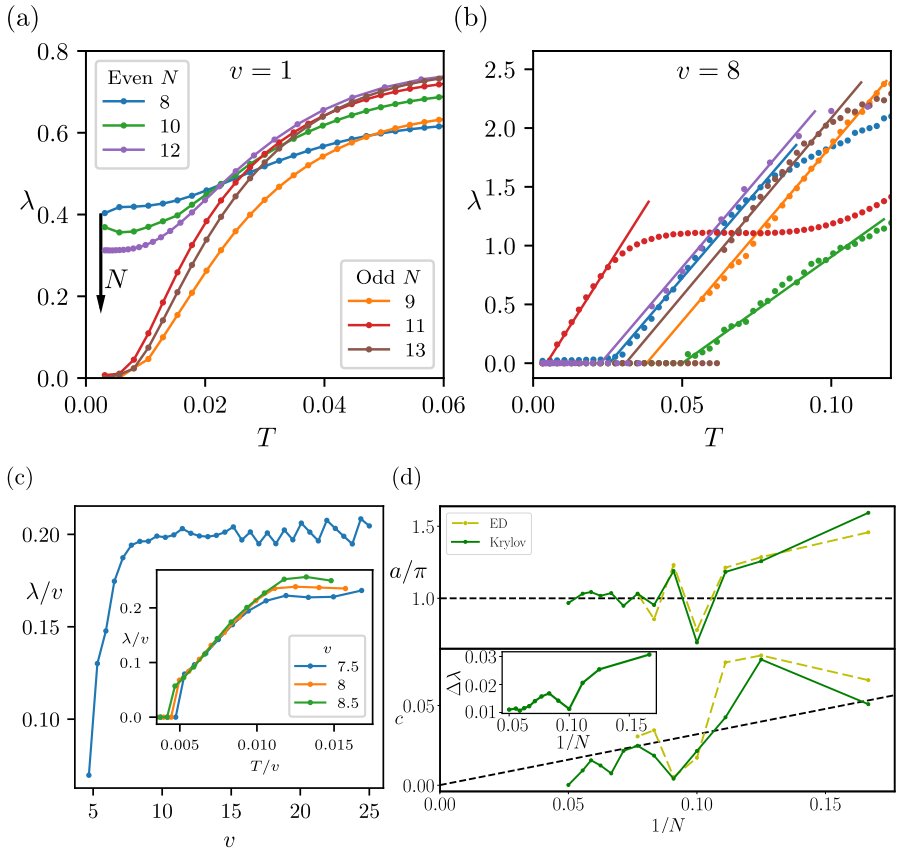

Figure 3.5: The Lyapunov exponent of the chiral spin-chain simulating the black hole. (a) Outside the black hole ($v = 1$ and $u = 1$) the Lyapunov exponent exhibits at low temperatures a quadratic behaviour. The observed even/odd system size dependence is decreased when N increases. (b) Inside the black hole ($v = 8$ and $u = 1$) a linear behaviour in the Lyapunov exponent is observed, indicating optimal scrambling. (c) The functional dependence of the linear regime of λ on the coupling v. When scaling both λ and T by v we find that with increasing v, the scaled Lyapunov exponent eventually flattens out ($N = 8$). (Inset) Upon scaling both λ and T axis by v, the linear plots collapse on top of each other ($N = 12$). (d) In the linear regime we fit $\lambda = a(T - c)$ as shown in (b) and extract the slope a (top) and the offset c (bottom). We plot a scaled by $v/2$ and by 2π against $1/N$. As N increases the fitting parameters approach $a \to 2\pi\frac{v}{2}$ and $c \to 0$, thus recovering the optimal scrambling behaviour in the thermodynamic limit. Black dashed lines are for guiding the eye. Results are computed using exact diagonalisation (ED) for smaller system sizes, and a Krylov subspace method (see Appendix B.2 for details) to reach larger system sizes. We see excellent agreement for the two when ED is possible. ED results are from $N = 6$ to $N = 13$, while Krylov results are up to $N = 20$. Inset shows the average standard error in λ from the Krylov subspace method vs N which is larger for smaller system sizes. These results are for $v = 8.0$. $v = 7.5$ and $v = 8.5$ show similar behaviour.

$\lambda = a(T^b - c)$ and study b with system size. We find that b takes values 1 and 2 in the corresponding regimes to a very good accuracy (see Appendix A.2 for more details). Furthermore, Fig. 3.5(c) shows that for large enough v, the Lyapunov exponent remains more or less constant taking the value $\lambda/v \approx 0.20$. This should be contrasted to other sub-optimal models with a rate of chaos that is parametrically slower than the SYK model [142, 143].

We next investigate the slope of the linear behaviour exhibited by the Lyapunov exponent when v is large. In Fig. 3.5(b) we identify the linear behaviour $\lambda = a(T - c)$ for a range of temperatures between $T_{\min}$ and $T_{\max}$. Here, $T_{\min}$ depends on the discreteness of the finite system and tends to zero as N increases, while $T_{\max}$ depends on the rest of the dynamics of the chiral model. The saturation of the scrambling bound is achieved for a linear gradient 2π normalised by the coupling of interactions, given in Hamiltonian (3.1) by $v/2$. In Fig. 3.5(d) (Top) we see that the slope of $\lambda/(v/2)$ as a function of temperature, $2a/v$, tends to 2π with increasing system size as expected from the optimal scrambling behaviour. Moreover, we observe that the constant offset, c, tends to zero with increasing system size, N, where the dashed line in Fig. 3.5(d) (Bottom) is a linear fit to the data. Note that both a and c show a strong oscillatory behaviour as a function of N, indicating the significance of the boundary effects.

To address this, we use both ED and a Krylov subspace method (see Appendix B.2). We find the two methods agree in the system sizes available through ED, therefore verifying the integrity of the Krylov algorithms results. The Krylov subspace method then allows us to reach much larger system sizes than ED, where we see a rapid trend to the expected values with oscillations decreasing with system size. Hence, in the strong chiral regime of our simulator, i.e. inside the black hole, we expect to have $\frac{\lambda}{v/2} = 2\pi T$ in the thermodynamic limit. Although, resolving the ambiguity associated with choosing the appropriate energy scale of the model, $J = v/2$, needs a theoretical investigation that goes beyond the scope of this work, we postulate that this expression corresponds to optimal scrambling.

Our numerical investigation shows that as the coupling v varies from small to large values the spin-chain (3.1) undergoes a quantum phase transition. This transition does not only changes its ground state properties from non-chiral to chiral [12, 13], but its thermalisation properties change from weakly scrambling to optimal scrambling at $\frac{v}{2} \approx u$, much in the same way as in [144]. Notably, our system does not have random all-to-all interactions as it is the case for the SYK model [73]. This locality and uniformity facilitates the fast convergence of our numerical simulations with system size to the expected behaviour. This is manifestly seen in Fig. 3.5, where system size effects become less pronounced with increasing N.

3.3 Exploiting maximal scrambling through quantum teleportation

Having established the existence of an maximally thermalising local model through the chiral spin-chain, we next present an application. Being local, the chiral model is naturally primed towards experimental feasibility in both cold atom systems and quantum circuits compared to the SYK model. One may reasonably believe however that thermalisation in a quantum system may serve as a detriment on quantum hardware due to the desire to retain information. This turns out to not always be the case. The Hayden-Preskill protocol is a teleportation scheme which counter-intuitively makes use of quantum thermalisation in order to maximise the success of state transfer.

Quantum teleportation is a fundamental protocol in quantum information theory, enabling the transfer of an unknown qubit state $|\psi\rangle$ from Alice to Bob, provided they share a maximally entangled Bell pair state, $|epr\rangle$. In the standard protocol, Alice performs a joint measurement on $|\psi\rangle$ and her share of $|epr\rangle$, then transmits the measurement outcome to Bob via a classical communication channel. Upon receiving this information, Bob applies a corrective unitary to recover $|\psi\rangle$ with unit fidelity and probability, with fidelity being defined as

$$\mathcal{F}(t) = |\langle\psi(0)|\psi(t)\rangle|^2. \tag{3.9}$$

Despite its simplicity, quantum teleportation has become a cornerstone of modern quantum communication, with experimental demonstrations extending up to 1400 km [145–149].

Hayden and Preskill presented a black hole adaptation of teleportation, where Alice's quantum state is thrown into a black hole, and Bob attempts to recover it from outgoing Hawking radiation [14, 103–107]. Unlike standard teleportation, this process bypasses classical communication, instead relying on two key quantum phenomena: Hawking radiation, which establishes entanglement between the black hole and its exterior, and optimal scrambling, which rapidly disperses quantum information within the black hole interior [70]. When the black hole has passed the Page time—the moment when its interior and exterior are maximally entangled—Hawking radiation can be distilled to reconstruct entangled pairs, allowing Bob to probabilistically recover Alice's state.

The Hayden-Preskill teleportation protocol is one of the most striking predictions of quantum black hole physics, demonstrating that black holes can act as near-instantaneous mirrors of quantum information. This challenges the classical notion that information falling into a black hole is lost, reinforcing the idea that black holes may function as highly efficient quantum processors. While this phenomenon depends upon the rapid scrambling expected in quantum gravity, a complete theoretical description remains elusive. The Hayden-Preskill protocol is also a fundamentally many-body extension of the traditional

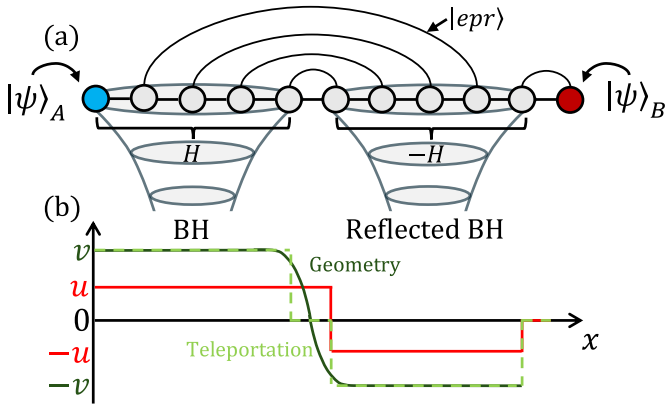

Figure 3.6: (a) Schematic of the chiral spin-chain with the encoded state $|\psi\rangle_A$ and the initially prepared EPR states, $|epr\rangle$. The scrambling inside the black hole is caused by Hamiltonian H, while bipartite Hamiltonian $H \oplus (-H)$ with left and right halves corresponding geometrically to mirrored black holes. (b) The coupling profile for u and v along the spin-chain for the Hamiltonian in Eq. (3.1). We highlight the difference in the v coupling between the (smooth) geometric interpretation where a large free system can be numerically considered and the teleportation protocol fit in a small strongly interacting system. The two-site u term flips after the site $(N-1)/2$, while the 3-site v term is 0 on site $(N-1)/2$ but becomes $\pm v$ on either side.

few-qubit quantum teleportation. Consequently, various quantum information models and condensed matter analogues have been developed to explore its dynamics [9, 150]. In what follows, we will implement the Hayden-Preskill protocol using the established optimally scrambling chiral spin-chain simulator, and demonstrate the power of quantum thermalisation in efficiently teleporting qubits with high-fidelity success rates.

3.4 Encoding a teleportation protocol with the chiral spin-chain

3.4.1 Black hole teleportation

Hayden and Preskill proposed a scheme for teleporting the quantum information stored in a black hole. Alice, who resides inside the black hole, seeks to teleport the quantum state $|\psi\rangle_A = \alpha|0\rangle + \beta|1\rangle$ to Bob who is positioned outside the black hole. As classical communication is forbidden due to the event horizon, the teleportation protocol instead relies on quantum correlations established through $L = (N-3)/2$ EPR pairs $|EPR\rangle = |epr\rangle^{\otimes L}$, where $|epr\rangle = \frac{1}{\sqrt{2}}(|01\rangle_{AB} - |10\rangle_{AB})$, arranged in a nested fashion, as shown in Fig. 3.6, and an optimally scrambling evolution U within the black hole [11, 50, 70]. Alice's system A now consists of a state $|\psi\rangle_A$ on site $n = 1$ and one qubit from each of

the L Bell pairs on sites $n = 2$ to $n = (N-1)/2$. Bob's system is the remaining qubits from the L Bell pairs on sites $n = (N+1)/2$ to $n = N-2$, and a final $|epr\rangle$ between sites $n = N-1$ and N. This state can be rewritten as

$$|\psi\rangle_A \otimes |EPR\rangle \otimes |epr\rangle_{N-1,N} = \frac{1}{2} |epr\rangle_{A,N-1} \otimes |EPR\rangle \otimes |\psi\rangle_B + \frac{1}{2} \sum_{a=x,y,z} \sigma_A^a |epr\rangle_{A,N-1} \otimes |EPR\rangle \otimes \sigma_B^a |\psi\rangle_B . \tag{3.10}$$

Crucially, the first part of Eq. (3.10) is left invariant by Alice applying U on sites $n = 1$ to $n = (N-1)/2$ provided Bob applies a corresponding unitary U^* (the complex conjugate of U) to sites $n = (N+1)/2$ to $N-1$ at their end. Despite this, such a unitary will in general scramble the remaining part of the state, including the central L EPR pairs. Therefore, if Bob performs E many EPR measurement and post-selects the outcomes to be $|epr\rangle$, with high probability the state will originates from the first part of (3.10), and Bob will have successfully teleported the state. Rapid scrambling of the state is vital to achieve this result, so that the EPR measurements have a low probability of reproducing $|epr\rangle$ for the second part of the state. Assuming full thermalisation of the state the probability $P_E = \frac{1}{4} + \frac{3}{4^{E+1}}$ and fidelity $F_E = 1 - \frac{2}{(4^E+3)}$ tend to $\frac{1}{4}$ and 1, respectively, exponentially fast as E increases [150]. The faster the system thermalises, the faster this result is obtained.

3.4.2 Chiral spin-chain encoding

To employ the chiral spin-chain simulator, Alice introduces her state $|\psi\rangle$ inside the black hole, where it evolves under the Hamiltonian H given in (3.1) for time t, producing the scrambling unitary $U = e^{-iHt}$. The nested structure of the $|epr\rangle$ states allows Bob to apply the counter evolution $MU^*M = e^{iHt}$ outside the black hole. M is a unitary operator which spatially inverts the order of the spins, leaving the $|EPR\rangle$ state invariant, as well as the Hamiltonian since $MH^*M = H$. As a result, the total evolution for the system is given by $e^{-iHt} \otimes e^{iHt} \otimes I_N$, where I_N is the identify acting on the Nth spin.

In the chiral model, this evolution is realised by introducing a coupling configuration $H \oplus (-H)$ that corresponds to a binary black hole system. We emphasise that neither H acts upon the final spin of the chain, as shown in Fig. 3.6. A step function profile for $u(x)$, where u changes sign at the centre of the chain, and a tanh profile for $v(x)$, as previously studied in Ref. [12], are given by

$$u(x) = -\mathrm{sgn}(x - x_0), \;\; v(x) = \alpha \tanh[\beta(x - x_0)] + 1, \tag{3.11}$$

where $x_0 = aN/2$ is the central site of the spin chain and a is the lattice spacing. The

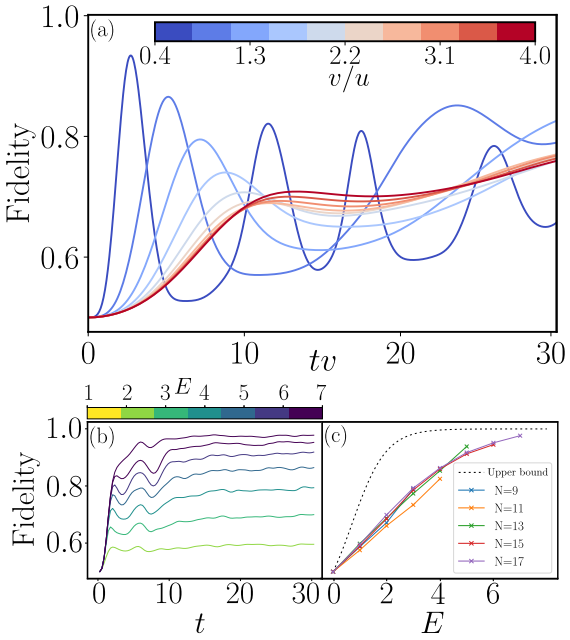

Figure 3.7: (a) Fidelity of teleportation over time, t, scaled by v after quenching the initial state, $|\psi\rangle_A \otimes |EPR\rangle$, with Hamiltonian (3.1). Success is determined by the overlap between the final state $|\psi\rangle_B$ of the last site with the initially prepared state $|\psi\rangle_A$. Colour indicates the value of v during the quench where we see a notable change in teleportation success across the phase transition at $v/u \approx 2$. Four EPR pairs, $|epr\rangle$, are measured in this case. As we enter the maximally scrambling regime, we find the teleportation scheme is executed more quickly. (b) Similarly but unscaled in time and at a fixed $v = 8$. Colour corresponds to a different number of EPR pairs measured, E, where we see teleportation success increases with E as expected. Here we take $N = 17$ and $u = 1$ using ED. (c) Taking a slice at $t = 30$ in (b) for different system sizes, we see how the scaling of fidelity with E changes for system size N when compared to the theoretical upper bound of F_E. We see with increasing system size our results tend towards the optimal theoretical prediction.

gradient of $v(x)$, and hence the Hawking temperature, is controlled by tuning α and β. This configuration creates Hamiltonian H in one half of the system and $-H$ in the other. From the metric in (3.5) we see that the black hole horizons appear at $|v|/2 = |u|$, while the interiors reside at the chain's edges, with a small shared exterior region at the centre. An additional XY-Hamiltonian at the exterior of the black holes leaves the total $|EPR\rangle$ state unchanged. Throughout this work we couple the two chains with a $u(N/2) = +1$ allowing non-trivial hopping between the two halves of the system, as shown in Fig. 3.6 although the results are not sensitive to this choice. Information is first encoded in the left black hole by Alice. Then, the system is evolved for time t before E many EPR measurements are applied and the fidelity of the teleportation, F, is monitored.

The time evolution of the fidelity is shown in Fig. 3.7(a). We observe that for small chiral couplings, $v/2 < u$, the fidelity oscillates without the ability to produce successful teleportation for a sustained period of time. On the other hand, when $v/2 > u$ the fidelity increases and remains high and stable. This stability is seen to increase with system size. Further results discussing the relevance of system size and number of measurements for the teleportation protocol can be found in Appendix B.1.1. The contrast between oscillatory and constant behaviour is due to the absence or presence of interactions that cause scrambling in the initial $\sigma^a |EPR\rangle$ state. For example, for the non-interacting mean field theory defined in Eq. (3.3), oscillatory behaviour is observed for all values of v. When the system is in the strong chiral phase, we observe an increase in the fidelity when the number of measurements is increased. This is shown in Fig. 3.7(b) where the fidelity is plotted against time. In fact, the increase of the teleportation fidelity is exponential with the number E of EPR measurements, as shown in Fig. 3.7(c), guaranteeing a fast convergence to unit fidelity. As a result, the chiral spin-chain can successfully reproduce the Hayden-Preskill teleportation protocol.

3.5 Physical processes in black hole teleportation

We now discuss the different physical effects that are involved in the black hole teleportation process. The aim is to determine the overall duration our quantum simulator takes to perform the Hayden-Preskill protocol. This includes utilising key features such as the geometry encoding and optimal scrambling behaviour which allows us to identify the relevant timescales.

3.5.1 Hawking radiation and Page time

An essential mechanism in black hole teleportation is Hawking radiation that builds quantum correlations between the inside and the outside of the black hole. This effect can be analysed with the semiclassical limit of the black hole, which corresponds to the mean field theory of the chiral spin-chain model. We demonstrate that Hawking radiation can generate the quantum correlations necessary for teleportation within a binary black hole system. Furthermore, we show that the coupling configuration (3.11), adopted for black hole teleportation, preserves the geometric properties of the metric (3.5) at the horizon, as encoded in the temperature of the Hawking radiation.

Here, we utilise the mean-field theory (MFT) description of the chiral spin chain given in (3.3). We begin by determining the Page curve, which tracks the entanglement entropy of the black hole across the horizon during Hawking radiation, considering a single-particle population inside the black hole, with the exterior initially empty. We

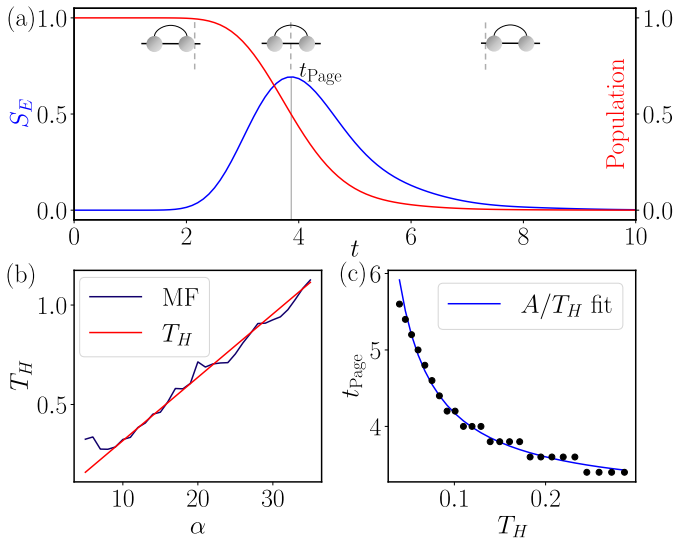

Figure 3.8: Page curve, Page time, and Hawking temperature of the mean-field (MF) chiral Hamiltonian (3.3). (a) The entanglement entropy, S_E (blue line), of the black hole across the horizon as a function of time, t, during the Hawking radiation of a single particle. This curve, known as the Page curve, reaches its maximum at the Page time, t_{Page}, when the population inside the horizon (red line) is halved. To accelerate black hole evaporation, we consider a single-particle population inside the black hole and place the horizon at $n_h = 2$, while the entropy is evaluated for a bipartition at $n = 22$ to account for the entropy of particles that are completely free from the black hole attraction. The inset sketches illustrate the evolution of an EPR pair as it crosses the event horizon (dashed line): at early times, the EPR pair is entirely inside the black hole ($S_E = 0$); at t_{Page}, half of the pair escapes, yielding maximal entanglement ($S = \ln 2$); at late times, the second half is also emitted, leading to $S \to 0$. (b) The Hawking temperature T_H as a function of α in the MF model (blue line) compared to its analytical value $T_H = \alpha\beta/2\pi$ (red line). Here, $N = 500$ and the horizon is at $n_h = 250$. (c) Page time t_{Page} as a function of T_H in the MF model (black dots), alongside the fitted curve A/T_H (blue line) with $A = 0.278$, obtained numerically by varying α and β.

also assume a small horizon radius, $n_h = 2$ where n_h is the site where the coupling profile changes sign, ensuring that complete tunnelling of the particle across the horizon occurs within a reasonable timescale. Initially, the system is in a tensor product state across the horizon, corresponding to an entanglement entropy of $S_E = 0$. As the particle tunnels outward, the fermionic mode inside the black hole becomes entangled with modes outside, leading to an increase in entanglement. When the population inside the black hole is halved, the entropy reaches its maximum, $S_E = \ln 2$. Subsequently, as the black hole population asymptotically approaches zero, the entanglement entropy decays to $S_E \to 0$. This simple model reproduces the Page curve shown in Fig. 3.8(a), with the time at which entropy is maximised defining the Page time, t_{Page}. A more precise

simulation of black hole evaporation would require more particles inside the black hole and a simultaneous reduction in the horizon radius reflecting the loss of mass due to Hawking radiation [6, 151–159]. Nevertheless, our process convincingly demonstrates how the simulated black hole becomes entangled with its exterior, a key requirement for executing the Hayden-Preskill protocol. Full details of this calculation can be found in Ref [160].

Next, we examine the Hawking radiation temperature, T_H, using the same configuration. In particularly, a single particle is placed inside the black hole and the coupling pattern given in (3.11) is chosen, defining a binary black hole system. To accurately reproduce the Hawking temperature, we use a large system, $N = 500$, with the horizon positioned in the middle, $n_h = N/2$. The particle inside the black hole is initialised at $n = 230$ and evolves under the MFT Hamiltonian (3.3). By varying the curvature at the horizon, e.g., by tuning α, the temperature of the outgoing radiation follows the theoretical prediction

$$T_H = \frac{1}{2\pi}\left|\frac{dv(v_h)}{dx}\right| = \frac{\alpha\beta}{2\pi}. \tag{3.12}$$

Previously, it was demonstrated that an analogous system with uniform $u(x)$ yields a consistent T_H across a range of temperatures and initial states [12]. Although the sign change in u, introduced in (3.11) for the implementation of the teleportation protocol, leaves the metric (3.5) unaffected, the derivation of this metric assumes uniform couplings. This raises the question of whether the dynamical properties of the chain, such as Hawking radiation, remain unchanged. To verify this numerically, we extract the Hawking temperature from radiation emitted through the horizon after a dynamical quench inside the black hole following the same method as in [12]. Fig. 3.8(b) shows the Hawking temperature as a function of α, demonstrating excellent agreement with theoretical predictions across a wide range of couplings. This confirms that the coupling configuration (3.11) accurately reproduces the black hole geometry, yielding Hawking radiation with temperature $T_H = \frac{\alpha\beta}{2\pi}$.

Modelling the black hole with a chiral spin chain allows us to identify the characteristic timescales governing the Hayden-Preskill teleportation protocol. The teleportation process can only proceed after the Page time, since this ensures that quantum matter inside the black hole is maximally entangled with the exterior. Only beyond this point can Hawking radiation reliably transmit EPR pairs across the horizon, facilitating the Hayden-Preskill protocol. The Page time, t_{Page}, marks the moment when the entanglement entropy of the emitted Hawking radiation reaches its peak, given by $t_{\text{Page}} = \frac{S_E}{2\pi T_H}$, where S is the black hole entropy [161, 162]. Subsequent Hawking radiation, which

provides additional EPR pairs to Bob, follows the emission timescale

$$t_{\text{rad}} = \frac{\Delta S_E}{2\pi T_H}, \tag{3.13}$$

where ΔS_E represents the corresponding entropy change. Fig. 3.8(c) confirms that the Page time, obtained by varying α and β, is inversely proportional to T_H. Since $T_H \propto \alpha \propto v$, the radiation emission time t_{rad} scales inversely with the chiral coupling v.

3.5.2 Optimal scrambling

One of the most important characteristics of black holes in a quantum context is that they are optimal scramblers [70]. Moreover, this property is vital to the success of the Hayden-Preskill protocol [103].

In principle, almost every many-body quantum Hamiltonian H is chaotic, and should therefore scramble the system. In this sense almost every Hamiltonian is an equally valid choice to realise the Hayden-Preskill teleportation protocol [163]. Nevertheless, the chiral spin-chain model is a uniquely appropriate for two reasons. Firstly, the MFT description discussed above means the results can be understood in the large system limit as describing Dirac fermions in a curved spacetime. Secondly, the behaviour of OTOCs for the interacting system demonstrates that the system is optimally scrambling, as we previously demonstrated before. We now demonstrate the advantageous nature of the optimal scrambling found in the chiral-spin model for the teleportation procedure. In practicality, one would ideally complete the teleportation between Alice and Bob in the quickest time possible to minimise both experimental error, and to easily repeat the procedure. The shortest time possible comes from the time taken to maximally scramble the second term in Eq. (3.10), which is determined by the scrambling time of the system. As the chiral spin-chain saturates the optimal bound for scrambling, demonstrated by the behaviour of the Lyapunov exponent shown in Fig. 3.5, the teleportation protocol will become maximally efficient.

We compared the teleportation protocol of the chiral-spin model to two other chaotic models, demonstrating that the chiral model exhibits more rapid teleportation. These models are the mixed-field Ising model [164–166], a commonly studied chaotic model, and the 2D ladder XY model where the same teleportation protocol was studied in Ref. [150]. For the former, we use the model parameters identified in Ref. [164] where these were found to correspond to a maximum entanglement distribution, corresponding to its maximally chaotic point. We scale the chiral model parameters such that the energy scales of the three models are comparable and compare for different values of v/u. We see in Fig. 3.9 that the chiral model outperforms both models for v larger than the

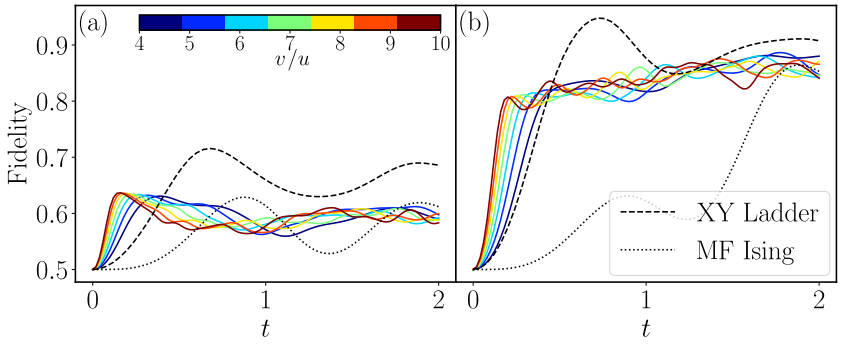

Figure 3.9: Comparison of teleportation fidelity over time after quenching the initial state with the chiral-spin model (solid lines), the XY ladder (dashed line), and the mixed field (MF) Ising model (solid dotted line). In the case of the mixed field Ising, the optimal ratio of values for chaos is used, as suggested in Ref. [164].(a) shows $E = 1$, while (b) shows $E = 4$ EPR measurements. Colour indicates the value of v during the quench in the chiral-spin chain. Using comparable Hamiltonian parameters between the three models, we find the chiral-spin chain outperforms both the XY and mixed field Ising model, as evidenced by an earlier saturation in the teleportation success. The results are for $N = 13$ using ED for all systems. For couplings, in the chiral model we take $u = -8$ such that the XY term has overall prefactor 1. For the XY ladder, we take the Hamiltonian from Ref. [150] with couplings J_x=0.91, $J_y = 1$ while for MF Ising, we take the Hamiltonian from [164] with $J = 1$, $h_x = 1.1$ and h_z=0.3.

phase transition, demonstrating the optimal scrambling in effect and the advantage of this model.

Finally, we estimate the scrambling time t_{scr}, which quantifies how quickly the black hole interior thoroughly mixes quantum information. It is believed t_{scr} to be inversely proportional to the Lyapunov exponent λ as $t_{\text{scr}} \propto \frac{1}{\lambda}$. While for small temperatures, the chiral spin-chain model saturates the bound on chaos $\lambda/(v/2) = 2\pi T$, during the teleportation protocol the system is effectively infinite temperature due to its maximal entanglement with the outside. These numerical results (see Appendix B.1.2) indicate that at that regime the Lyapunov exponent is approximately $\lambda \approx 0.78v$. Thus, the scrambling time follows $t_{\text{scr}} \propto 1/v$, which is consistent with the teleportation results in Fig. 3.7.

3.5.3 Butterfly Velocity and the propagation of information

The speed of the teleportation protocol also depends upon the order the EPR measurements are performed. This arises from the finite time necessary for information to propagate along the chain between the initial teleportation qubit and the position of the first EPR measurement. The black hole Hamiltonian, H, will immediately begin

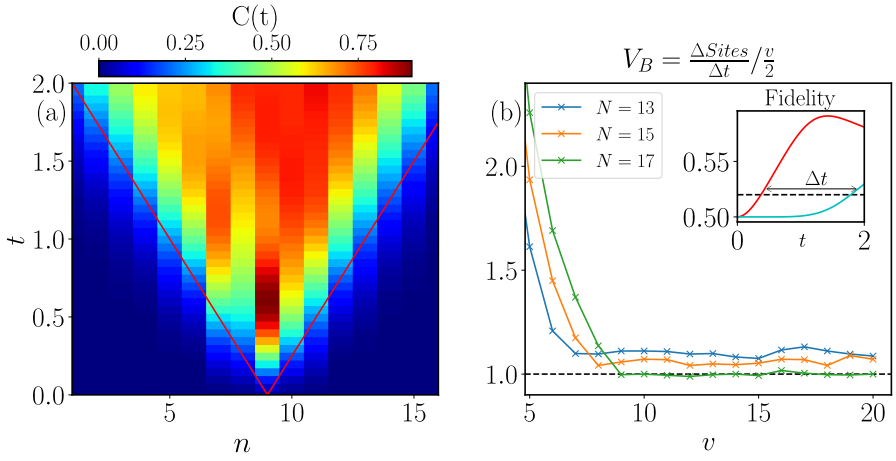

Figure 3.10: Butterfly velocity and black hole teleportation time. (a) is the regularised Out-of-time order correlators (colour scale) over time measured on site i. A linear fit is then applied to estimate the butterfly velocity which is found to be $V_B \approx v/2$. Results are computed using a Krylov algorithm for $N = 17$, $v = 8$, $O_n = \sigma_n^Z$ at infinite temperature in Eq. (3.7). (b) We estimate the speed of propagation of quantum information by comparing the fidelity when measuring the outer EPR pair first versus the inner EPR pair first during the projection in the teleportation protocol shown in Fig. 3.6. We find the time difference, Δt, for when these two fidelities match (see Inset), indicating the time spent for information to propagate between these two EPR pairs positioned at distance Δl. We use this to estimate the butterfly velocity, $V_B = \Delta l/\Delta t$, which remarkably saturates to $V_B = v/2$ with increasing system size.

scrambling the EPR state on the site where the σ_A^a rotation is acting (cf. Eq. (3.10)). This is the only site where the state is different from the $|EPR\rangle$ state, which is an eigenstate of the full scrambling Hamiltonian H. Therefore, for EPR pairs far from this state to become scrambled, the effect needs to propagate there with speed set by the butterfly velocity, V_B. For example, measuring the inner EPR pair in contrast to the outer (see Fig. 3.10(a)), will cause a delay in the teleportation success due to the need for information to first propagate across their respective locations before scrambling can take place [167].

We calculated the delay created due to the measurement order in the following manner. Firstly, we measured the gradient of the regularised OTOCs, as in Eq. (3.7), along the chain - a typical method used to estimate the butterfly velocity. The results are shown in Fig. 3.10(a) where the gradient of the red line is found to be $V_B \approx v/2$. We note the difference in the left and right propagation due to the chirality of the model breaking inversion symmetry. Secondly, we compared the fidelity when projectively measuring on different sites, and calculate the time required for the teleportation fidelity to reach matching values, Δt. Dividing the difference in lattice sites of the two measurements,

Δl, by the time lapse Δt, we independently obtain the value of the butterfly velocity. In practice we compared the fidelity when projectively measuring the EPR pair on the first site to the $(N-1)/2$th site such that $\Delta l = (N-1)/2 - 1$. Scanning this for different v in Fig. 3.10(b) we similarly find V_B saturates to approximately $v/2$ deep in to the chiral phase. Therefore, the measurement order of EPR pairs affects the speed of the teleportation protocol due to scrambling propagating through the system with butterfly velocity. This propagation time is given by $t_B = \Delta l / V_B \propto 1/v$. This differs from an effective model of a black hole such as the SYK model, which is defined by randomised all-to-all coupling, and therefore lacks a well defined notion of distance.

3.6 Chapter conclusions

In this chapter, we presented a local chiral model that maximises thermality. We accomplished this through the use of out-of-time-order correlators which allowed us to extract the associated Lyapunov exponent of the model. Analysing how this exponent varies with temperature, we quantified how thermal our model is. Crucially, by simply varying the couplings through the phase transition of the model, we see a regime switch where we transition from a generically scrambling model to that of a maximally scrambling model. This presented a degree of control over the level of thermality in the quantum system. Through numerical analysis of out-of-time-order correlators, we have provided compelling evidence that at the coupling regime representing the interior of the black hole, information encoded in the chain scrambles at an optimal rate.

With this, we also demonstrated how maximal scrambling and information loss is not the bane it may initially appear to be. We presented a realisation of the Hayden-Preskill quantum teleportation protocol within a binary black hole system simulated by a chiral spin-chain. This model successfully demonstrates the key ingredients of the protocol: the generation of entanglement through Hawking radiation and the implementation of optimal scrambling dynamics within the black holes. The optimal scrambling facilitates rapid information dispersal, reducing the overall time required for teleportation. By using these properties of the chiral spin-chain, we have shown that it is possible to achieve high-fidelity quantum teleportation even with relatively small system sizes.

We further quantified the propagation speed of quantum information using the butterfly velocity, finding that it aligns well with theoretical expectations and saturates to $v/2$ in the strongly interacting regime. The scrambling time and the butterfly velocity of the chiral spin-chain underscore the efficiency of the black hole teleportation protocol. All the characteristic timescales involved in black hole teleportation scale inversely with v, the coupling strength of the chiral spin-chain model. Comparative analyses with other

chaotic models – such as the mixed-field Ising model and the XY ladder – revealed that the chiral spin-chain outperforms them in terms of scrambling speed. This advantage is attributed to the chiral spin-chain's inherent ability to achieve optimal scrambling, thus minimising the time required for information recovery. Our findings establish the chiral spin-chain as a powerful platform for simulating quantum gravitational phenomena, particularly in the context of black hole information dynamics.

These findings pave the way for further exploration in several directions. Firstly, a theoretical analysis to determine the Lyapunov exponent of our chiral spin chain would complement our numerical findings. This would offer a deeper understanding of its chaotic behaviour. It would also be interesting to further examine this model in the context of extreme black holes, which correspond to zero temperature, $T = 0$. While the simulation techniques used can approach this limit, we cannot impose it exactly due to numerical instabilities. Nevertheless, the behaviour of our black hole simulator near $T \to 0$ can be faithfully reproduced. Additionally, investigating the quantum phase transition at $\frac{v}{2} \approx u$, where both the ground state and scrambling behaviour undergo significant changes, presents an intriguing topic for future research. This is particularly interesting due to the profound effect it has on the thermality of the system.

While one could argue that SYK has the capability to replicate the same results, the chiral spin-chain presents several key advantages. Firstly, it is non-local and disorder free in contrast to SYK, increasing its experimental simplicity and ability to be practically realised. Previous studies have shown the feasibility of realising chiral interactions in optical lattice systems [108,109]. This suggests the potential for experimental verification of the optimal scrambling behaviour and teleportation protocol in laboratory settings. Secondly, the chiral spin-chain black hole phenomena naturally arises from the continuum limit of the model. Meanwhile, the SYK model relies on the AdS/CFT correspondence for its emergent black hole behaviour. Finally, the chiral spin-model couplings allows one to naturally tune between a maximally thermalising regime and a free regime compared to the SYK model. This demonstrates a greater versatility and degree of control in the chiral spin-chain. Overall, the plausible experimental accessibility of our model opens new possibilities for studying thermalisation in a system that allows for fine control over the degree of thermality present.

Chapter 4

Evading and controlling thermalisation via quantum many-body scars

4.1 Chapter introduction

Previously, we introduced the concept of quantum thermalisation, its consequences, and the extreme limit of maximal information scrambling. While maximal scrambling can be advantageous in specific protocols like quantum teleportation, it often poses a challenge in practical quantum computing. In this chapter, we take a step back to explore mechanisms for avoiding thermalisation. Although integrable models offer one route to avoid thermalisation, they are notoriously fragile: real-world systems inevitably interact with environments, typically destroying integrability. Quantum many-body scarring [16, 18], introduced in Chapter 2, is an intermediate type of behaviour between full chaos and integrability.

Quantum many-body scars (QMBS) are a form of weak ergodicity breaking where select states in the Hilbert space are found to avoid thermalisation in an otherwise chaotic system. This undoubtedly changed the playing field by introducing a method to evade chaos without entering the integrable limit. This can be observed in the dynamics through quantum revivals – a phenomenon where the wave function $|\psi(T)\rangle$ at some time $t = T$ returns to its value at initial time $t = 0$ [168, 169], i.e., $|\langle\psi(0)|\psi(T)\rangle|^2 \sim O(1)$, has played an important role in understanding coherence properties of few-body or weakly-interacting quantum systems [170–181].The ability to engineer recurrent behaviour in more complex quantum systems is an important task as it allows one to study their long-term coherent evolution beyond the initial relaxation, while on the other hand, it

also provides insight into the emergence of statistical ensembles in closed systems that evolve according to the Schrödinger unitary dynamics.

Signatures of QMBSs were initially observed in experiments on Rydberg atom arrays [16], where energy cost due to the presence van der Waals interactions forbids two neighbouring atoms from both occupying excited states – a kinetic constraint known as the Rydberg blockade [15]. A famous limit of the Rydberg model which accounts for this blockade is colloquially known as the PXP model. For most initial states that are product states of spins in the computational basis, the PXP model exhibits fast equilibration without revivals. However, for special initial states, such as the Néel or "$\mathbb{Z}_2$" state, $|\mathbb{Z}_2\rangle \equiv |101010\ldots\rangle$, the PXP model undergoes a significant state transfer to the translated Néel state, $|010101\ldots\rangle$. These states feature a robust quantum revival with return probability on the order $\sim 70\%$ in relatively large systems of N=32 spins [19].

While the existence of quantum revivals in the PXP model has been been accounted for by an emergent su(2) spectrum-generating algebra [23], the origin of the effect remains unclear. Furthermore, what states ultimately exhibit such revivals also remains unanswered. For example, beyond the $\mathbb{Z}_2$ state, it was recently demonstrated that in the presence of a chemical potential, new scarring states begin to emerge in PXP [27, 182].

In this chapter, we provide a brief introduction to quantum many-body scarring and illustrate it using the paradigmatic PXP model [183, 184]. By then considering the PXP model in the presence of the chemical potential, our new results demonstrate the ubiquity of scarring by the construction of a dynamical phase diagram. We make use of the time-dependent variational principle (TDVP) to obtain a semiclassical interpretation of the quantum dynamics and the associated dynamical phase diagram. This diagram highlights the rich scarring behaviour of the PXP model and its curious interplay with quantum criticality, an otherwise unrelated phenomenon.

In our findings, we also show that even a highly entangled critical ground state retains the ability to avoid information scrambling. While we present only theory in this chapter, it is worth noting that this diagram has also successfully been reproduced experimentally using QuEra's Rydberg quantum simulator. This approach provides a method to evade and control thermalisation by the ability to continuously tune parameters of the system, such that certain states remain robustly non-thermal.

4.2 Quantum scars in the PXP model

4.2.1 The PXP model of Rydberg atoms

Quantum many-body scarring (QMBS) – a phenomenon introduced in Section 2.3 – was first observed in experiments with Rydberg atom arrays [16]. This system can be well

approximated by a chain of N coupled two-level atoms where, locally, the atoms can either be in the ground state $|0\rangle$, or an excited "Rydberg" state $|1\rangle$. Experimentally, this system is driven by lasers with a Rabi frequency Ω and on-site detuning Δ. Crucially, when atoms are in their excited states, they also interact via a van der Waals interaction, V, which decays with interatomic distance as $1/d^6$, where we work in units of lattice spacing $a = 1$ – see Fig. 4.1. With this, the lattice Hamiltonian takes the form

$$H_{\text{Ryd}} = \Omega \sum_i^N \sigma_i^x - \Delta \sum_i^N n_i + \sum_{i<j}^N V_{|i-j|} n_i n_j, \tag{4.1}$$

where $\sigma^x = |1\rangle\langle 0| + |0\rangle\langle 1|$, $n = |1\rangle\langle 1|$, and $V_{|i-j|} = \frac{V}{|i-j|^6}$.

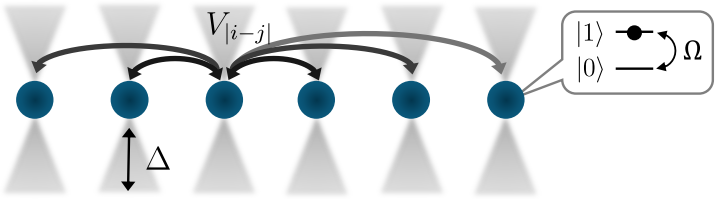

Figure 4.1: Schematic description of the 1D Rydberg model with Rydberg atoms trapped in optical tweezers. The local basis of each Rydberg atom is highlighted along with the effect of the van der Waals interactions and on-sight chemical potential. When the van der Waals interaction is tuned such that $V_1 \gg \Omega, \Delta \gg V_2$, it becomes energetically unfavourable for two neighbouring Rydberg excitations to exist.

While there are many parameter regimes in the Rydberg Hamiltonian, one of particular interest is when $V_1 \gg \Omega, \Delta \gg V_2$. Although this may initially appear to be a fine-tuned regime, it has been the focus of several experimental studies [16,46], due to the steep spatial decay of the van der Waals interaction. In this regime, energy cost due to van der Waals interactions strongly disfavours two neighbouring atoms occupying excited states – a form of kinetic constraint called the Rydberg blockade [15]. When the Rydberg blockade is strong, the atoms are described by an effective "PXP" model [183,184]. This is a one-dimensional chain of spin-1/2 degrees of freedom, where the spin-up state corresponds to a Rydberg atom occupying an excited state (and, similarly, for the spin-down state which denotes an atom in the ground state). Thus, the number of up spins translates into the number of Rydberg excitations, and we will use such nomenclature interchangeably. The PXP Hamiltonian for N atoms takes the form

$$H_{\text{PXP}}(\mu) = \Omega \sum_{j=0}^{N-1} P_{j-1} \sigma_j^x P_{j+1} + \mu \sum_{j=0}^{N-1} n_j. \tag{4.2}$$

In this chapter we set the Rabi frequency to $\Omega = 1$. The projector $P = |0\rangle\langle 0|$ implements

the constraint by preventing the Rabi flip from generating any neighbouring excitations. The complementary projector, $n = 1 - P$, again counts the number of excitations in the system and thus defines the chemical potential term, $\mu = -\Delta$. We will consider two types of boundary conditions for the Hamiltonian in Eq. (4.2). For analytical considerations and exact diagonalisation simulations, we will use periodic boundary conditions (PBCs) by identifying site $j + N \equiv j$. For matrix product state simulations in large systems, we will instead use open boundary conditions (OBCs), where the first and the last flip term are taken to be $X_0 P_1$ and $P_{N-2} X_{N-1}$, respectively.

Due to the kinetic constraint inherent in the PXP model, states containing two contiguous excitations ($|11\rangle$) are dynamically frozen, resulting in a highly disconnected Hilbert space. For the purpose of this study, we restrict to the largest connected sector consisting of states with no neighbouring excitations. As a result, the Hilbert space dimension of PXP scales as ϕ^N where $\phi = (1 + \sqrt{5})/2$ is the Golden Ratio [18, 185]. This immediately presents a numerical advantage in comparison to the full Rydberg model whose dimension scales as 2^N.

Further reduction in computational complexity can be achieved by exploiting the model's discrete symmetries: namely, translation and reflection. It is straightforward to verify that the PXP Hamiltonian commutes with both the translation operator T and the reflection operator P, i.e., $[H_{\text{PXP}}, T] = [H_{\text{PXP}}, P] = 0$. The translation operator T shifts all atoms by a single site, $j \to j + 1$, and we label its eigenstates using quantum number $k = 0, 1, 2, \ldots N - 1$. The reflection operator P flips the sites around the centre of the chain according to $j \to N - j$, and we label its eigenstates with quantum number $p = \pm 1$. In this work, we typically focus on the symmetry sector with $k = 0, p = +1$. It is important to note we can only resolve both symmetries for this choice of k and p as P only commutes with T when $k = 0$, since P maps $+k \to -k$ (for details, see [186, 187]).

Having resolved the symmetries, one can analyse the level statistics as described in Sec. 2.1.2. It is shown in Ref. [18] that the level statistics of the PXP model approach Wigner-Dyson distributions with increasing system size, indicating that the model is thermal in the conventional sense (both with and without the chemical potential term). As such, it is expected to obey the ETH for any generic initial state with eigenstates expected to exhibit thermal properties.

Nevertheless, in the absence of chemical potential ($\mu = 0$), the PXP model displays non-thermalising dynamics when initialised in the Néel state, $|\psi(0)\rangle = |\mathbb{Z}_2\rangle \equiv |1010...10\rangle$ [16]. Evolving this state with respect to the Hamiltonian in Eq. (4.2), one observes that the return probability periodically reaches values close to unity [18]. By contrast, other initial states exhibit fast equilibration, as expected in a chaotic system. This is evidenced in Fig. 4.2(a) where we compare a random product state to the Néel

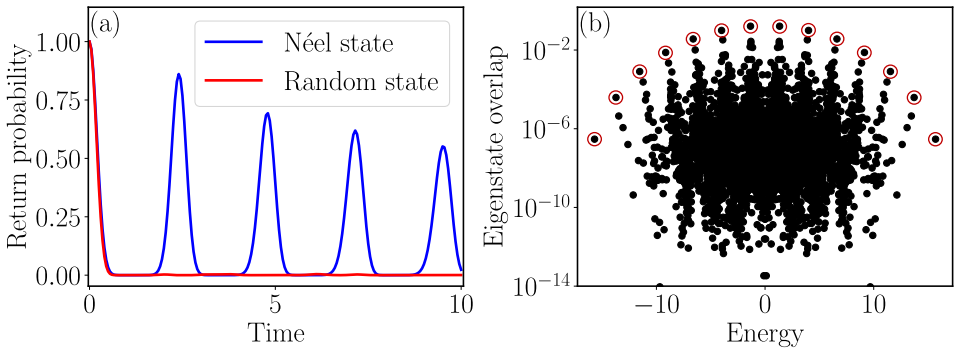

Figure 4.2: (a) The return probability when initialising with the Néel state (blue) and a random product state (red) and evolving over time with respect to the PXP Hamiltonian. We see the random product rapidly thermalises while the Néel state has persistent revivals, evading thermalisation. (b) The overlap between the Néel state and the eigenstates of H_{PXP} with $\mu = 0$. Anomalously high overlap is found with special eigenstates (circled in red) which are equidistant in energy. This energy separation is inversely proportional to the period of revivals found in (a). Results are obtained using ED with $N = 26$ in the $k = 0, p = +1$ symmetry sectors.

state. This atypical dynamics is also reflected in ergodicity breaking among a subset of eigenstates of the PXP model [19,188,189], even in the presence of perturbations [190,191] or in energy transport at infinite temperature [192]. It is precisely these select eigenstates that break the ETH by displaying non-thermal behaviour such as subvolume-law entropy scaling and non-thermal expectation values of local observables. They can be immediately observed by looking at the eigenstate overlap of $|\mathbb{Z}_2\rangle$, as shown in Fig. 4.2(b), which reveals anomalously high overlap with $N + 1$ eigenstates distributed evenly amongst the energy spectrum. The atypical revivals in the dynamics arise due to the presence of these special eigenstates which are approximately equidistant in energy.

Many attempts have been made to understand the atypical eigenstates in the PXP model. For example, it was shown that they can arise from an approximate representation of a weakly "broken" su(2) Lie algebra in PXP [23,24]. This is one of the underlying possible mechanisms discussed in Section. 2.3.1, a spectrum generating algebra, but in this instance, the embedded subspace is weakly coupled to the thermal bulk. The consequence of this algebra is an approximately decoupled su(2) subspace in which revivals primarily take place, while the wavefunction amplitude slowly leaks into the thermal bulk. However, the exact origin of the scarring behaviour and how this can be reproduced in other models remains an open question.

4.2.2 The role of chemical potential and equilibrium phase transition (EPT)

While our prior discussion primarily focused on pure PXP model, the chemical potential term μ has a significant impact on the physics, both in and out of equilibrium. As first noted in Ref. [193], when the chemical potential is tuned to $\mu_c \approx -1.31$, the ground state of the PXP model undergoes an Ising phase transition associated with a spontaneous breaking of $\mathbb{Z}_2$ symmetry [193–197], whose signatures have also been observed in the programmable Rydberg atom quantum simulators [46]. This equilibrium phase transition (EPT) is in the same universality class as the one induced by varying the quark mass in the Schwinger model of quantum electrodynamics in (1+1)-dimension [198]. The lattice formulation of the latter, known as the U(1) quantum link model, exactly maps to the PXP model in Eq. (4.2) for the case of spin-1/2 degrees of freedom [199].

Furthermore, a recent study [27] has found that new QMBS regimes can emerge in the PXP model when $\mu \neq 0$. One prominent example is the polarised state, $|0\rangle = |000....0\rangle$. While in the absence of chemical potential the $|0\rangle$ state is believed to thermalise [16], at non-zero chemical potential, it starts to revive, much like the $|\mathbb{Z}_2\rangle$ state. Moreover, periodic modulation of μ can enhance scarring behaviour and has been studied extensively [182, 200–205]. On the other hand, Ref. [19] studied the effect of perturbations (including the chemical potential) on the revivals of $|\mathbb{Z}_2\rangle$ state and tuning to $\mu \neq 0$ was found to hinder the non-ergodic behaviour. Thus, the impact of μ on QMBS is subtle and appears to be strongly state-dependent. Moreover, a natural question arises: is there any link between EPT and QMBS phenomena?

The EPT has a profound effect on the low-energy physics of the PXP model, but it is not obvious that it should directly impact QMBS, which manifest in the quench dynamics at infinite temperature. Nevertheless, Ref. [29] recently argued that there is a link between this EPT and QMBS. Namely, when tracing the eigenstates responsible for the quantum revival of the $|\mathbb{Z}_2\rangle$ state, Ref. [29] found that these states merge with the thermal bulk of the energy spectrum as the EPT is approached. Conversely, upon moving away from the EPT towards $\mu \to -\infty$, the degenerate ground states acquire high overlap with the $|\mathbb{Z}_2\rangle$ state and its partner translated by one site, $|\bar{\mathbb{Z}}_2\rangle \equiv |0101\ldots\rangle$. Thus, the $|\mathbb{Z}_2\rangle$ state can only thermalise as one approaches the EPT, suggesting a connection between QMBS and criticality. This was also demonstrated experimentally in the Bose-Hubbard quantum simulator [206]. Moreover, for the PXP model realised at a special resonance condition in the quantum Ising model, Ref. [207] argued that QMBS from the $|\mathbb{Z}_2\rangle$ state is smoothly connected to integrability by continuously turning off the constraint, induced by the longitudinal field.

In summary, the effect of μ on QMBS and the interplay with EPT has remained poorly

understood. For example, what if we initialise the system in the critical ground state at $\mu = \mu_c$ and then perform a quench by changing the value of μ – could this lead to QMBS dynamics? In the remainder of this chapter, we explore in depth the interplay of QMBS and EPT driven by varying the chemical potential. We will show that there is a close connection between the two effects, which can be used to create QMBS dynamics from a continuous family of initial conditions, including the critical ground state at EPT. To develop a deeper understanding of this connection, we will utilise a semiclassical approach based on time-dependent variational principle, introduced next.

4.2.3 Time-dependent variational principle and periodic orbits

Semiclassical methods have played an important role in the understanding of quantum scars in single-particle systems [208]. For example, in billiard systems, it was found that wavepackets are anomalously long-lived when prepared along the periodic orbits of the classical billiard, while they quickly disperse otherwise [25, 209]. In this chapter, we introduce a many-body generalisation of such an approach based on the Time-Dependent Variational Principle (TDVP) [210–212]. TDVP will allow us to establish a parallel between many-body dynamics in the PXP model [213–215] and the analogous dynamical phenomena of a single particle in a stadium billiard discussed in Chapter 2. Furthermore, the TDVP framework will provide a natural semiclassical language for investigating and interpreting the scarring behaviour in PXP from states other than $|\mathbb{Z}_2\rangle$ or $|0\rangle$, which become relevant in the presence of chemical potential.

The starting point of TDVP is to specify a variational manifold of states $\mathcal{M}$, parametrised by some continuous variable, and then project the Schrödinger dynamics into that manifold in a way that manifestly conserves the energy. The nature of states belonging to $\mathcal{M}$ determines to what extent we can interpret the dynamics as "semiclassical". For example, it would be simplest to consider a manifold spanned by tensor products of spin-coherent states. This would yield a "mean-field" description for the dynamics, where each atom precesses independently. However, the Rydberg blockade intrinsically builds in local correlations into the system, due to the fact that any neighbouring excitations, $|\ldots 11 \ldots\rangle$, are projected out of the Hilbert space. Ordinary spin-coherent states clearly violate this blockade condition.

Another way of defining a manifold, which naturally accommodates the Rydberg blockade constraint, is to take the span over MPS states with bond dimension χ controlling the amount of correlations necessary to capture the projected dynamics [212]. To simplify matters as much as possible, we will consider the dynamics to be spatially periodic with a (infinitely repeated) unit cell of size K (below we will be primarily interested in small unit cells with $K = 1, 2$). For a 1D chain of size N, the resulting MPS

ansatz is given by

$$|\psi_{\mathrm{MPS}}(\{\mathbf{x}\})\rangle = \sum_{\{\sigma\}} \mathrm{Tr}\Big(\prod_{m=0}^{N/K-1} A^{\sigma_{1+Km}}(\mathbf{x}_1) A^{\sigma_{2+Km}}(\mathbf{x}_2) A^{\sigma_{K+Km}}(\mathbf{x}_K) \Big) |\sigma_1 \sigma_2 \sigma_3 \cdots \sigma_N\rangle \,. \quad (4.3)$$

Here $A^{\sigma}(\mathbf{x_i})$ are $(\chi \times \chi)$-dimensional matrices that depend on variational parameters $\mathbf{x_i} = (\theta_i, \phi_i)$, where the angles θ_i, ϕ_i are akin to the Bloch sphere angles of each spin in the unit cell. The physical degree of freedom $\sigma_i = 0, 1$ labels the basis states of a single spin. Following Refs. [213, 216], in order to make things analytically tractable, we will restrict to $\chi = 2$ and choose

$$A^1(\theta_i, \phi_i) = \begin{pmatrix} 0 & e^{-i\phi_i} \\ 0 & 0 \end{pmatrix}, \quad A^0(\theta_i, \phi_i) = \begin{pmatrix} \cos\theta_i & 0 \\ \sin\theta_i & 0 \end{pmatrix}. \quad (4.4)$$

Due to $A^1 A^1 = 0$, this ansatz ensures that configurations with neighbouring spin-up are forbidden, thus our manifold $\mathcal{M} = \mathrm{span}\{|\psi_{\mathrm{MPS}}(\mathbf{x})\rangle \, |\forall \mathbf{x}\}$ respects the Rydberg blockade.

With the choice of ansatz in Eqs. (4.3)-(4.4) and setting $K = 1$, we are left with only two variational degrees of freedom, (θ, ϕ). Choosing $(0, 0)$ recovers the state $|0\rangle \equiv |000\ldots\rangle$, while $(\pi/2, \pi/2)$ corresponds to the equal-weight superposition of the two Néel states related by single-site translation,

$$\left|\mathbb{Z}^+\right\rangle \equiv \frac{1}{\sqrt{2}} \left(|\mathbb{Z}_2\rangle + \left|\bar{\mathbb{Z}}_2\right\rangle \right). \quad (4.5)$$

Note that, with $K = 1$ unit cell periodicity, the states $|\mathbb{Z}_2\rangle$, $\left|\bar{\mathbb{Z}}_2\right\rangle$ do not individually belong to the manifold. Instead, if we extend the ansatz to $K = 2$, then $(\theta_1, \theta_2) = (0, \pi/2)$ recovers the $|\mathbb{Z}_2\rangle$ state. Thus, our manifold with bond dimension $\chi = 2$ captures the initial product states that we expect to play an important role for QMBS dynamics in the PXP model.

After defining the manifold, the next step is to minimise the difference between exact Hamiltonian dynamics and its projection to the manifold [211],

$$\min_{\{\mathbf{x}\}} \left\| i\hbar \frac{\partial}{\partial t} |\psi_{\mathrm{MPS}}(\{\mathbf{x}\})\rangle - H |\psi_{\mathrm{MPS}}(\{\mathbf{x}\})\rangle \right\|. \quad (4.6)$$

This results in the Euler-Lagrange equations of motion for the classical variables $\mathbf{x}$ [212]. In the case of the PXP model, this step can be performed analytically in the limit of $N \to \infty$ to obtain the equations of motions for the θ and ϕ angles, see Appendix C.2 for $K = 1$ and Refs. [213, 216] for some $K = 2$ and $K = 3$ examples. Integrating this system of differential equations yields the trajectory in $\mathcal{M}$ taken by $|\psi_{\mathrm{MPS}}(\{\boldsymbol{\theta}, \boldsymbol{\phi}\})\rangle$ during the

course of quantum evolution. Fig. 4.3 shows a pictorial representation of the $K = 2$ manifold and the projection of exact dynamics into it, for the cases of interest in the bare PXP model without any chemical potential.

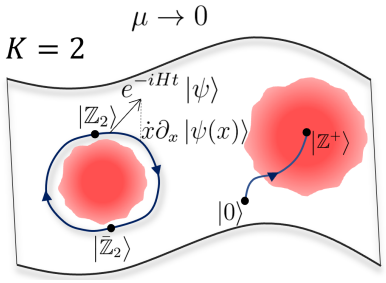

Figure 4.3: Sketch of the TDVP manifold $\mathcal{M}$ for the PXP model in the absence of chemical potential ($\mu \to 0$). Red regions represent areas of high leakage where the TDVP approximation breaks down, as quantified by Eq. (4.7). The Néel state is denoted by $|\mathbb{Z}_2\rangle \equiv |1010\ldots\rangle$ and its translated partner – the anti-Néel state is $|\bar{\mathbb{Z}}_2\rangle \equiv |0101\ldots\rangle$, while $|\mathbb{Z}^+\rangle = (|\mathbb{Z}_2\rangle + |\bar{\mathbb{Z}}_2\rangle)/\sqrt{2}$. The polarised state is $|0\rangle \equiv |0000\ldots\rangle$. For a two-site unit cell $K = 2$ and $\mu = 0$, the $|\mathbb{Z}_2\rangle$ state lies on a periodic trajectory identified in Ref. [213]. We also illustrate the trajectory of the $|0\rangle$ state, which is predicted by TDVP to evolve to $|\mathbb{Z}^+\rangle$; however, this point lies within a region of high leakage where the TDVP dynamics does not accurately describe the quantum evolution. This is consistent with the $|0\rangle$ state thermalising at $\mu = 0$.

Importantly, beyond equations of motion, it is possible to estimate "quantum leakage": the difference between exact quantum evolution and its projection into the manifold [213]. Quantum leakage, γ, is defined as the instantaneous rate at which the exact wave function leaves $\mathcal{M}$:

$$\gamma^2 = \lim_{N\to\infty} \frac{1}{N} \left\| iH\,|\psi_{\mathrm{MPS}}(\mathbf{x})\rangle + \sum_j \dot{x}_j \partial_{x_j}\,|\psi_{\mathrm{MPS}}(\mathbf{x})\rangle \right\|^2 . \tag{4.7}$$

Red regions in Fig. 4.3 indicate areas of large γ^2. In these high-leakage regions, the instantaneous TDVP dynamics is expected to poorly capture the exact dynamics. Consequently, trajectories passing through such regions will generally be of limited accuracy. On the other hand, as first noted in Ref. [213], the special property of the PXP phase space is that it has regions of remarkably *low* leakage, such as the region traversed by the semiclassical orbit associated with the $|\mathbb{Z}_2\rangle$ state. This is depicted in Fig. 4.3 where the orbit is sketched, lying within a region of low leakage. Note that, in general, there can exist *multiple* periodic orbits within the same manifold [214]. Having established this framework, we will use it below to analyse the scarring behaviour in the presence of chemical potential.

4.3 Dynamical phase diagram of the PXP model

By 'dynamical phase diagram' of the PXP model we refer to the global quench of the chemical potential from some initial value, $\mu_{\rm i}$, to an arbitrary final value, $\mu_{\rm f}$. Specifically, we prepare the ground state of the PXP Hamiltonian in Eq. (4.2) at $\mu_{\rm i}$ and then evolve that state with the Hamiltonian corresponding to $\mu_{\rm f}$:

$$|\psi(0)\rangle \equiv |\mathrm{GS}(\mu_{\rm i})\rangle \to |\psi(t)\rangle = e^{-\frac{i}{\hbar}tH_{\rm PXP}(\mu_{\rm f})}\,|\psi(0)\rangle\,. \tag{4.8}$$

This setup provides a means of probing out-of-equilibrium dynamics from more complex initial states beyond $|\mathbb{Z}_2\rangle$ or $|0\rangle$, which had been accessed in previous experiments by taking the limits $\mu_i \to \pm\infty$.

As indicated in Eq. (4.8), we assume a closed system evolving under unitary Schrödinger dynamics. Since the energy level spacings in the PXP model are expected to obey the Wigner-Dyson distribution for all values of μ [18, 183], the nonequilibrium dynamics induced by quenching μ should be chaotic [60]. In particular, quenching the chemical potential by a large amount $\sim$O(1) should initialise the system in a generic high-temperature state, which is expected to lead to rapid thermalisation according to the Eigenstate thermalisation Hypothesis (ETH) [1,2,217]. This means that the expectation value of any local observable should converge towards the value predicted by the canonical ensemble within any symmetry-resolved sector of the many-body Hilbert space. Deviation from this prediction, i.e., ergodicity breaking, can be detected through a number of dynamical probes, two of which we utilise.

One probe of ergodicity breaking, convenient in the context of QMBS, is quantum fidelity or return probability of the wavefunction to its initial value, as defined in Eq. (3.9). For a thermalising initial state, $\mathcal{F}(t)$ rapidly drops to a value close to zero and remains exponentially small in system size at late times. Therefore, if the average fidelity over a time interval $\gg \Omega^{-1}$ is much larger than $\sim$ O(exp($-N$)), we expect non-ergodic behaviour. However, one should exclude trivial cases such as $\mu_{\rm i} \approx \mu_{\rm f}$ when the ground state of $H_{\rm PXP}(\mu_{\rm i})$ is approximately an eigenstate of $H_{\rm PXP}(\mu_{\rm f})$, as this would lead to the system getting "stuck" in an eigenstate, with fidelity $\mathcal{F}(t) \approx 1$ and potentially never decaying. To avoid such cases, we compute the difference $\delta\mathcal{F}$ between minimal fidelity and maximal fidelity over a time window $t \in [t_0, t_1]$, with t_0=1 and t_1=20. This window is large enough to exceed the initial relaxation on the scale $\gtrsim \Omega^{-1}$ (thus excluding the high fidelity near $t = 0$), yet small enough ($t_1 \lesssim N/\Omega$) to be free of the boundary effects.

The obtained $\delta\mathcal{F}$ in the $\mu_{\rm i} - \mu_{\rm f}$ plane is shown in Fig. 4.4(a). The fidelity has been evaluated in a system of $N = 51$ atoms using matrix product state (MPS) [219] simulations based on the algorithm in Ref. [218], and we have checked that the results

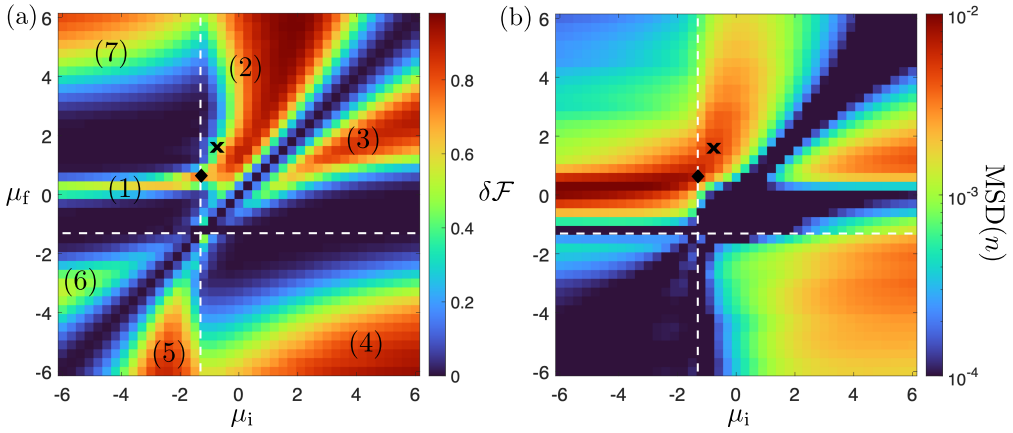

Figure 4.4: Dynamical phase diagram for global quenches starting in the ground state of $H_{\mathrm{PXP}}(\mu_{\mathrm{i}})$ and evolving with $H_{\mathrm{PXP}}(\mu_{\mathrm{f}})$. (a) The difference between maximal and minimal revival fidelity $\delta\mathcal{F}$ over time interval $1 \leq t \leq 20$ following the quench. Regions with strong fidelity revivals have been enumerated (see the text for details). (b) Same as (a) but the colour bar showing the deviation of the excitation density from the thermal value, Eq. (4.9). Data is obtained using MPS simulations [218] for a chain of $N = 51$ atoms with OBCs, maximum bond dimension $\chi = 128$ and time step $\delta t = 0.025$. Dashed lines mark the EPT at $\mu_{\mathrm{c}} \approx -1.31$. In both plots, the cross marks the point $(\mu_{\mathrm{i}} = -0.76, \mu_{\mathrm{f}} = 1.60)$ that will be analysed in Sec. 4.4. The diamond marks the optimal reviving point in the $\mu_{\mathrm{i}} = \mu_{\mathrm{c}}$ plane, which will be discussed in Sec. 4.5.

agree closely with exact diagonalisation for systems with $N < 30$ atoms. We note that $t_0 = 1$ in Fig. 4.4(a) was chosen to be just slightly longer than the initial relaxation period, as modulating μ alters the period of the fidelity revivals. Setting $t_0 > 1$ results in a qualitatively similar phase diagram, but with a reduced overall scale for $\delta\mathcal{F}$, as the window with larger t_0 may miss the first (and typically the largest) revival peak.

Before we comment on the interesting regimes of the phase diagram, we note that we have also computed the deviation of an observable expectation value from the thermal ensemble prediction, shown in Fig. 4.4(b). This provides a complementary probe of ergodicity breaking that is more amenable to experimental measurements. For the observable, we chose the density of excitations in the system, $n = (1/N)\sum_{j=1}^{N} n_j$, which is readily available in existing experimental setups [16, 27]. After quenching the system, we compute the integrated mean-square deviation of the excitation density from the thermal value over the time window between $t_0 = 10$ and $t_1 = 20$,

$$\mathrm{MSD}(n) = \frac{1}{t_1 - t_0} \int_{t_0}^{t_1} |\langle\psi(t)|n|\psi(t)\rangle - n_{th}|^2 \; dt. \tag{4.9}$$

The thermal value is defined as

$$n_{th} = \mathrm{Tr}(\rho_{th} n),\ \rho_{th} = \exp(-\beta H)/\mathcal{Z}\ \mathcal{Z} = \mathrm{Tr}\exp(-\beta H), \tag{4.10}$$

where the inverse temperature β is determined from the condition

$$\langle\psi(0)|H_{\mathrm{PXP}}(\mu_{\mathrm{f}})|\psi(0)\rangle = \mathrm{Tr}(\rho_{th} H_{\mathrm{PXP}}). \tag{4.11}$$

The plot of MSD(n) is shown in Fig. 4.4(b), where the bright non-ergodic regions match those of high fidelity in Fig. 4.4(a). The colour contrast is stronger in the fidelity plot due to the exponential sensitivity of that quantity. A few distinct regimes where fidelity displays large-amplitude oscillations have been marked by (1)-(7) in Fig. 4.4(a). These regions will be analysed in detail in the subsequent sections. There, we will argue that regions (1), (2) and (3) can be identified as QMBS regimes. Regions (1) and (3) fall under the "universality class" of $|\mathbb{Z}_2\rangle$ and $|0\rangle$ QMBS behaviour, as we explain in Sec. 4.2.3. On the other hand, while the dynamics in region (2) has some similarities with regions (1) and (3), in Sec. 4.4 we will highlight the distinctions of this QMBS regime. As it turns out, regions (4), (5), (6) and (7) have a simple origin, which will be explained briefly in Appendix C.1.

A few comments are in order. The QMBS fidelity appears to vary smoothly between regions (1) and (2) in Fig. 4.4(a), while they are separated by the EPT (indicated by the dashed line). In fact, we find the most robust revivals correspond to the ground state precisely at the EPT point (highlighted by the diamond in Fig. 4.4). That is to say, although $\delta\mathcal{F}$ may be smaller than other regions, the revivals decay more slowly over time, and this behaviour persists with increasing N. This intriguing case will be addressed in detail in Sec. 4.5. Here we note that we have confirmed the existence of QMBS across the critical point in much larger systems ($N \leq 400$ spins) using MPS numerics. This is in contrast to the $\mu_{\mathrm{f}} = \mu_{\mathrm{c}}$ case, where we see no ergodicity breaking in Fig. 4.4(a), as also expected from Refs. [29, 206].

In summary, our dynamical phase diagram confirms that the previously known scarring regimes, associated with $|\mathbb{Z}_2\rangle$ and $|0\rangle$ states (as discussed in Section. 4.2.2), indeed break down when approaching the EPT, either via $\mu_{\mathrm{i}} \to \mu_{\mathrm{c}}$ or $\mu_{\mathrm{f}} \to \mu_{\mathrm{c}}$, in agreement with Refs. [29, 206]. However, we also find a new QMBS regime corresponding to the initial state being the ground state near the EPT. Using the time-dependent variational principle (TDVP) framework for QMBS, developed in Ref. [213], we can identify a semi-classical picture behind QMBS dynamics. Across much of the phase diagram away from the EPT point, the QMBS dynamics can be understood in terms of a periodic trajectory that passes through the $|0\rangle$ state, with the radius of the trajectory controlled by the

chemical potential. Allowing for a continuous family of initial states – the ground states of $H_{\mathrm{PXP}}(\mu_{\mathrm{i}})$ – we find surprisingly robust QMBS signatures at intermediate times that smoothly bridge across the EPT. In the subsequent Sections 4.4 and 4.5, we discuss in detail the most interesting parts of the phase diagram, i.e., regions (1), (2), (3) and the EPT, while the other parts are relegated to Appendix C.1.

4.4 Scarring in gapped regimes in the phase diagram

In this section we focus on regions (1), (2), and (3) of the phase diagram in Fig. 4.4, in particular for the values of the chemical potential away from the EPT. Based on the discussion of TDVP in Sec. 4.2.3, the origin of regions (1) and (3) can be understood by examining the form of the PXP ground state in the presence of chemical potential. When $\mu_{\mathrm{i}} \to -\infty$, excitations are favoured and the ground state is (for PBCs) a superposition of the two Néel states, $|\mathbb{Z}^+\rangle$ in Eq. (4.5). By contrast, $\mu_{\mathrm{i}} \to \infty$ penalises excitations, therefore the ground state is the polarised state $|0\rangle$. The superposition state $|\mathbb{Z}^+\rangle$ is known to display revivals when quenched to $\mu_{\mathrm{f}} = 0$ [19], while the polarised state revives when quenched with $\mu_{\mathrm{f}} \neq 0$ as shown more recently in Refs. [27,182]. By continuity, these limiting cases explain the mechanism behind revivals in regions (1) and (3) of Fig. 4.4.

4.4.1 TDVP interpretation of the dynamical phase diagram

We can utilise TDVP to understand much of the PXP dynamical phase diagram in Fig. 4.4 by considering the trajectory of the polarised state in the manifold introduced in Section 4.2.3. Fig. 4.5 sketches this trajectory for $K = 1$ unit cell and three different values of the chemical potential μ.

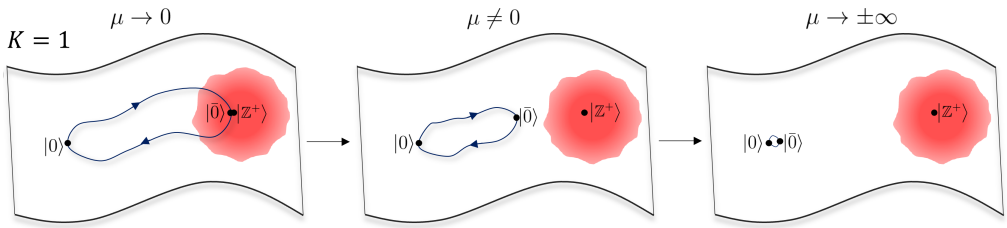

Figure 4.5: Sketch of the TDVP manifold $\mathcal{M}$ for the PXP model with $K = 1$ unit cell and chemical potential μ. The notations are the same as in Fig. 4.3. For $\mu = 0$, the $|0\rangle$ trajectory is periodic but passes through a region of high leakage. When $\mu \neq 0$, the trajectory shrinks, whilst gradually exiting the high leakage area, and QMBS dynamics starts to emerge in the full system. In this regime, the QMBS dynamics can be seen as an oscillation between $|0\rangle$ and a new state, $|\bar{0}(\mu)\rangle$, defined in Eq. (4.12). Finally, in the extreme $\mu \to \pm\infty$ limit, the orbit shrinks to a point and the dynamics is frozen.

Within TDVP, a periodic orbit exists even for $\mu = 0$. However, the orbit passes through the superposition of the two Néel states, $|\mathbb{Z}^+\rangle$ – a point which is located in the high-leakage region. The TDVP dynamics is therefore not a good approximation in this case, which accounts for the absence of revivals observed in the full quantum dynamics. The addition of a finite chemical potential μ, as shown in the middle panel of Fig. 4.5, contracts the trajectory and pushes it into a low-leakage region and effectively allowing the revivals from the polarised state to emerge. As we will explain in Sec. 4.4.3, in this intermediate range of μ, the ground state of $H_{\mathrm{PXP}}(\mu')$ (where $\mu \neq \mu'$) occupies an antipodal position on the orbit, corresponding to a chemical-potential dependent state we label $|\bar{0}(\mu)\rangle$, given by Eq. (4.4) for unit cell size $K = 1$:

$$|\bar{0}(\mu)\rangle = |\psi_{\mathrm{MPS}}(\theta_{\max}, \phi_{\max})\rangle\,, \tag{4.12}$$

with angles $(\theta_{\max}, \phi_{\max})$ denoting the antipodal point in the TDVP orbit of the initial polarised state, see Fig. 4.5. As μ has the effect of deforming the trajectory, the antipodal angles also depend on μ, in a way that will be specified in Eq. (4.17) below. Note that the sign of μ has no effect on the deformation of the particular orbit discussed here [220]. Finally, in the extreme limit $\mu \to \pm\infty$, the trajectory is restricted to the vicinity of the initial state and the dynamics is effectively frozen, as shown in the right panel of Fig. 4.5. In the following subsection, we focus on the more interesting region (2) where the pre-quench initial state is an entangled state with low overlap on both $|0\rangle$ and $|\mathbb{Z}_2\rangle$ states. Nevertheless, this same TDVP analysis will prove useful due to the connection between the initial state and $|0\rangle$.

4.4.2 Scarring in region (2) of the phase diagram

We focus on region (2) of the phase diagram in Fig. 4.4 and pick $(\mu_{\mathrm{i}}^*, \mu_{\mathrm{f}}^*) = (-0.76, 1.60)$ as an illustrative point in this region, marked by the cross in Figs. 4.4(a)-(b). QMBS dynamics at this point was first noted in Ref. [27] and here we will characterise it in detail and explain its origin. The evolution of fidelity and overlap with the polarised and Néel state are shown in Fig. 4.6(a), where persistent fidelity revivals can be observed while the overlap with $|\mathbb{Z}_2\rangle$ remains negligible throughout the evolution. Curiously, while the initial state at μ_{i}^* has low overlap with $|0\rangle$, the evolved state does develop a relatively high overlap with $|0\rangle$ state, approximately half way between the main revival peaks – see the green line in Fig. 4.6(a). This is reminiscent of the $|\mathbb{Z}_2\rangle$ state, which in the pure PXP model undergoes state transfer to $\left|\bar{\mathbb{Z}}_2\right\rangle$ at half the revival period [213]. This implies that the ground state of $H_{\mathrm{PXP}}(\mu_{\mathrm{i}}^*)$ is related to the polarised state.

Another tell-tale signature of QMBS is a slower growth of entanglement entropy

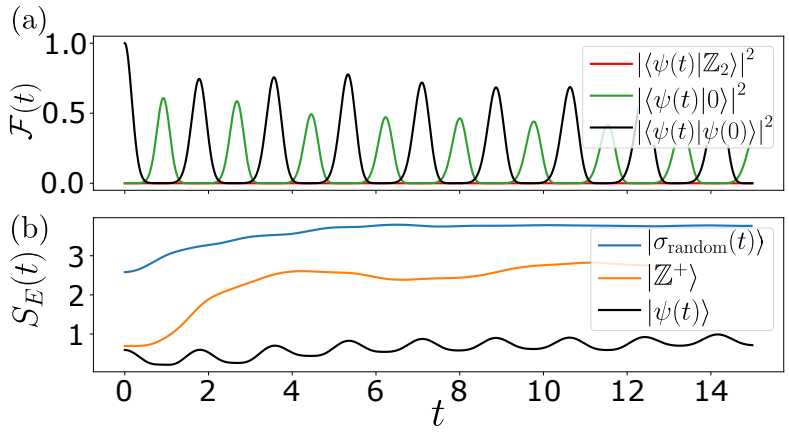

Figure 4.6: Dynamics of quantum fidelity and entanglement entropy, following a global quench of the chemical potential, $\mu_{\text{i}}^* = -0.76 \to \mu_{\text{f}}^* = 1.6$, corresponding to the point marked by the cross in Fig. 4.4(a). Quantum fidelity for the initial state $|\psi(0)\rangle$ defined as the ground state of the PXP model with μ_{i}^*. Also shown is the projection of the time-evolved state on the $|\mathbb{Z}_2\rangle$ and $|0\rangle$ states. While the overlap with the $|\mathbb{Z}_2\rangle$ state is low throughout the evolution, the overlap with $|0\rangle$ reaches relatively high values between the main revival peaks. (b) Growth of entanglement entropy, $S_E(t)$, for the same initial state $|\psi(0)\rangle$ as in (a), as well as for a random state $|\sigma_{\text{Random}}\rangle$ and $|\mathbb{Z}^+\rangle$ state. The initial state $|\psi(0)\rangle$ has strongly suppressed entanglement growth compared to the other cases. Data is for system size $N = 28$ obtained using exact diagonalisation with PBCs.

$S_E(t)$, as defined in Eq. (2.6), for special initial states. We plot the dynamics of $S_E(t)$ in Fig. 4.6(b). Compared to both $|\mathbb{Z}^+\rangle$ and a random state in the constrained Hilbert space, $|\sigma_{\text{Random}}\rangle$, the entropy growth from the ground state of $H_{\text{PXP}}(\mu_{\text{i}}^*)$ is strongly suppressed. For the latter state, we observe clear oscillations in the time series of $S_E(t)$, reminiscent of entropy dynamics in the PXP model in the absence of chemical potential [18].

We emphasise that the special point $(\mu_{\text{i}}^*, \mu_{\text{f}}^*)$ is representative of the entire region (2) in the phase diagram, where similar QMBS phenomenology is numerically observed. In the following subsection, we use TDVP to garner a further understanding of this QMBS regime from a semiclassical point of view.

4.4.3 TDVP analysis of scarring in region (2)

Before we apply TDVP to describe the dynamics in Fig. 4.6, we need to make sure that the PXP ground state in the presence of chemical potential is indeed represented within the manifold spanned by states in Eq. (4.3). We discuss this further in Appendix C.3, where we find that, for a unit cell size $K = 1$ at system size $N = 20$, most states belonging to the TDVP manifold ($> 90\%$ of them) can be approximated with better than 98% accuracy by a ground state of Eq. (4.2) with the addition of a phase pulse.

With suitable modifications, numerical evidence suggests that TDVP states with $K \geq 2$ can also be successfully prepared.

Having established that our pre-quench ground state at arbitrary μ_{i} can be approximately mapped to an MPS state in the $K = 1$ TDVP manifold for some variational parameters (θ, ϕ), we now proceed to describe the dynamics from this initial state using the classical dynamical system defined by $(\theta(t), \phi(t))$. From Eq. (4.6), one can derive the TDVP equations of motion for $K = 1$ and arbitrary chemical potential μ (see Appendix C.2 for details):

$$\dot{\theta} = -\cos\theta\cos\phi\left(1+\sin^2\theta\right), \tag{4.13}$$

$$\dot{\phi} = \mu + \frac{\sin\phi}{\sin\theta}\left(1-4\sin^2\theta-\sin^4\theta\right). \tag{4.14}$$

Unlike the special case $\mu = 0$, where ϕ variables can be set to zero in the flow-invariant subspace [213], for general values of μ one must consider both θ and ϕ simultaneously [214].

Integrating Eqs. (4.13)-(4.14), we plot the phase space θ, ϕ portrait for the chemical potential value $\mu_{\mathrm{f}} = 1.6$ in Fig. 4.7(a). The greyscale background indicates the quantum leakage at any given point in the manifold,

$$\gamma^2 = \frac{\sin^6\theta}{1+\sin^2\theta}, \tag{4.15}$$

which only depends on θ variable (see Appendix C.2). By integrating the equations of motion for $\mu_{\mathrm{f}} = 1.6$, starting from the polarised state $|\psi_{\mathrm{MPS}}(0,0)\rangle$, we obtain the trajectory plotted in red colour in Fig. 4.7(a). Generally, for any $|\mu_{\mathrm{f}}| \neq 0$, the polarised state has a periodic orbit within TDVP. When μ_{f} is large, the orbit is pinned around $\theta = 0$. Decreasing $|\mu_{\mathrm{f}}|$ stretches the orbit until the maximal point in the trajectory eventually tends towards the $|\mathbb{Z}^+\rangle$ superposition state, $(\theta, \phi) \equiv (\pi/2, \pi/2)$. Due to the quantum leakage gradient, the $|\mathbb{Z}^+\rangle$ point is not reached for any finite time. This is consistent with the lack of revivals from the polarised state in the full quantum dynamics for sufficiently small values of μ_{f}. Thus, we conclude that the orbit corresponding to the cross in Fig. 4.4(a) is a compromise between two competing effects: the orbit is sufficiently stretched so that it has non-trivial dynamics, while at the same time, by being not stretched too much, it can avoid the large leakage in the vicinity of $|\mathbb{Z}^+\rangle$ state.

To verify this picture across the entire region (2), we study the projection of the PXP ground state at μ_{i}, $|\mathrm{GS}(\mu_{\mathrm{i}})\rangle$, to the TDVP manifold. We numerically maximise the overlap $|\langle\psi_{\mathrm{MPS}}(\theta,\phi)|\mathrm{GS}(\mu_{\mathrm{i}})\rangle|^2$, with the MPS state given in Eq. (4.3). We plot the resulting (θ, ϕ) phase space coordinates for a variety of μ_{i} in Fig. 4.7(a), where the coloured dots correspond to the ground states from our phase diagram in Fig. 4.4(a).

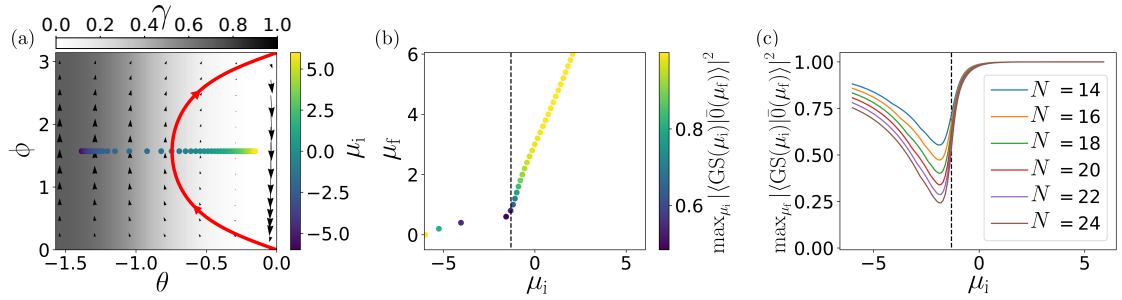

Figure 4.7: (a) Phase space portrait of quantum dynamics within the $K = 1$ TDVP manifold for the PXP model with μ_f=1.6 where the arrows demonstate the trajectories present in the manifold. Grey shading indicates quantum leakage (darker regions represent larger leakage). Coloured symbols indicate the location of the PXP ground states corresponding to various μ_i indicated on the colour bar while the trajectory of the $|0\rangle$ state for the given value of μ_f is highlighted in red. We see that the ground states with $\mu_i \approx -0.76$ lie close to the point which is antipodal to the $|0\rangle$ state in its trajectory. With changing μ_f, this trajectory either expands or compresses, meaning all ground states will lie on this antipodal point for some μ_f. (b) In region (2) of the phase diagram, for a given μ_f, $|\bar{0}(\mu_f)\rangle$ state is well-approximated by a detuned PXP ground state with some μ_i. colour bar shows the highest overlap between the $|\bar{0}(\mu_f)\rangle$ state, given by Eq. (4.17) for a range of fixed $\mu_f \in [-5, 5]$, and the family of ground states of $H_{\mathrm{PXP}}(\mu_i)$. Dashed lines denote the EPT. For negative chemical potentials, especially relevant for region (1) of the phase diagram, the mapping requires an additional phase pulse, as described in Appendix C.3. (c) Matching the detuned PXP ground state with a $|\bar{0}\rangle$ state becomes progressively more difficult at the critical point (dashed line) as system size N is increased. In contrast to panel (b), here we fix the PXP ground state at μ_i and vary μ_f to find the optimal $|\bar{0}(\mu_f)\rangle$ state with the highest overlap. All plots are obtained using exact diagonalisation with PBCs and system size $N = 20$ in panels (a)-(b).

As expected, some of the ground states are "distant" from $|\mathbb{Z}^+\rangle$ or $|0\rangle$ but tend towards either in their respective limits. All successfully optimised ground states lie on the same ϕ plane in Fig. 4.7(a). Consequently, the deformation of the trajectory means they will correspond to some maximum point μ_f on the polarised state trajectory, denoted by the state $|\bar{0}\rangle$. By analogy with the Néel state, whose translation partner – the anti-Néel state – displays identical scarring behaviour [97], here we have a similar relation between $|0\rangle$ and $|\bar{0}(\mu_f)\rangle$ states. The main difference with the anti-Néel state is that $|\bar{0}\rangle$ state depends on the value of μ_f.

To substantiate this further, we analytically derive the phase-space coordinates corresponding to $|\bar{0}(\mu_f)\rangle$. Using Eq. (4.13), we see that the turning point in the gradient of θ along the trajectory is governed by $\cos\phi$. A sign flip therefore must occur when $\phi = \pm\pi/2$. Because energy is exactly conserved along a TDVP trajectory, $|\bar{0}(\mu_f)\rangle$ must have the same energy as the polarised state. For states belonging to $K = 1$ TDVP

manifold, the energy density is given by

$$E(\theta,\phi)/N = \frac{\sin\theta}{1+\sin^2\theta}\left(\mu_{\rm f}\sin\theta + 2\cos^2\theta\sin\phi\right). \tag{4.16}$$

For the polarised state, $E(0,0)=0$ and, setting $\phi_{\max}=\pi/2$, allows us to determine the $\theta_{\max}$ coordinate of the $|\bar{0}(\mu_{\rm f})\rangle$ turning point:

$$\sin\theta_{\max} = \left(|\mu_{\rm f}| - \sqrt{\mu_{\rm f}^2+16}\right)/4. \tag{4.17}$$

In Fig. 4.7(b) we test the overlap of the state $|\bar{0}(\mu_{\rm f})\rangle$, with the MPS angles given by Eq. (4.17), against the family of ground states of $H_{\rm PXP}(\mu_{\rm i})$. We scan through a set of values $\mu_{\rm f}\in[-5,5]$ and, for each $\mu_{\rm f}$, plot the maximum overlap obtained by maximising over $\mu_{\rm i}$. Doing so, we confirm that the ground states within region (2) of the phase diagram have high overlap with the antipodal state in the polarised state trajectory in the TDVP manifold. Although $\mu_{\rm f}<0$ is not particularly relevant for region (2), we note that the optimisation fails there. This, however, can be fixed by including an additional phase pulse, as explained in Appendix C.3. Comparing Fig. 4.7(b) to Fig. 4.4(a), we see a striking correspondence between the successful optimisation and region (2) in the phase diagram. This confirms that the QMBS phenomena in region (2) are indeed associated with $|\bar{0}(\mu_{\rm f})\rangle$ state.

Finally, in Fig. 4.7(c) we study the system size scaling of the mapping between the PXP ground state with chemical potential and states in the TDVP manifold. We scan for the maximal overlap of the ground state at some $\mu_{\rm i}$ with the set of all $|\bar{0}(\mu_{\rm f})\rangle$ states in the interval $\mu_{\rm f}\in[-20,20]$. Remarkably, for the vast majority of region (2) when $\mu_{\rm i}>0$, we see a near perfect overlap between the ground state and $|\bar{0}(\mu_{\rm f})\rangle$, independent of system size. This suggests that the TDVP state captures well the PXP ground state in region (2). Nevertheless, in Fig. 4.7(c) we also observe a breakdown of the mapping at the EPT point $\mu_{\rm i}=\mu_{\rm c}$. This is expected since the ground state at the critical point develops a diverging entanglement entropy and the $\chi=2$ MPS approximation must deteriorate as system size is increased, since an area-law state cannot capture the critical ground state in the thermodynamic limit. This naturally leads to the question: is the observed scarring in the critical ground state an artefact of finite size and what is its origin?

4.5 Interplay between scarring and criticality

Finally, we focus on the nature of QMBS regime when quenching from the critical ground state at $\mu_{\rm i}=\mu_{\rm c}$. Despite the complexity of this state, we find robust signatures of ergodicity breaking. Long-time memory retention from states in energy close to an EPT

has previously been observed in the LMG model [221, 222]. We find similar behaviour between regions (1) and (2) in Fig. 4.4(a). For example, by fixing $\mu_\mathrm{i} = \mu_\mathrm{c}$ and scanning μ_f to determine the largest $\delta\mathcal{F}$, we find the most robust revivals occur at $\mu_\mathrm{f} = 0.633$ – a point marked by the diamond in Fig. 4.4. This turns out to be one of the best reviving points in all of regions (1), (2) and (3), including the $|\mathbb{Z}_2\rangle$ and $|0\rangle$ initial states. As discussed above, the TDVP semiclassical formalism is not well-suited for describing this case as it cannot capture the diverging entanglement entropy of the initial state. This immediately raises the question if the observed QMBS behaviour is a finite size effect and whether one should rather expect a sharp boundary between regions (1) and (2) in Fig. 4.4 in the thermodynamic limit.

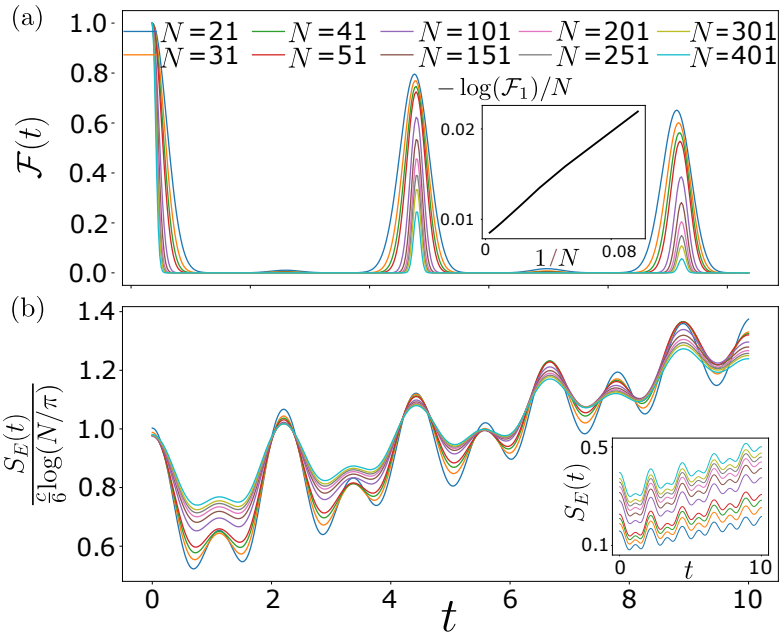

Figure 4.8: Fidelity and entanglement entropy dynamics for the quench from the critical ground state with $\mu_\mathrm{i} = -1.31$ to $\mu_\mathrm{f} = 0.6$. (a) Fidelity revivals persist up to the largest system size $N = 401$. While the fidelity decays with N, the fidelity *density* of the first revival peak, $-\log(\mathcal{F}_1)/N$, plotted against inverse system size, $1/N$, extrapolates to a value close to 0 (inset), indicating non-ergodic behaviour in the thermodynamic limit at a finite time. (b) Dynamics of the half-chain entanglement entropy $S_E(t)$ for the same quench. We scale the entropy by the critical value given by the Cardy-Calabrese formula with central charge $c = 1/2$ [223], which collapses the data to 1 at $t = 0$ (inset shows the unscaled entropy). The growth of entropy is seen to be linear, with pronounced oscillations. Data is obtained by MPS simulations with OBCs, bond dimension $\chi = 300$, and time step $\delta t = 0.025$.

To probe the robustness of QMBS revivals in the thermodynamic limit, we simulated the quench $\mu_\mathrm{i} = -1.31 \to \mu_\mathrm{f} = 0.6$ in large systems up to $N = 401$ using MPS in Fig. 4.8.

The fidelity, plotted in Fig. 4.8(a), demonstrates that revivals exist in all accessible system sizes. The fidelity is not an intensive quantity, therefore it is generically expected to decay in the $N \to \infty$ limit due to the exponential growth of the Hilbert space with system size, as observed in Fig. 4.8(a). Thus, to compare different system sizes, we take the fidelity at the first revival peak $\mathcal{F}_1$ and plot its density, $-\log(\mathcal{F}_1)/N$ against $1/N$, in inset of Fig. 4.8(a). This serves as an indicator of ergodicity breaking at a finite time that can be properly scaled to the thermodynamic limit as it remains constant with system size. For a random state in the constrained Hilbert space of the PXP model, whose dimension grows asymptotically as $\sim \phi^N$, where $\phi = (1+\sqrt{5})/2$ is the Golden Ratio [184], the fidelity density at late times asymptotically approaches the value $\log\phi \approx 0.48$, with $O(1/N^2)$ corrections. Contrary to this expectation, the fidelity density in Fig. 4.8(a) continues to decrease as $N \to \infty$ and extrapolates to a value smaller than 0.01, signaling non-ergodicity in the thermodynamic limit at a finite time scale $t \sim 5/\Omega$, which is well beyond the initial relaxation.

In Fig. 4.8(b) we observe a slow growth of entanglement entropy following the same quench. In contrast to previous QMBS cases in the literature, where the system was initialised in a product state with zero entropy, here we start from a critical ground state whose entropy is expected to diverge logarithmically with system size according to the Cardy-Calabrese formula, $S_{\text{crit}} = (c/6)\log(N/\pi)$ [223]. The universal prefactor is determined by the central charge c of the conformal field theory, which is $c = 1/2$ for our critical point in the Ising universality class. Scaling the data by S_{crit} indeed yields a good collapse at time $t = 0$. At later times, the entropy grows linearly with time. On top of linear growth, we observe prominent oscillations that are typically found in QMBS systems, e.g., the $|\mathbb{Z}_2\rangle$ initial state in the PXP model [18]. The amplitude of these oscillations is roughly independent of system size, as can be seen in the inset of Fig. 4.8(b). At much later times, which are inaccessible to MPS methods, we expect the entropy to saturate to a value proportional to the volume of the subsystem.

Apart from the diverging entropy of the initial state, the overall picture from Fig. 4.8 is broadly similar to previous studies of QMBS dynamics [20]. What remains to be explained is why the critical ground state is poised towards QMBS-like dynamics.

To identify the microscopic origin of this robust ergodicity breaking in the vicinity of $\mu_{\text{f}} = 0.633$, we plot the overlap of the initial critical ground state with the eigenstates of the post-quench Hamiltonian in Fig. 4.9. The overlap exhibits clear towers of eigenstates which are emblematic of QMBS. While these features are present throughout the spectrum, the dominant contributions to the initial state come from low-energy eigenstates. In order to approximate their characteristics, we can treat them as magnons with a given momentum k on top of the ground state. For $\mu_{\text{f}} = 0$, this has been shown to give a good

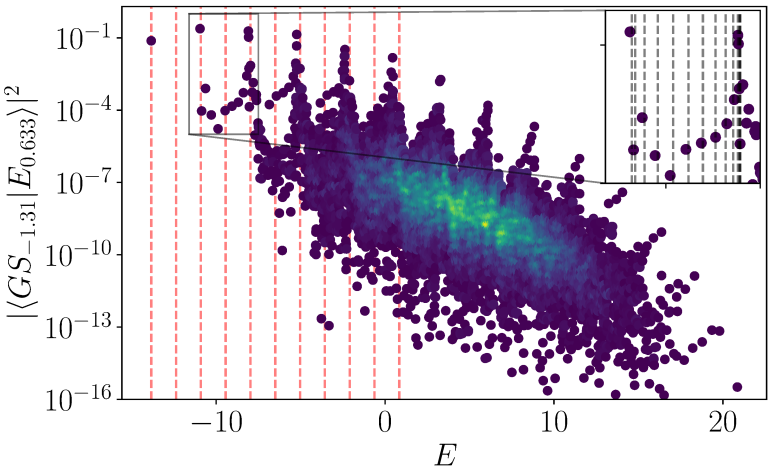

Figure 4.9: Overlap between the ground state at the critical point $\mu_\mathrm{i} = \mu_\mathrm{c} = -1.31$ and the eigenstates of the PXP model with $\mu_\mathrm{f} = 0.633$. The colour indicates the density of datapoints. The red dashed lines indicate multiples of the energy of a $k = \pi$ excitation on top of the ground state. This matches well with the scarred towers in the relevant part of the spectrum. The inset shows the first set of excited states, with the grey dashed lines indicating the expected energy for non-interacting pairs of excitations with momenta k and $-k$. Due to the flatness of the band near $k = \pi$ and $k = 0$, the lines are denser near the scarred states, leading to sharper towers and better revivals (see further analysis of the magnon dispersion in Fig. 4.10 below). Data is obtained by exact diagonalisation for system size $N = 28$ with PBCs.

approximation of scarred states even at relatively high energies when using magnons with momentum $k = \pi$ [224]. Magnon, in this sense, refers to a quasiparticle excitation with a given momentum built on top of the ground state $|GS\rangle$. More formally, an magnon $|k\rangle$ with momenta k is defined as

$$|k\rangle = \mathcal{N}_k Z_k |GS\rangle \,, \tag{4.18}$$

where $\mathcal{N}_k$ is a normalisation factor given by

$$\mathcal{N}_k = \langle GS|Z_{-k}Z_k|GS\rangle^{-1/2} \tag{4.19}$$

and

$$Z_k = \sum_{j=0}^{N-1} e^{ijk} Z_j \tag{4.20}$$

where Z_j is the Pauli-Z operator (for more information, see Ref [224]). Similarly, we find this to be true in our case near $\mu_\mathrm{f} = 0.6$, where much of the low-energy spectrum can be approximately reconstructed from pairs of non-interacting magnons with momenta k and $-k$, see the dashed lines in Fig. 4.9 and inset. Note that the PXP model is gapped

for $\mu_{\rm f} = 0.633$. Hence, the ground state and the first tower in Fig. 4.9 are separated by a finite energy that is independent of N in sufficiently large systems.

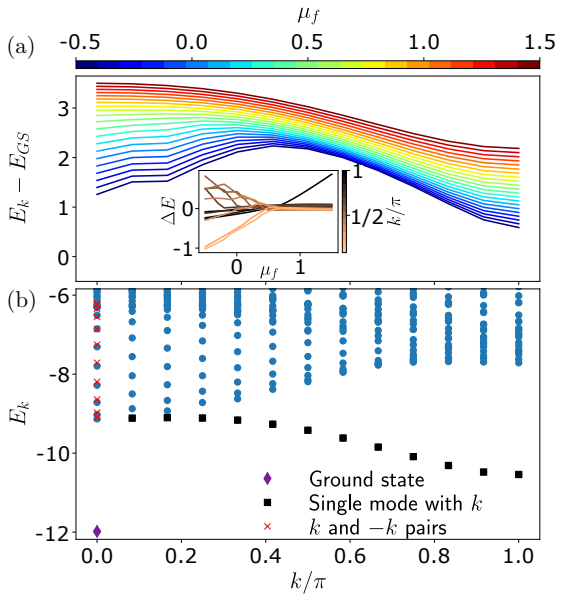

Figure 4.10: (a) Dispersion relation of the low-lying excitations of the PXP model for several values of the chemical potential $\mu_{\rm f}$, shown in different colours. When $\mu_{\rm f} \approx 0.6$, the dispersion becomes visibly flat near both $k = 0$ and $k = \pi$ momenta. Inset shows the difference between the actual energies of the first excited states in the spectrum and their approximation by a pair of two non-interacting excitations. For all momenta k, the best agreement between the approximation and exact energy is attained at $\mu_{\rm f} \approx 0.6$. (b) Low energy spectrum of the PXP model with $\mu_{\rm f} = 0.6$ – the value with the best revivals when quenching from the critical ground state. The ground state and first excited states are indicated, along with energies corresponding to a non-interacting pair of excitations with momenta k and $-k$. In this instance, we see the approximate excitations and exact energy levels lie close to each other. Data is obtained by exact diagonalisation for system size $N = 24$ with PBCs.

A detailed analysis of the magnon dispersion as a function of chemical potential is presented in Fig. 4.10. The dispersion relation for several values of $\mu_{\rm f}$ is shown in Fig. 4.10(a). For $\mu_{\rm f} < 0.6$, the single-magnon band merges with the two-magnon continuum, causing the downward slope near $k = 0$. Near $\mu_{\rm f} = 0.6$, the band becomes remarkably flat for small k, coinciding with the one-magnon and two-magnon bands barely touching. At that point, the energies of the first excited states at $k = 0$ are well approximated by twice the energies of the single-magnon states. This indicates that they correspond to a pair of two non-interacting magnons with momenta k and $-k$. This is illustrated in Fig. 4.10(b) and the inset of panel (a). This simple picture of non-interacting excitations allows us to predict the energies of the low-energy excited states based solely

on the dispersion relation of the single-magnon states. In particular, the flatness of the band near $k = 0$ and $k = \pi$ means that the eigenstates near the scarred ones have approximately the same energy. This implies that towers of states will be sharper, and that the effective energy spacing, which determines the dynamics at intermediate times, is the spacing between the towers. In turn, the fact that magnons are very weakly interacting means that the spacing between these towers will be approximately equal.

In summary, we showed that QMBS in the critical initial state can persist due to (i) the post-quench Hamiltonian $H_{\mathrm{PXP}}(\mu_{\mathrm{f}})$ having a gapped spectrum with a sufficiently flat band of the low-lying magnon excitations; (ii) the magnons are weakly interacting and their multiplets give rise to regularly spaced QMBS-like towers in the spectrum. While this scenario is reminiscent of Ref. [225], where quantum revivals in some non-integrable models were related to the low-lying quasiparticle states, in our case the chemical potential needs to be finely tuned to a value $\mu_{\mathrm{f}} \approx 0.6$ to meet the conditions (i)-(ii). Indeed, as seen in Fig. 4.4, varying μ_{f} around this value leads to a sharp decay of QMBS revivals. In contrast to the PXP model with $\mu_{\mathrm{i}} = 0$ and the $|\mathbb{Z}_2\rangle$ initial state, the QMBS eigenstates in the $\mu_{\mathrm{i}} = \mu_{\mathrm{c}}$ case are clearly skewed towards the low-energy part of the spectrum, however this allows the QMBS revivals to persist in large systems, despite the highly entangled initial state.

4.6 Chapter conclusions

In this chapter, we have presented a mechanism of weak ETH violation via quantum many-body scarring. In contrast to Chapter 2 – which focused on a model that maximises thermalisation – here we demonstrated the PXP model's ability to evade thermalisation and ETH expectations for a few select initial states. While the presence of QMBS in the PXP model had been well established, it was previously considered a finely-tuned phenomenon occurring in a small number initial states that are difficult to identify. Throughout this chapter, we showed how the simple addition of an excitation-counting term to the PXP Hamiltonian reveals the ubiquity of scarring, introducing a greater level of control over thermalisation and the capability to evade it.

We mapped out the dynamical phase diagram of the detuned PXP model based on ergodicity breaking in the dynamics following a global quench of the chemical potential. This demonstrated the existence of extended regions which harbour QMBS phenomena, either associated with the previously studied initial conditions, such as $|\mathbb{Z}_2\rangle$ and $|0\rangle$, or with new entangled states such as $|\bar{0}(\mu)\rangle$. The mechanisms giving rise to these QMBS phenomena, in particular the underlying periodic trajectories, were identified within the TDVP framework. Analysing in detail the robustness of QMBS when the system is tuned

to the EPT, we argued that the latter does not provide an obstacle for QMBS. This holds provided that the post-quench Hamiltonian is tuned in such a way that the low-lying quasiparticle excitations are weakly interacting and possess a flat energy-momentum dispersion. This enables different QMBS regions in the dynamical phase diagram to connect smoothly, bridging across the critical point.

In view of experimental realisations, we outline an adiabatic ramping protocol in Appendix C.5 that allows one to map out the same phase diagram in Rydberg atoms and ultracold bosons in tilted optical lattices, both of which have recently implemented the PXP model in the presence of a tunable chemical potential. In experiment, the evolution is naturally restricted to finite times, as assumed above. However, in Ref [220] we also discuss the corresponding phase diagram at late times, $t \to \infty$. In summary, the existence of a continuous family of QMBS states, tunable by the chemical potential, demonstrates the capability in the PXP model to evade thermalisation in ways that were previously thought inpossible.

One motivation for the work presented in this chapter was to address the open problem of identifying all initial conditions associated with QMBS for a given model. For the pure PXP model, it had originally appeared that only the $|\mathbb{Z}_2\rangle$ and $|\mathbb{Z}_3\rangle = |100100...100\rangle$ states are special in this regard [16]. However, more recent explorations of the chemical potential [27] have revealed that the latter can also stabilise QMBS from a different initial state, $|0\rangle$. In this chapter, we have highlighted that these two product states share a semiclassical description and belong to a larger family, including some other weakly-entangled states such as $|\bar{0}(\mu)\rangle$ state. In fact, our results for the initial state at the critical point suggest that QMBS dynamics is not necessarily associated with preparing the system in a product state or even an area-law entangled state, but in principle allows for highly-entangled initial states. In this case, QMBS dynamics is more strongly temperature-dependent. This is evident from the strong overlap of the initial state with the relatively low-lying energy eigenstates of the post-quench Hamiltonian. The key ingredient for making this work was to suppress the interaction between quasiparticles and flatten their energy dispersion.

The existence of a many-body scarring phase diagram directly challenges the notion that scars are "rare" phenomena. The tunability of initial scarring states in PXP through a simple control parameter serves as a practical knob for controlling the effect of thermalisation with potential applications in quantum technologies. For example, the existence of a continuous family of QMBS states would be of interest in quantum-enhanced metrology, for which QMBS states were shown to be advantageous [226–228]. On the other hand, several fundamental questions also remain open. For example, it is unclear how to explain the entirety of the dynamical phase diagram in the framework of a spectrum-

generating su(2) algebra, which had previously provided an elegant description of revivals from the $|\mathbb{Z}_2\rangle$ state in the pure PXP model [23]. Furthermore, when it comes to scarring from the critical ground state, it would be interesting to explore if such mechanisms apply to other models and whether they can be used to realise similar dynamics from highly-entangled initial states.

Chapter 5

In the absence of chaos: avoiding Gaussification in Rydberg atom arrays

5.1 Chapter introduction

Having demonstrated the menagerie of methods one may use to explore quantum thermalisation, from maximising it in Chapter 3 to evading it in Chapter 4, we now consider processes similar to thermalisation. Specifically, do any mechanisms similar to thermalisation exist, wherein initially-encoded information eventually gets scrambled – and if so, can it be also avoided and utilised? One such mechanism is Gaussification – a process wherein initially non-Gaussian quantum states inevitably evolve towards a non-interacting Gaussian state. This process can occur in both interacting as well as non-interacting systems [30].

In this thesis, we quantify a states Gaussianity via the violation of the Wick's decomposition [229]. This will be explained later in the chapter but, in a sense, the Wick's decomposition is the decomposition of n-point correlations in a quantum state into smaller correlations. If a state is interacting (and therefore highly correlated), it will be impossible to break the correlations down and there will therefore be a violation of the Wick's identity. The extend of this violation quantifies how non-Gaussian a state is. Following from this, the process of Gaussification can defined by the emerging ability to decompose correlations via the Wick's decomposition over time.

Recent works [30, 230] have investigated the behaviour where generic closed systems, governed by quadratic Hamiltonians, swiftly relax to Gaussian states, regardless of their initial conditions, thereby undergoing Gaussification. Significant work has gone into

understanding the process of Gaussification, particularly in quadratic non-interacting fermionic systems where it is found to arise due to two properties: clustering of correlations in the initial state and a Hamiltonian that exhibits delocalising transport [30]. Examples of such Hamiltonians include quadratic hopping Hamiltonians with a constant on-site potential as well as the critical Ising model. The emergence of Gaussian correlations has also been demonstrated in recent experiments on coupled one-dimensional superfluids [231]. This process can often prove detrimental due to the need for interacting (non-Gaussian) quantum states in quantum information protocols.

This chapter explores the process of Gaussification in Rydberg atom arrays, wherein certain initial states are expected to evolve into Gaussian states when the Hamiltonian is quenched between different ordered phases. To systematically understand these dynamics, our new findings involves the construct a Gaussification phase diagram and investigate its structure through global quenches between different regions, quantifying Gaussianity using both local Wick decomposition and a variational approach based on reduced density matrices. Our findings reveal that, surprisingly, in certain cases Gaussification can be circumvented.

Specifically, in this work we explore regimes where the ground state of the Rydberg Hamiltonian is either a non-Gaussian $\mathbb{Z}_3$ like state or a Gaussian $\mathbb{Z}_2$ like state. In this instance, it is typically expected that if one takes the $\mathbb{Z}_3$ state and quenches in the regime where $\mathbb{Z}_2$ is the ground state, that Gaussification will take place where the $\mathbb{Z}_3$ state is ultimately scrambled to a Gaussian state. As we will demonstrate, however, one can instead similarly evade Gaussification through experimentally accessible techniques and novel measuring methods.Our analysis not only uncovers the underlying mechanisms that govern the onset or evasion of Gaussification but also confirms the robustness of these behaviours against realistic experimental imperfections. These results demonstrate that, much like thermalisation, Gaussification is not an inevitable outcome but a nuanced process shaped by controllable physical parameters.

5.2 From thermalisation to Gaussification

We start by noting that free field theories describe the dynamics of fields with no interactions. These are known as Gaussian as their path integral description contains some form of Gaussian function [229, 232]. In the presence of interactions, however, the system's ground state often develops strong non-Gaussian correlations. While Gaussian states are highly structured and can be understood using a variety of theoretical techniques, it is the non-Gaussian states (strongly correlated interacting states) that often play a key role as resources for universal quantum computation and enhancing the efficiency of a range of

quantum information protocols. These include quantum teleportation, communication, sensing, metrology and quantum error correction [33–45].

Recent works [30, 230] have investigated the behaviour of quantum states under non-equilibrium dynamics, sparked by the intriguing question: What happens to an interacting state when interactions suddenly vanish, e.g., after a global quench of the system? It has been shown that generic closed systems, governed by quadratic Hamiltonians, swiftly relax to Gaussian states, regardless of their initial condition in contrast to recent results established in fine tuned open quantum system [30,32]. This can be viewed as an example of a "quantum central limit" theorem [233, 234].

To explain the emergence of Gaussianity, several mechanisms have been proposed, such as spatial scrambling and canonical transmutation, the latter suggesting that Gaussian components of the initial system act as a Gaussian bath, therefore suppressing non-Gaussianity [30, 230]. These mechanisms have been used to describe the decay of non-Gaussianity in recent experiments on ^{87}Rb superfluids trapped in a double well potential [179, 231]. While these studies have provided crucial insights into the process of relaxation in quantum many-body systems [4], they are restricted to systems with effectively non-interacting degrees of freedom, which do not exhibit "full" thermalisation but only relax towards a Generalised Gibbs Ensemble [235]. It is thus important to understand the role of Gaussianity in interacting systems, which can exhibit chaotic dynamics and thermalisation. In particular, it is important to understand if and how non-Gaussianity could be protected in such many-body systems when they are taken out of their equilibrium state.

We will show that Rydberg atom arrays [236] provide a versatile experimental platform for realising and manipulating non-Gaussian correlations far from equilibrium. We show that quenching the atoms between different ordered phases allows to explore two very different regimes of correlations. On the one hand, our setup allows to observe how non-Gaussian correlations build up as the system undergoes thermalising dynamics from an initial, nearly free-fermion state. On the other hand, it is possible to "lock" the system in a strongly non-Gaussian state, which evades both Gaussification and thermalisation at late times. This intriguing non-Gaussian regime is found to be remarkably robust, e.g., even to quenching the system across a quantum phase transition. Our proposal can be readily implemented in Rydberg atom experiments [15, 16, 46, 47], which have recently realised the required types of ordered states and protocols for probing correlations in out-of-equilibrium dynamics.

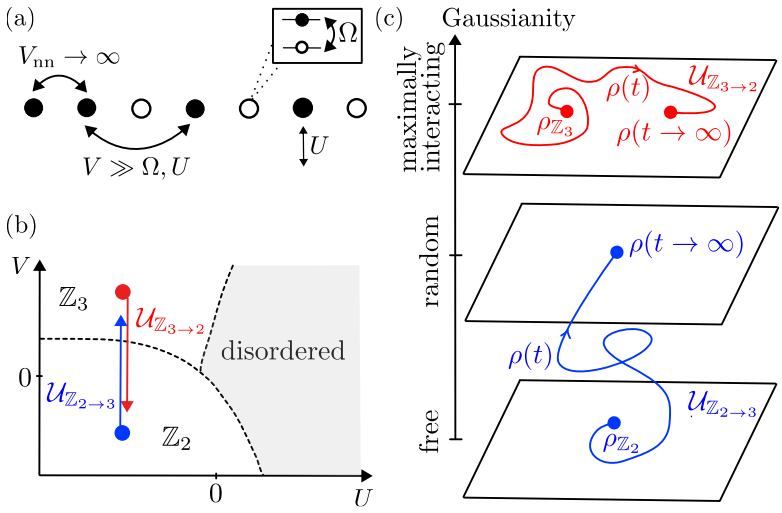

Figure 5.1: (a) Schematic description of a 1D UV model, Eq. (5.1). (b) Sketch of the phase diagram in the U-V plane. We focus on the $\mathbb{Z}_2$ and $\mathbb{Z}_3$ ordered phases and quenches between them: blue arrow $\mathcal{U}_{\mathbb{Z}_{2\to 3}}$ indicates a quench from $\mathbb{Z}_2$ ordered phase into the $\mathbb{Z}_3$ phase, while the red arrow represents the reverse quench $\mathcal{U}_{\mathbb{Z}_{3\to 2}}$. (c) The two types of quenches lead to strikingly different dynamical behaviours. During the $\mathcal{U}_{\mathbb{Z}_{2\to 3}}$ quench, the system is initially free and Gaussianity grows until it reaches typical values in a random state. By contrast, during the $\mathcal{U}_{\mathbb{Z}_{3\to 2}}$ quench, the state remains strongly interacting and it is pinned to a highly non-Gaussian manifold. We will quantify this picture in Secs. 5.4.1 and 5.4.2 using precise Gaussianity measures.

5.3 The UV model of Rydberg atoms

We consider again a one-dimensional (1D) periodic chain containing N Rydberg atoms where each atom is modelled as a two-level system, where $|0\rangle$ represents an atom in the ground state and $|1\rangle$ is an excited Rydberg state. The atomic array is governed by the Hamiltonian [183]:

$$\mathcal{H} = \sum_{i=1}^{N} -\Omega P_{i-1}\sigma_i^x P_{i+1} + U n_i + V n_i n_{i+2}, \tag{5.1}$$

where the flipping between the ground and excited states is described by the Rabi frequency Ω, U is the chemical potential (detuning), and V is the next-nearest neighbour interaction between atoms excited to Rydberg states, see Fig. 5.1(a). Unless specified otherwise, due to the periodic boundary conditions, we will restrict our calculations to the zero momentum sector in the largest sector of the Hilbert space containing no neighbouring excitations.

The model in Eq. (5.1) is again applicable to the strong Rydberg blockade regime,

where the nearest-neighbour van der Waals interaction is much larger than all other energy scales [236]. The strong Rydberg blockade imposes the kinetic constraint $n_i n_{i+1} = 0$, which forbids Rydberg excitations on adjacent sites. This constraint is enforced in the Hamiltonian by dressing the σ_i^x with projectors on the neighbouring atoms. This prevents the Rabi flip term from generating nearest-neighbour excitations, such that states $\cdots 11 \cdots$ with neighbouring atoms simultaneously excited are projected out of the Hilbert space. As we can see, this is just a simple extension of the previously studied PXP model in Chapter 4 with next-nearest neighbour interaction and we have also recast μ as U to align with the literature.

The interplay of U and V terms gives rise to a rich phase diagram sketched in Fig. 5.1(b). The phase diagram was mapped out with high precision in the numerical simulations in Refs. [237–239] and explored in experiments [16,46]. Large negative values of the chemical potential U favour excitations on every other site (due to the Rydberg blockade, this is largest density of excitations allowed). On the other hand, positive V value assigns a repulsive potential on the next-nearest neighbours and it favours excitations on every third site. Conversely, large negative V favours excitations on every other site. Thus, the model in Eq. (5.1) hosts two ordered phases represented by states

$$|\mathbb{Z}_2\rangle = \frac{1}{\sqrt{2}}(|10101\ldots\rangle + |01010\ldots\rangle), \tag{5.2}$$

$$|\mathbb{Z}_3\rangle = \frac{1}{\sqrt{3}}(|100100\ldots\rangle + |010010\ldots\rangle + |001001\ldots\rangle), \tag{5.3}$$

in which Rydberg excitations occupy every second or third site, respectively. Both of these phases are destroyed by sufficiently large positive U, which drives the system into a disordered ($|0\rangle$) phase, see Fig. 5.1(b) [183, 240, 241].

For the subsequent calculations, unless specified otherwise, we set $\Omega = 1$ and concentrate on the Gaussianity and entanglement properties of the initial state as we quench the Hamiltonian between $\mathbb{Z}_2$, $\mathbb{Z}_3$ ordered phases, Fig. 5.1(b). We will show that the choice of the initial state and realisation of the quench can have dramatically different influence on the Gaussianity, as illustrated in Fig. 5.1(c). For the quench initialised in the $\mathbb{Z}_2$ phase, indicated by $\mathcal{U}_{\mathbb{Z}_{2\to 3}}$ in Fig. 5.1(b), the Gaussianity, as precisely defined in Sec. 5.4.1 below, is initially low because the pre-quench state can be approximately expressed as a free-fermion state. After the quench, the state becomes progressively more correlated, with its Gaussianity approaching that of a random vector in the same Hilbert space at late times. This behaviour is consistent with thermalisation dynamics. In contrast, the ground state in the $\mathbb{Z}_3$ phase cannot be expressed as a free-fermion state and hence it has high non-Gaussianity. Moreover, following the quench, the state remains strongly interacting, which occurs due to a lack of thermalisation in this case. It is important to note

that in both cases, the quench Hamiltonian, regardless of the nature of the ground state, is an interacting, non-integrable Hamiltonian – further contrasting the two regimes. In the following sections, we introduce several metrics of non-Gaussianity and quantitatively support the phase diagram and dynamical behaviour sketched in Fig. 5.1.

5.4 Detecting and evading Gaussification

5.4.1 Gaussianity Phase diagram

Let us begin with how one measures Gaussianity. A conventional approach for quantifying the Gaussianity of quantum states relies on Wick's theorem [229]. This theorem allows to reduce the evaluation of n-point correlation functions in terms of "contractions" (i.e., vacuum expectation values) of pairs of creation and annihilation operators. For any free-fermion system, the Wick's identity for four-point correlators takes the form

$$\langle \hat{A}\hat{B}\hat{C}\hat{D}\rangle = \langle \hat{A}\hat{B}\rangle\langle \hat{C}\hat{D}\rangle - \langle \hat{A}\hat{C}\rangle\langle \hat{B}\hat{D}\rangle + \langle \hat{A}\hat{D}\rangle\langle \hat{B}\hat{C}\rangle, \tag{5.4}$$

where we take the expectation value with respect to the ground state ("vacuum") – though this can be similarly used with any state. One possible definition of Gaussianity $\mathcal{W}$ is the extent to which Eq. (5.4) is violated, i.e., the absolute value of the difference between its left-hand and right-hand side. For Gaussian states, we have $\mathcal{W} = 0$. The operators $\hat{A}, \ldots, \hat{D}$ are understood to be single-site fermionic creation and annihilation operators $\hat{f}_i, \hat{f}_j^\dagger$, which obey the anti-commutation relation $\{\hat{f}_i, \hat{f}_j^\dagger\} = \delta_{ij}$. As our model in Eq. (5.1) is expressed in terms of spin variables, it will be convenient to work with spin operators rather than fermionic ones, which can be accomplished by applying the Jordan-Wigner transformation (using the same procedure as illustrated in Appendix A.1).

In order to distinguish the Gaussianity between $\mathbb{Z}_2$ and $\mathbb{Z}_3$ ordered phases, we choose $\hat{A} = \hat{f}_1^\dagger$, $\hat{B} = \hat{f}_1$, $\hat{C} = \hat{f}_2^\dagger$, $\hat{D} = \hat{f}_3$, resulting in the following measure of the Wick's decomposition violation:

$$\begin{aligned}\mathcal{W}(\rho) = \big|&\langle n_1\sigma_2^+\sigma_3^-\rangle - \langle n_1\rangle\langle\sigma_2^+\sigma_3^-\rangle \\ &- \langle\sigma_1^+\sigma_2^+\rangle\langle\sigma_1^-\sigma_2^z\sigma_3^-\rangle + \langle\sigma_1^-\sigma_2^+\rangle\langle\sigma_1^+\sigma_2^z\sigma_3^-\rangle\big|,\end{aligned} \tag{5.5}$$

where $\sigma_j^\pm \equiv (\sigma_j^x \mp i\sigma_j^y)/2$ are the standard spin raising and lowering operators at site j, and ρ denotes the ground state of the system (which could be either a pure state or a density matrix). This particular choice of operators $\hat{A}, \ldots, \hat{D}$, justified in Appendix D.1, will reveal the difference between the $\mathbb{Z}_2$ phase, where $\mathcal{W} \approx 0$ across the entire phase, and the $\mathbb{Z}_3$ phase where the deviation from Wick's decomposition is of order unity, $\mathcal{W} \sim O(1)$.

The ambiguity in the choice of operators in the Wick decomposition can be elimin-

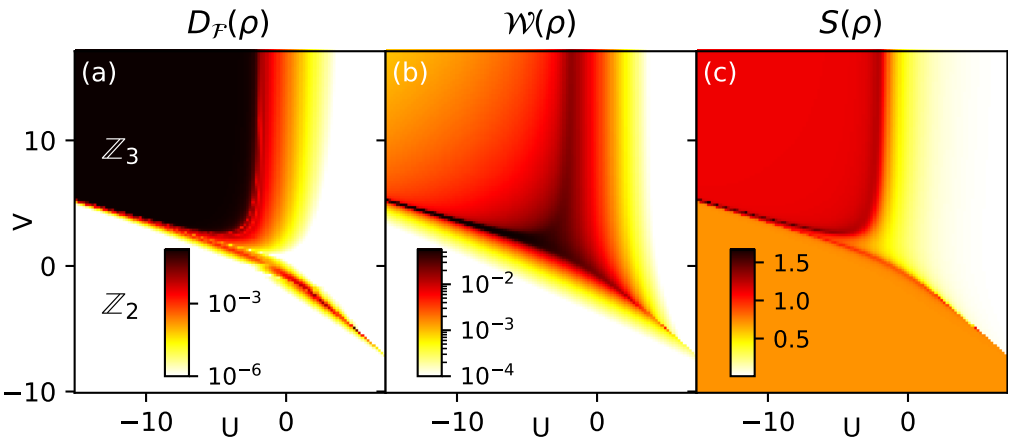

Figure 5.2: Gaussianity phase diagram for the ground state of the model in Eq. (5.1) as a function of U and V. The colour scale represents the value of interaction distance $D_{\mathcal{F}}$ in (a), the Wick's decomposition violation $\mathcal{W}$ in (b), and the entanglement entropy S in (c). All data was obtained by exact diagonalisation for N=18 atoms on a ring with periodic boundary conditions.

ated by employing variational optimisation techniques to measure the minimum distance between the reduced density matrix of a given state and the set of all density matrices associated with free-fermion models [242–245]. This quantity, dubbed the "interaction distance" $D_{\mathcal{F}}$ [242], allows for a more general characterisation of the state's Gaussianity. It does so by quantifying its deviation from the *closest* free-fermion model defined in an *arbitrary* basis (for more detailed information, see Appendix D.2 and Refs. [242,246,247]). Interaction distance is a property of the reduced density matrix ρ describing the subsystem A of a bipartite system $A \cup B$. For the total system in a pure state $|\psi\rangle$, the density matrix $\rho = \mathrm{Tr}_B\, |\psi\rangle\langle\psi|$ is obtained by tracing out the subsystem B. The eigenvalues ρ_k of ρ define the so-called "entanglement spectrum", $\mathcal{E}_k = -\ln \rho_k$ [248]. Using the entanglement spectrum, the interaction distance is defined as

$$D_{\mathcal{F}}(\rho) = \min_{\{\epsilon\}} \frac{1}{2} \sum_k \left| e^{-\mathcal{E}_k} - e^{-\mathcal{E}_k^f(\epsilon)} \right|, \tag{5.6}$$

where $\mathcal{E}_k^f(\epsilon) = \sum_l n_l^{(k)} \epsilon_l$ is the entanglement spectrum of a free-fermion system, given in terms of single-fermion modes ϵ_l and their occupations $n_l^{(k)} \in \{0, 1\}$ [249]. The sum runs over the many-body entanglement spectrum. The minimisation is over the single-particle energies $\{\epsilon\}$ by scanning over all n_l and ϵ_l, whose number typically scales linearly with the number of atoms N.

It is worth noting that the entanglement spectrum is naturally dependent on the choice of bipartition. Unless otherwise specified, we consider a bipartition of the system

into two equal parts. Our results, however, are not sensitive to the particular choice of partition, as long as both subsystems are of comparable sizes. If one subsystem is much smaller than the other, the number of Schmidt coefficients will be significantly reduced and we expect non-universal behaviour of $D_{\mathcal{F}}$. Interestingly, the interaction distance can also be probed with respect to the eigenspectrum of the system – thus probing the thermal properties of a given Hamiltonian. This analysis can be done and reveals that in both ordered regimes, the Hamiltonian is interacting. Generally, however, this is more cumbersome to perform with increasing system size due to the exponential scaling of the spectrum. Furthermore, it does not reveal the distinct differences in the ground state between the two regimes.

Intuitively, $D_{\mathcal{F}}$ represents the minimum distance between the reduced density matrix of a given quantum state ρ and the density matrix of the closest free-fermion model defined on the subsystem A (see Appendix D.2 for details). Crucially, the free-fermion model is defined up to an arbitrary unitary transformation on A, which makes $D_{\mathcal{F}}$ basis independent. This allows to quantify the Gaussianity of a quantum state without the need to search for suitable operators in $\mathcal{W}$ as done in Eq. (5.5). However, $\mathcal{W}$ has the advantage over $D_{\mathcal{F}}$ in that it is expressed in terms of local correlations that are amenable to experimental measurements. Thus, Eq. (5.5) provides a more practical way of detecting non-Gaussianity in the lab.

The Gaussianity phase diagram for the ground state of the Hamiltonian in Eq. (5.1) is presented in Fig. 5.2 for a range of U and V values. The phase diagram was obtained using both the interaction distance $D_{\mathcal{F}}$ and the Wick's theorem violation $\mathcal{W}$, shown in panels (a)-(b). In panel (c) we also show the von Neumann entanglement entropy as defined in Eq. (2.6). All the quantities were computed for the reduced density matrix corresponding to the subsystem A being one half of the chain. Fig. 5.2 reveals excellent qualitative agreement between all three metrics, in particular between interaction distance and Wick's decomposition. The phase boundaries are in good agreement with Refs. [237, 239], suggesting weak finite-size effects. For large and negative chemical potential U, there are two competing ordered phases, $\mathbb{Z}_2$ and $\mathbb{Z}_3$. In particular, for large and positive values of V, the ground state is the $\mathbb{Z}_3$ ordered state. The quantum phase transition from $\mathbb{Z}_3$ to $\mathbb{Z}_2$ ordered state occurs at around $|V| \sim -U/3$. In between these two ordered phases, we expect a narrow intermediate commensurate phase [46, 183, 237]. This phase is difficult to resolve in small systems used in Fig. 5.2, but it will be irrelevant for our discussion.

Figures 5.2(a)-(b) reveal a stark contrast between the two ordered phases in terms of the Gaussian nature of their ground-state correlations. While the $\mathbb{Z}_2$ ground state is approximately a non-interacting Gaussian state with both $D_{\mathcal{F}}$ and $\mathcal{W}$ close to zero,

the $\mathbb{Z}_3$ ground state is nearly maximally interacting, non-Gaussian state. The notion of "maximally interacting" can be made precise by noting that $D_{\mathcal{F}}$, as a trace distance between density matrices, has an upper bound, which has been conjectured to be $D_{\mathcal{F}}^{\max} = 3 - 2\sqrt{2}$ [247]. In the $\mathbb{Z}_3$ phase in Fig. 5.2, $D_{\mathcal{F}}$ attains values very close to this upper bound. This strongly suggests that it is not possible to express the $\mathbb{Z}_3$ ground state as a Gaussian state of free-fermionic modes. Finally, we note that the entanglement entropy in Fig. 5.2(c) also captures some features of the phase diagram, but it does not sharply distinguish between the $\mathbb{Z}_2$ and $\mathbb{Z}_3$ phases. Thus, the interaction distance and local Wick decomposition are essential to gain a complete understanding of non-Gaussianity, both in equilibrium as well as out-of-equilibrium, as we show next.

5.4.2 Persistent non-Gaussian correlations under quench

Previously, we have seen that the two competing ordered phases, $\mathbb{Z}_2$ and $\mathbb{Z}_3$, are the extreme points on the Gaussianity spectrum: while the $\mathbb{Z}_2$ ground state represents a nearly-free fermion state, the $\mathbb{Z}_3$ state is maximally interacting. It is natural to inquire about the temporal evolution of Gaussianity following a sudden quench between these phases. According to the standard scenario of thermalisation in a closed system [250], under quench dynamics, particularly across a quantum phase transition, the system should lose memory of its initial state and equilibrate towards a maximally entangled state. To test this expectation, we study the spreading of entanglement and non-Gaussian correlations when the system is prepared in the ground state of the Hamiltonian (5.1) for some value $V \equiv V_{\mathrm{i}}$. We then quench the Hamiltonian to some different value of $V \equiv V_{\mathrm{f}} \neq V_{\mathrm{i}}$. By varying V_{i} and V_{f} we can access different ordered states and post-quench Hamiltonians. For simplicity, we keep U the same in the initial and post-quench Hamiltonian and postpone the discussion of its role to Sec. 5.5.

Figure 5.3(a) contrasts the growth of entanglement entropy for the $\mathcal{U}_{\mathbb{Z}_{2\to 3}}$ quench vs. $\mathcal{U}_{\mathbb{Z}_{3\to 2}}$ quench. In the first case, the system exhibits thermalisation, as confirmed by the fast growth of entropy towards its saturation value when it reaches the thermal state. A key indication of thermalisation is the volume-law scaling behaviour of the saturation value of entanglement entropy, $S_\infty \propto N$, consistent with Fig. 5.3(a). In contrast, quenches from the $\mathbb{Z}_3$ state lead to non-thermalising dynamics, as seen in the strongly suppressed growth of entropy in Fig. 5.3(a).

In Fig. 5.3(b) we illustrate how Gaussianity changes in time when we prepare the system in an approximately Gaussian $\mathbb{Z}_2$ state at $t = 0$. In particular, when the post-quench Hamiltonian is in the $\mathbb{Z}_3$ phase (e.g., $V_{\mathrm{f}} = 8$), the deviation from Gaussianity sharply increases from zero and quickly reaches the saturation value of $D_{\mathcal{F}}^{\infty} \approx 0.03$. This value coincides with the interaction distance of a random vector [247]. This is

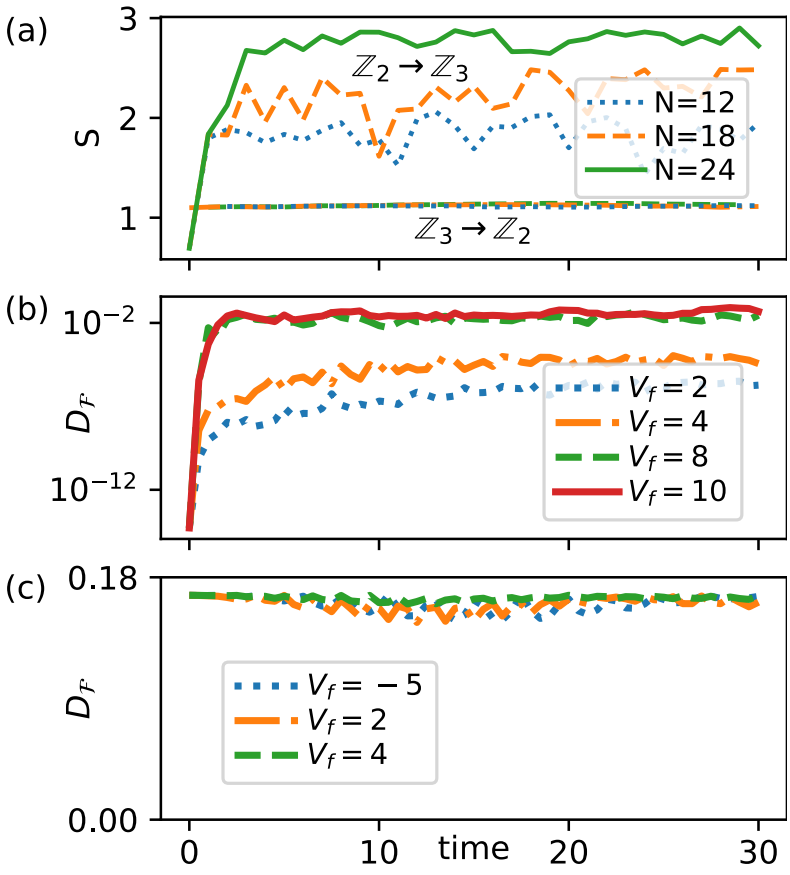

Figure 5.3: Temporal behaviour of entanglement and Gaussianity for quenches $\mathcal{U}_{\mathbb{Z}_{2\to3}}$ and $\mathcal{U}_{\mathbb{Z}_{3\to2}}$, previously indicated in Fig. 5.1(b). The chemical potential is held fixed at U=−15. (a) Growth of entanglement entropy for different system sizes. The top three lines represent $\mathcal{U}_{\mathbb{Z}_{2\to3}}$ (specifically, V_{i}=−5 → V_{f}=8), while the bottom three (overlapping) lines are for the reverse $\mathcal{U}_{\mathbb{Z}_{3\to2}}$ quench. For the $\mathcal{U}_{\mathbb{Z}_{2\to3}}$ quench, the saturation entropy obeys the volume law scaling with system size, indicating thermalisation. By contrast, $\mathcal{U}_{\mathbb{Z}_{3\to2}}$ quench leads to strongly non-thermalising dynamics, as evidenced by a complete lack of entropy growth. (b)-(c) Temporal behaviour of Gaussianity measured by interaction distance. In (b), we quench from the $\mathbb{Z}_2$ ground state (V_{i}=−5) to a range of V_{f} values spanning both $\mathbb{Z}_3$ and $\mathbb{Z}_2$ phases. The top plateau value corresponds to the interaction distance of a random state, $D_{\mathcal{F}}^{\mathrm{random}} \approx 0.03$ [247], consistent with thermalisation observed for $\mathcal{U}_{\mathbb{Z}_{2\to3}}$ in (a). (c) Similar to (b) but for $\mathbb{Z}_3$ initial state (V_{i}=8). The persistent large value of $D_{\mathcal{F}}$ is consistent with an absence of entanglement spreading for $\mathcal{U}_{\mathbb{Z}_{3\to2}}$ quench in (a). Data in panels (b)-(c) is for system size N=18.

consistent with thermalising dynamics at infinite temperature in Fig. 5.3(a), where the state at late times becomes similar to a random vector. Note that this scenario is very different from Ref. [231], where the initial state was chosen to be non-Gaussian, but the Hamiltonian itself is quadratic and induces the development of Gaussian correlations over time. Conversely, for the non-Gaussian $\mathbb{Z}_3$ initial state in Fig. 5.3(c), we see that the previous scenario does not hold. In this case, there is persistent non-Gaussianity after the quench, with no sign of decay of the correlations due to interactions. Consequently, the time-evolved state remains highly interacting over the course of quantum dynamics. We note that these results hold for larger system sizes via finite-size scaling and with open boundary conditions – see Ref [31].

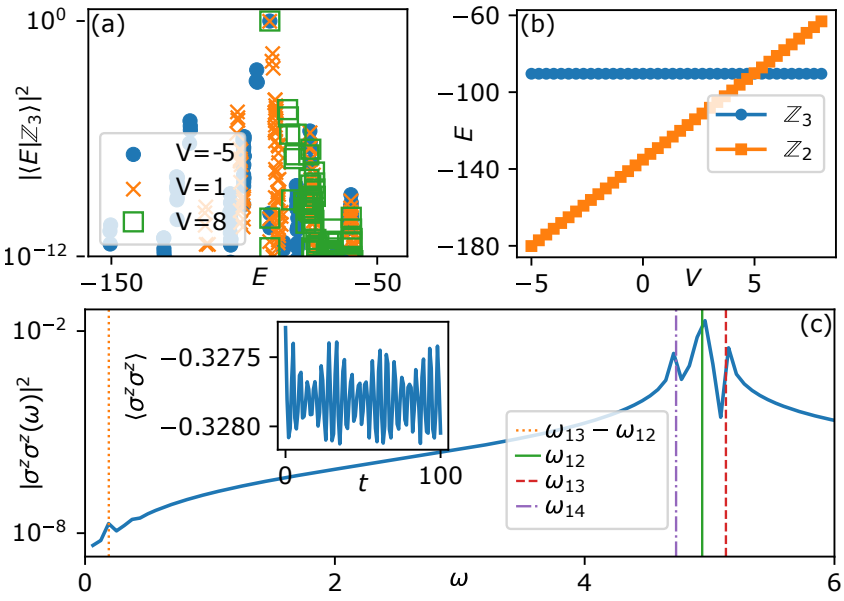

Figure 5.4: The nature of the non-Gaussian quench $\mathcal{U}_{\mathbb{Z}_3\to 2}$. (a) Overlap between the initial $\mathbb{Z}_3$ state (as defined in Eq. (5.2)) and energy eigenstates $|E\rangle$ of the Hamiltonian in Eq. (5.1), plotted as a function of energy. Data is for system size N=18 and $U=-15$, for three V values given in the legend. In all the cases, the $\mathbb{Z}_3$ state has high support (overlap ≈ 1) on a single eigenstate at roughly the same energy. (b) Energy expectation value, $E = \langle\psi|\mathcal{H}|\psi\rangle$, for product states $|\psi\rangle = |\mathbb{Z}_3\rangle$ and $|\psi\rangle = |\mathbb{Z}_2\rangle$, plotted as a function of V with fixed $U=-15$. We see that $|\mathbb{Z}_3\rangle$ remains at constant energy for any V, while $|\mathbb{Z}_2\rangle$ scales linearly. (c) The power spectrum of the correlation function $\langle\sigma^z_i\sigma^z_{i+1}\rangle$ evaluated in the time evolved state (raw data shown in the inset). The vertical lines in the plot represent the energy gaps ω_{ij} between the states with largest overlap in (a). The gaps align precisely with the peaks in the power spectrum.

We now analyse the $\mathcal{U}_{\mathbb{Z}_3\to 2}$ quench in more depth. In terms of spectral properties, we find that there is a single energy eigenstate $|E_1\rangle$ of the Hamiltonian that has very high overlap with the $\mathbb{Z}_3$ state, $|\langle E_1|\mathbb{Z}_3\rangle|^2 \approx 1$, see Fig. 5.4(a). The energy of this ei-

genstate also exactly matches that of the ground state energy of the initial Hamiltonian pre-quench. In fact, the energy of the state is independent of deforming V in the quench Hamiltonian as shown in Fig. 5.4(b). This implies that the $\mathbb{Z}_3$ state is effectively close to being an eigenstate of the Hamiltonian. This behaviour is somewhat reminiscent of quantum many-body scarring [20, 22, 54], with the exception that here the high overlap exists only for a single eigenstate. Furthermore, numerically we find that the special eigenstate $|E_1\rangle$ has lower entanglement entropy than the majority of the spectrum, whereas its interaction distance attains a nearly maximum value. By also plotting the overlap between the $\mathbb{Z}_3$ state and the eigenstates of Hamiltonians with $V = 8$ and $V = 1$, we see the single eigenstate remains dominant at constant energy, regardless of the value of V. The state simply transitions from being an initial ground state to a mid-spectrum state.

Previously, in Fig. 5.3(c), we saw that non-Gaussianity remains robust for the quench $\mathcal{U}_{\mathbb{Z}_{3\to 2}}$. In order to experimentally access this behaviour, one can study temporal behaviour of local correlation functions, as frequently done in modern ultracold atom experiments [251]. For example, the correlation function $\langle \sigma_i^z \sigma_{i+1}^z \rangle$, computed in Fig 5.4(c), reveals persistent oscillations. The characteristic frequencies of these oscillations correspond to the energy differences of the eigenstates with dominant overlap with the initial state of the system. This can be characterised more precisely by the power spectrum [252, 253], computed in Fig. 5.4(c). The dominant frequencies are given by $\omega_{1j} = |E_1 - E_j|$ (and their differences), where $|E_j\rangle$, $j = 2, 3, \ldots$, denote eigenstates with subleading overlaps with the $\mathbb{Z}_3$ state. Similar oscillations and frequencies can be observed in the quantity $\mathcal{W}$ defined in Eq. (5.5), other two-point local correlations, and even in the entanglement entropy.

A simple heuristic argument that gives an approximate value of the oscillation frequency in the limit $U, V \gg \Omega$ can be stated as follows. For the Hamiltonian with $U{=}{-}15$ and $V{=}{-}5$, the ground state is approximately $\mathbb{Z}_2$ product state with energy $E_{\mathrm{GS}}^{\mathbb{Z}_2} \approx (U+V)N/2$. The energy of the $\mathbb{Z}_3$ state is approximately $E^{\mathbb{Z}_3} \approx UN/3$. For general values of U and V there are no other states with the same energy as $\mathbb{Z}_3$. For special ratios of U/V, a resonance may occur and other states could have the same energy as $\mathbb{Z}_3$; we can prevent this by assuming U and V to be irrational numbers. The oscillations seen in Fig. 5.4(c) are between $|\mathbb{Z}_3\rangle$ and states where one of the excitations is moved by a single unit, i.e., the states $|101000100100\ldots\rangle$, $|100101000100\ldots\rangle$ etc., which all have a single 101 pattern. The energy of these states is $UN/3 + V$, so they are lower in energy by approximately $-|V|$ compared to $\mathbb{Z}_3$. This predicts that the oscillation frequency is set by V, i.e., the energy difference between $\mathbb{Z}_3$ states and these states containing $|\ldots 101\ldots\rangle$ in the chain. Thus the energy differences between second and first energy levels are determined by $|V|$, i.e., $\omega_{12} = |E_1 - E_2| \approx |V|$, as can be seen in the power

spectrum in Fig. 5.4(c).

5.4.3 Origin of persistent non-Gaussian correlations

The origin of robust non-Gaussianity associated with the $\mathbb{Z}_3$ state can be more readily understood by considering the evolution in eigenspace overlap for different V presented in Fig. 5.4(a). We consider the difference between the initial Hamiltonian, $\mathcal{H}_i$, and post-quench Hamiltonian, $\mathcal{H}_f$. Recalling Fig. 5.1(b), we restricted to the case where the quench only changes the value of V. Therefore $\mathcal{H}_f = \mathcal{H}_i + \Delta V \mathcal{H}^{nn}$ where $\mathcal{H}^{nn} = \sum_i n_i n_{i+2}$. Now consider a quench from the $\mathbb{Z}_3$ state in its respective regime such that $\mathcal{H}_i |\mathbb{Z}_3\rangle = E_0 |\mathbb{Z}_3\rangle$ with ground state energy E_0. Then, quenching yields $\mathcal{H}_f |\mathbb{Z}_3\rangle = \mathcal{H}_i |\mathbb{Z}_3\rangle + \Delta V \mathcal{H}^{nn} |\mathbb{Z}_3\rangle$. Note that in the case of $|\mathbb{Z}_3\rangle$, there is only occupancy of every third site, therefore $\mathcal{H}^{nn} |\mathbb{Z}_3\rangle = 0$, irrespective of ΔV. Thus,

$$\mathcal{H}_f |\mathbb{Z}_3\rangle = \mathcal{H}_i |\mathbb{Z}_3\rangle + \Delta V \mathcal{H}^{nn} |\mathbb{Z}_3\rangle = \mathcal{H}_i |\mathbb{Z}_3\rangle = E_0 |\mathbb{Z}_3\rangle . \tag{5.7}$$

Hence, upon deforming ΔV, $|\mathbb{Z}_3\rangle$ remains an eigenstate of $\mathcal{H}_f$ with the same energy. This may not necessarily still be the ground state and instead may be shifted up in the energy spectrum for sufficiently large ΔV. This means that upon quenching, the initial state remains the same over long periods of time due to its proximity to an eigenstate. As interaction distance is defined only with respect to a given state ρ, it is clear why it does not significantly change over time, despite quenching the system across criticality. This interpretation is supported by the high overlap with a single eigenstate of the quench Hamiltonian in Fig. 5.4(a).

A similar argument can be made for why the quench from the initial $\mathbb{Z}_2$ state with $\mathcal{H}_f$ in the $\mathbb{Z}_3$ phase leads to scrambling and thermalisation dynamics. As $\mathbb{Z}_2$ has an occupancy on every 2 lattice sites, it "feels" the deformation of ΔV: $\mathcal{H}^{nn} |\mathbb{Z}_2\rangle = \frac{N}{2} |\mathbb{Z}_2\rangle$. Considering the form of $\mathcal{H}_i$ such that the initial state is $|\mathbb{Z}_2\rangle$, the terms that result in this being approximately the ground state are $\sum_{i=1}^{N} -|U| n_i - |V| n_i n_{i+2}$ with $U, V \gg \Omega$. By then suitably tuning a positive ΔV, quenching with $\mathcal{H}_f$ in the $\mathbb{Z}_3$ regime means that $|\mathbb{Z}_2\rangle$ is no longer an eigenstate due to the competing factors of U, V and ΔV. More concretely, the final Hamiltonian when acting on $|\mathbb{Z}_2\rangle$ has a term proportional to $-((|U|+|V|)+\Delta V$. These competing negative and positive terms mean that, overall, $-((|U|+|V|)+\Delta V$ may not be much greater than Ω and thus $|\mathbb{Z}_2\rangle$ may no longer be approximately an eigenstate like before. This results in the possible scrambling of the initial state thus becoming a non-Gaussian state over time.

The further substantiate the previous argument, the underlying mechanism for persistent non-Gaussian correlations can be inferred by considering an effective quench

Hamiltonian with five-body interactions. As we are interested in the quench dynamics going from $\mathbb{Z}_3$ into the $\mathbb{Z}_2$ ordered phase, we define the effective Hamiltonian in a regime where U is negative and large, favouring particle creation on all sites. Similarly, we require V to be large and negative as well. Under these conditions, the quench Hamiltonian is given by

$$\mathcal{H}_q = -\left[\sum_{i=1}^{N} \mathcal{P}_{i-1}\sigma_i^x\mathcal{P}_{i+1} + |U|n_i + |V|n_i n_{i+2}\right] \tag{5.8}$$

with $|U|\gg 1$, $|V|\gg 1$ and we still have $n_i n_{i+1}=0$. Following a similar procedure as in Ref. [254], we move the quench Hamiltonian into an interaction picture with respect to the next-nearest neighbour term by applying the transformation $W^\dagger \mathcal{H}_q W$, where $W = \exp[-it|V|\sum_i n_i n_{i+2}]$. Ignoring the rapidly oscillating phases for $|V| \gg 1$, we reach an effective Hamiltonian

$$\mathcal{H}_q^{\text{eff}} = -\left[\sum_{i=1}^{N} \mathcal{P}_{i-2}\mathcal{P}_{i-1}\sigma_i^x\mathcal{P}_{i+1}\mathcal{P}_{i+2} + |U|n_i\right]. \tag{5.9}$$

In the largest fully connected sector, the presence of Rydberg excitations on the nearest and next-nearest neighbouring sites is prohibited. The effective Hamiltonian corresponds to the PPXPP model with a chemical potential. The $\mathbb{Z}_2$ state still exists as the overall ground state but instead within a small disconnected sector due to the new blockade condition. Meanwhile, due to a large negative U in the effective Hamiltonian, the ground state of the largest sector where the blockade remains respected is $\mathbb{Z}_3$. Thus, the quench Hamiltonian does not induce delocalising dynamics when the system is initialised in the $\mathbb{Z}_3$ state and such states are protected against both Gaussification and thermalisation. We can therefore conclude that the persistent non-Gaussianity of the $\mathbb{Z}_3$ initial state equivalently arises from the effective blockade mechanism up to the next-nearest neighbour excitations in the interaction picture. Agreement in dynamics was also tested and found numerically between the exact Hamiltonian and effective Hamiltonian. This further supports the notion that the initial state remains approximately an eigenstate of the quench Hamiltonian.

5.5 Experimental realisability in Rydberg atom arrays

With the possible quantum information applications, it is important to test the robustness of the non-Gaussification against external perturbations. This is particularly important because our results rely on the quantum superpositions of states with degenerate energies in the $\mathbb{Z}_3$ and $\mathbb{Z}_2$ phases. External perturbations may result in the

superposition collapsing into an energetically favourable product state, thus removing any non-Gaussian correlations. Here we focus on three types of effects that are relevant for experimental implementations: (i) the stability against a single site magnetic field or impurity εn_i with magnitude ε; (ii) the effect of changing the chemical potential U during the quench; (iii) the effect of long-range van der Waals interactions that are present in real systems but were neglected in Eq. (5.1).

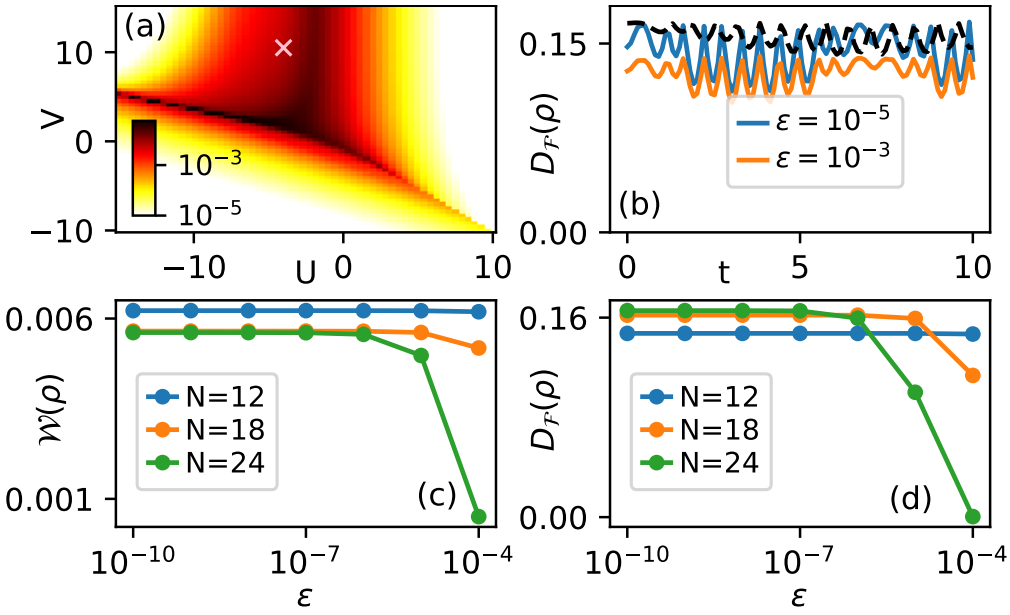

Figure 5.5: Resilience of non-Gaussianity against a local impurity, εn_4, added to Eq. (5.1). (a) The phase diagram obtained using local Wick's decomposition, $\mathcal{W}(\rho)$, with impurity strength $\varepsilon = 10^{-4}$ at system size $N = 12$. The cross marks the point (U, V)=$(-4, 10.5)$ studied in (b)-(d). (b) The time evolution of the interaction distance $D_{\mathcal{F}}$, when quenching the initial ground state at (U, V)=$(-4, 10.5)$ in the $\mathbb{Z}_3$ phase with the Hamiltonian parameters (U, V)=$(-4, -6)$ in the $\mathbb{Z}_2$ phase. Both the initial and quench Hamiltonian contain impurity ε. Data is for system size $N = 12$ with the impurity potentials shown in the legend. Black dashed line is with no error ($\varepsilon = 0$) but instead taking the initial ground state at (U, V)=$(-15, 8)$ and quenching at (U', V')=$(-10, -5)$, which demonstrates persistent non-Gaussianity even with a change in U. (c)-(d) Wick's decomposition and interaction distance, respectively, of the ground state at (U, V)=$(-4, 10.5)$, as a function of impurity strength for several system sizes. Results were computed using exact diagonalisation without resolving translation symmetry.

Fig. 5.5 shows the results when adding the impurity term εn_i to the Hamiltonian in Eq. (5.1) on site $i = 4$. We choose this site along the chain as it is found to have the most substantial effect on the results providing a qualitative lower-bound in robustness. Despite the presence of an impurity, we see that qualitative features of the phase diagram remain preserved with an impurity strength ε=10^{-4}, see Fig. 5.5(a). This is a magnitude

of error much larger than the detuning resolution of current quantum technology [255]. Furthermore, perturbations are generally characterised by their proportionality to the ground state gap. We find this order of magnitude to be comparable to the energy gap of the system (which decreases with N). This demonstrates that the non-Gaussian characteristics are protected nearly up to the same order as the energy gap in the system. It is natural that any larger magnitude of error would disrupt this as one would no longer be probing ground-state physics. Taking a single point in this diagram, marked by the cross, we find the ground state still possesses high overlap with the superposition state $\mathbb{Z}_3$. Consequently, the non-Gaussian correlations persist when quenching in the $\mathbb{Z}_2$ phase (with error still present in the quench Hamiltonian), as seen in Fig. 5.5(b). For this point, the non-Gaussianity remains robust for impurity strengths up to $\varepsilon{\sim}10^{-3}$. Furthermore, in Figs. 5.5(c)-(d) we test the robustness of $D_{\mathcal{F}}$ and $\mathcal{W}$ for this point with varying impurity strength and system size. The non-Gaussianity is seen to be more pronounced in smaller system sizes.

While our presented analysis assumed that only V is changed during the quench, we have numerically verified that the non-Gaussian correlations also remain robust upon simultaneous changes in U. This can be understood via the following argument. Consider modulating both V and U, then $\mathcal{H}_f \left|\mathbb{Z}_3\right\rangle = \mathcal{H}_i \left|\mathbb{Z}_3\right\rangle + \Delta U \mathcal{H}^n \left|\mathbb{Z}_3\right\rangle$ where $\mathcal{H}^n = \sum_i n_i$. Unlike $\mathcal{H}^{nn}$, $\mathcal{H}^n \left|\mathbb{Z}_3\right\rangle \neq 0$. This is instead equivalent to quenching horizontally in the phase diagram in Fig. 5.2; therefore, if ΔU is such that one remains in the regime where $\left|\mathbb{Z}_3\right\rangle$ is approximately the ground state, the state remains an eigenstate and the non-Gaussianity remains robust. This is illustrated by the black dashed line in Fig. 5.5 where in changing V during the quench, we also take $\Delta U = 5$. On the other hand, if ΔU is large enough to transition from the $\mathbb{Z}_3$ regime, thermalisation occurs. This stability against small changes in U makes the non-Gaussianity effect robust against possible experimental imperfections.

Finally, our idealised model in Eq. (5.1) neglects the long-range van der Waals forces that are invariably present in real systems of Rydberg atoms [16, 46, 47]. Thus, it is important to verify our conclusions still hold in the full model describing the Rydberg atom experiments [238]:

$$H = -\frac{\Omega}{2}\sum_i^N \sigma_i^x - U\sum_i^N n_i + V\sum_{i<j}\frac{n_i n_j}{|i-j|^6}. \tag{5.10}$$

Note that, in contrast to Eq. (5.1), here we keep the factor 1/2 in the Rabi term and set V=1 in order to facilitate comparison with the literature. In Fig. 5.6(a), we first recompute the Gaussianity phase diagram of the long-range model with relevant parameters taken from the experimental papers [46,47]. Similar to the truncated model in Eq. (5.1),

the full model also realises both $\mathbb{Z}_3$ and $\mathbb{Z}_2$ phases. The phase diagram in Fig. 5.6(a) is in good agreement with that given in Ref. [238]. We then prepare the state in one phase (indicated by a red cross) and perform a quench into the other phase. As illustrated in Figs. 5.6(b)-(c), the results are consistent with those of the UV model, where the $\mathbb{Z}_3$ state preserves its non-Gaussian correlations. For the $\mathbb{Z}_2$ initial state, the thermalisation time scale is longer than in Fig. 5.3 due to the smallness of the energy gap in the chosen units for the Hamiltonian (5.10).

Taking this a step further, we introduce experimental error into our calculation. Ref. [255] states that there are approximate errors of $\approx 0.1\mu$m in the spatial position of sites along the Rydberg chain. We can factor this into our simulations by recalling to numerical values and modulating $i, j \to i + \delta_i, j + \delta_j$ in Eq. (5.10) (so, numerically, δ is randomly sampled from a normal distribution between ± 0.02). We find that the results still hold well when taking the initial ground state from a disordered Hamiltonian with only a slight decrease in $D_{\mathcal{F}}$ as shown by the orange line in Fig. 5.6(b). More-so, if one assumes the perfect $\mathbb{Z}_3$ state can still be prepared, we find the perfect results still hold irrelevant of the disordered quench Hamiltonian – adding a degree of robustness as it demonstrates the error only factors into the initial state preparation. Overall, the main features of our results are present in the full Rydberg model, suggesting that persistent non-Gaussianity could be observed with the existing experimental technology [46, 47].

5.6 Chapter conclusions

Throughout this chapter, we have examined how quantum states can exhibit a Gaussian or non-Gaussian nature, depending on the degree of interaction between the system's constituent parts. We have investigated the phenomenon of Gaussification, wherein non-Gaussian states undergo transformation into Gaussian states during quench dynamics in quantum many-body systems. This process differs from thermalisation yet it still maintains a degree of information scrambling and loss of memory of the initial state. We have demonstrated that Rydberg atom arrays provide a versatile platform where this behaviour can be probed with available experimental techniques.

More intriguing, perhaps, is the illustration that the Rydberg blockade gives rise to states with remarkably robust non-Gaussian correlations. These correlations are found to persist far from equilibrium, e.g., as the system is quenched across a quantum phase transition. We have elucidated the origin of this behaviour by analysing quenches between $\mathbb{Z}_2$- and $\mathbb{Z}_3$-ordered phases, which exhibit either scrambling dynamics or suppression of thermalisation due to the effective Rydberg blockade mechanism. Moreover, we formulated a criterion based on Wick's decomposition that provides a test for observing

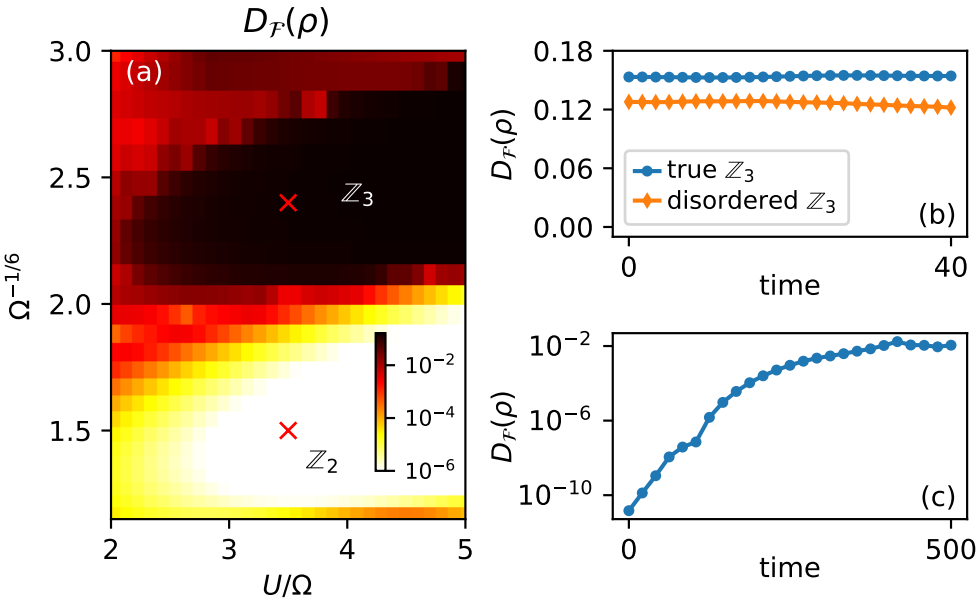

Figure 5.6: (a) Gaussianity phase diagram of the long-range Rydberg model in Eq. (5.10) for system size N=12 and fixed V=1. (b)-(c) Temporal behaviour of $D_{\mathcal{F}}$ when quenching from the point indicated by the red cross in the $\mathbb{Z}_3$ ($\mathbb{Z}_2$) phase to the other phase. The different behaviour of non-Gaussianity for the two types of quenches, seen in Fig. 5.3, is reproduced. Blue lines indicates using the pure Rydberg Hamiltonian Eq. (5.10). Meanwhile the orange line introduces further experimental error by using a Hamiltonian with spatial disorder such that $i, j \to i + \delta_i, j + \delta_j$ where δ is a site dependent and taken randomly in the range $[-0.02, 0.02]$. The results are averaged over 100 realisations. Both the pure and disordered Rydberg Hamiltonian show persistent non-Gaussianity.

(non-)Gaussianity in experiment. This finding was further corroborated via variational optimisation and computing the minimal distance between the reduced density matrix of the ground states belonging to different ordered phases and the set of all free-fermion density matrices defined on the same subsystem. It is important to note that, while both being present, the processes of thermalisation and Gaussification are distinct in this system. The former arises specifically due to the interactions of the system while the latter is expected in any Hamiltonian that exhibits delocalising transport [30].

These results highlight the richness of quantum state complexity in systems evolving under constrained dynamics, providing three contributions to the broader quantum information framework. Firstly, our findings reveal the existence of robust non-Gaussian states in Rydberg systems, which are well-known resources for quantum information processing. Recent studies have shown that non-Gaussian states act as magic states [44], facilitating the construction of a universal gate set. Our findings propose a route towards accessing and utilising these robust states in the commonly explored Rydberg systems,

moving closer to the realisation of universal quantum devices – even in the presence of long-range interactions and local impurity potentials. Secondly, we demonstrate how Rydberg systems allow to naturally generate and manipulate $\mathbb{Z}_3$ and $\mathbb{Z}_2$ states by varying the detuning and interaction range. These two states exhibit stark contrast in terms of their Gaussianity. In particular, we find that the $\mathbb{Z}_3$ state is maximally non-Gaussian while simultaneously robust against thermalisation, allowing it to serve as a qutrit basis for quantum memories [256, 257]. Lastly, our results provide a counterexample to the typical Gaussification scenario of Refs. [4, 233]. This ultimately illustrates the possibility of richer types of dynamical behaviour facilitated by the Rydberg blockade.

Though seemingly distinct from thermalisation, Gaussification is equally pervasive in quantum systems. Developing methods to evade it is crucial for advancing control over broad classes of quantum models. This chapter shows that even in the absence of interactions, where information scrambling persists, these mechanisms can not only be circumvented but also harnessed for practical use in quantum information processing.

Chapter 6

Conclusions and outlook

Understanding and ultimately conquering quantum thermalisation remains a tremendous aspiration in the fields of quantum mechanics and quantum gravity. A valiant effort to achieve this was put forth through the framework of the ETH which associates the thermality of a quantum system with the special properties of its eigenstates. The ETH has enabled great leaps in understanding the properties of quantum many-body systems; however, in spite of its success since the early 1990s, a rigorous analytic formalism is still lacking. As a result, properly understanding quantum thermalisation and how to effectively utilise it remains challenging.

A complementary direction to understanding the ETH is motivated by the question how one can violate it in physically-relevant models. A recent discovery of quantum many-body scarring (QMBS) constitutes a "weak" form of ETH breaking and allows some limited means of evading thermalisation in interacting quantum systems. However, if there is any hope of mastering thermalisation for experimental realisation and access – particularly in quantum technology – there is still significant progress to be made. Such progress is also need for a unified description of quantum gravity, where quantum thermalisation plays a pivotal role in understanding quantum black holes.

This thesis contributes to the efforts mentioned above by showcasing several methods for controlling thermalisation and inducing new types of dynamical behaviours. Below, we first summarise the key findings from each chapter and then discuss possible future extensions on the fronts of experimental realisability, analytical approaches, higher-dimensional extensions, and broader practical applications.

We began in Chapter 3, where we presented an optimally-scrambling quantum spin model. The optimal behaviour was identified through the expectation that a quantum model with a black hole description should exhibit maximal thermalisation – much like the SYK model. Our chiral spin model presents several advantages over the SYK model, for example its natural tunability between a free phase and a maximally scrambling phase

through changing the chiral coupling parameter. This also highlights the experimental realisability of our model: due to locality of the interactions and a lack of disorder, our model is better suited to experimental platforms and a quantum-circuit description. We demonstrated the controllability of thermalisation in the chiral spin model by successfully executing the Hayden-Preskill teleportation protocol, which was able to outperform standard chaotic models by a judicious tuning of the couplings. In other words, our model was able to execute the protocol in a shorter amount of time, making it better suited to realistic quantum hardware which is prone to decoherence over long timescales. These advantages position the chiral spin-chain as a more practical and experimentally viable alternative to the well-known SYK model. Consequently, this also opens new possibilities for studying quantum gravity-inspired phenomena in controlled environments and utilising their properties to achieve quantum advantage.

In Chapter 4, we instead studied how to engineer nearly-perfect state transfer, protected against thermalisation, in Rydberg atom quantum simulators. Through the PXP model – the Rydberg blockade limit of the Rydberg Hamiltonian – we demonstrated the accessibility of QMBS dynamics by constructing the scarring phase diagram. This highlighted the existence of continuous families of experimentally-accessible QMBS states in the PXP model. This was achieved in-part through the time-dependent variational principle (TDVP), an analytical framework that bridges the gap between the single-particle and many-body scarring mechanisms. We emphasise that TDVP can serve as a powerful tool in identifying periodic quantum trajectories in interacting many-body systems, potentially beyond QMBS physics discussed in this thesis [258, 259]. Contrary to the expectation that QMBS dynamics is associated with low-entanglement initial states, our results in Chapter 4 point to the possibility of QMBS dynamics when initialising the system in a ground state at a quantum-critical point. This implies there is an intriguing interplay of QMBS physics with quantum criticality, highlighting the need for further study. The fact that this is achieved by simply tuning the chemical potential demonstrates the flexible control of which states are protected from thermalisation. Moreover, it highlights the need for a generalisation of the ETH to account for such phenomena. Some recent attempts have been made to address this problem by making use of eigenoperators [260] instead of eigenstates.

Finally, the richness of the Rydberg atom platform presents opportunities not only for evading thermalisation but also for exploring similar processes like Gaussification. In Chapter 5, we discussed persistent non-Gaussian correlations when quenching between the $|\mathbb{Z}_3\rangle$ state into the $\mathbb{Z}_2$-ordered phase of Rydberg atoms, in sharp contrast with the observed Gaussification for a reverse quench starting in the $|\mathbb{Z}_2\rangle$ state. We identified the origin of non-Gaussianity with the kinetic constraint due to van der Waals interactions.

To characterise non-Gaussianity in a basis-independent manner, we employed interaction distance measure – a variational estimate of the minimal distance between the reduced density matrix of a given state and the set of all free-fermion density matrices defined within the same Hilbert space. Interaction distance can be viewed as a generalisation of the more traditional and experimentally applicable approach – the Wick decomposition. The key advantage of the interaction distance is the ability to detect correlations without the need of systematically scanning through all different n-point correlation functions. Thus, after using the interaction distance to identify the source of potential non-Gaussian correlations, one can employ Wick's decomposition for further experimental studies. This would allow to detect similar phenomena in other models where Wick's decomposition in the computational basis may have proven insufficient as an initial method. While our study was originally conducted on the UV model, we demonstrated that the same conclusions hold for the full Rydberg model and even in the presence of single qubit imperfections and spatial disorder. These results collectively indicate the experimental robustness of our findings. This is an immediate advantage due to applications of non-Gaussian states as magic states [44]; therefore, any ability to evade their decoherence in an experimental setting is essential.

The work presented in this thesis opens up several directions for further research. First and foremost, it would be beneficial to experimentally verify much of the work throughout this thesis. Fortunately, the existing Rydberg atom platforms are already at a stage where they can probe our results on QMBS and Gaussification. While not discussed here, we have initiated such a study on QuEra's Rydberg atom quantum simulator following up on the work presented in this thesis. On the other hand, an experimental counterpart of the chiral model is still lacking, making it a clear next step for future study. While chiral interactions can be experimentally realised in optical lattice systems [108, 109], we are currently in the process of "reshaping" the chiral spin model into a quantum circuit, similar to [167]. This would enable the realisation of the chiral spin model and maximal scrambling on a quantum processor.

It would also be useful to supplement our findings with more analytic results. Much of our work throughout this thesis was numerical. For example, in Chapter 3, we numerically computed the OTOCs for the purpose of extracting the Lyapunov exponent. There are alternative analytical methods in the large N limit to calculate OTOCs exactly through a diagrammatic method by summing Greens functions [49, 50]. This, alongside a CFT description of the model, are still lacking, highlighting further avenues for exploration. Analytics proved useful in our study of QMBS, where we utilised the TDVP framework in order to study the quantum trajectories. In this case, however, our investigation focused on the dynamics with periodicity $K = 1$, yet it would be interesting

to extend it to $K \geq 2$. For example, it is known that $|\mathbb{Z}_3\rangle = |100100100\ldots100\rangle$ state also exhibits revivals in the pure PXP model [19]. This state necessitates a TDVP description with $K = 3$ unit cell, which already gives rise to an intricate phase space at the semiclassical level [214]. It would be intriguing to understand the dynamical phase diagram associated with such states that have larger unit cells, either in the PXP model or analogous models for larger Rydberg blockade radii.

Another important question is whether the results in this thesis hold in higher dimensions. Due to the simplicity and computational advantages, we restricted our work to 1D models. In the case of the chiral model, our initial investigation lends itself to generalisations to $(2+1)$ or $(3+1)$ dimensional black holes following the methodology presented in [261], which would be desirable from a quantum gravity perspective. The teleportation protocol can also be easily extended to higher dimensions (as was done in [150]) by simply entangling Bell states along each row individually. ETH is expected to hold regardless of the dimensionality of the system, so we would expect to still observe maximal thermalisation in the chiral model – particularly with the increased connectivity that arises from the geometry of higher dimensions. For the PXP model, our study numerically identified QMBS states in the 1D Hamiltonian. Studying 2D PXP, and interacting 2D models in general, is well-known to be a computationally difficult task. Meanwhile, the extension to 2D experimentally is straightforward due to the geometry of the platform [255]. Therefore, the phase diagram construction could be used experimentally to study the effect of scarring in 2D PXP where numerics make this task difficult. Contrasting the chiral spin model, it would be useful to investigate how many-body scarring survives the change in geometry in higher dimensions as a means to evade thermalisation.

Finally, it would be beneficial to explore more practical implementations of our findings within quantum technologies. We demonstrated one practical application of thermalisation through the Hayden-Preskill protocol to teleport a single qubit. This could be extended to multiple qubits through traversable wormhole protocol [262–264] which would be more useful in quantum hardware. Finding further protocols that employ thermalisation in an interacting system would be powerful, due to its inevitable presence in interacting systems. Quantum many-body scars have already been realised in superconducting processors [28], yet methods to actually utilise them in quantum hardware – particularly as a form of quantum memory – remains unexplored. Similarly, this is the case for non-Gaussian states like $|\mathbb{Z}_3\rangle$, presented in Chapter 5. These states could serve either as magic states [44] or as a stable qutrit basis [256, 257], due to their ability to avoid scrambling mechanisms.

In conclusion, our findings shed light on the ability of quantum models to control scrambling processes and underscore their practical applications. Yet, much remains

to be understood about the nature of quantum thermalisation. Mastery over classical thermal processes led to transformative technologies like heating and refrigeration – tools we often take for granted. While the impact of quantum thermalisation may not yet rival that of its classical counterpart, there are undoubtedly profound and as-yet-unseen benefits in comprehending this deeply fundamental process. Though ETH brings us close, a rigorous and universally accepted definition of quantum thermalisation remains elusive even today. By furthering our understanding of how to harness and control quantum thermalisation, we move closer to new and exciting discoveries in quantum physics.

Appendix A

Black hole geometry background in the chiral-spin model and Lyapunov fitting details

A.1 Lattice representation of Dirac field in black hole background

A.1.1 Mean field approximation

The system we investigate in Chapter 3 is the one-dimensional spin-$\frac{1}{2}$ chain with the Hamiltonian

$$H = \frac{1}{2}\sum_n \left[-u\left(S_n^x S_{n+1}^x + S_n^y S_{n+1}^y\right) + \frac{v}{2}\chi_n\right], \tag{A.1}$$

where the spin chirality operator is given by

$$\chi_n = \boldsymbol{S}_n \cdot (\boldsymbol{S}_{n+1} \times \boldsymbol{S}_{n+2}), \tag{A.2}$$

where $\boldsymbol{S}_n = \frac{1}{2}(\sigma_n^x, \sigma_n^y, \sigma_n^z)$ is the spin vector, where σ_n^a is the a-Pauli matrix acting on the nth lattice site for $a \in \{x, y, z\}$, and the $u, v \in \mathbb{R}$ are couplings with dimensions of energy. In this Appendix, we assume we are working in the thermodynamic limit.

First we transform from spin operators to Pauli operators. In terms of the Pauli operators, the Hamiltonian is given by

$$\begin{aligned} H = \sum_n \Big[&- \frac{u}{8}\left(\sigma_n^x \sigma_{n+1}^x + \sigma_n^y \sigma_{n+1}^y\right) \\ &+ \frac{v}{32}\epsilon_{abc}\sigma_n^a \sigma_{n+1}^b \sigma_{n+2}^c\Big] \end{aligned} \tag{A.3}$$

where the repeated Latin indices a, b, c are summed over in the chirality term. We now introduce the ladder operators $\sigma_n^{\pm} = (\sigma_n^x \pm i\sigma_n^y)/2$ and the Jordan-Wigner transformation defined by [265]

$$\sigma_n^+ = \exp\left(-i\pi \sum_{m<n} c_m^\dagger c_m\right) c_n^\dagger \tag{A.4}$$

$$\sigma_n^- = \exp\left(i\pi \sum_{m<n} c_m^\dagger c_m\right) c_n \tag{A.5}$$

$$\sigma_n^z = 2c_n^\dagger c_n - 1 \tag{A.6}$$

where c_n are a set of fermionic modes obeying the anti-commutation relations $\{c_n, c_m\} = \{c_m^\dagger, c_n^\dagger\} = 0$ and $\{c_n, c_m^\dagger\} = \delta_{mn}$. After expressing the Hamiltonian in terms of $\sigma_n^{\pm}$ and σ_n^z and then applying the Jordan-Wigner transformation, we arrive at

$$\begin{aligned} H = \frac{1}{4}\sum_n \Bigg[&- u c_n^\dagger c_{n+1} - \frac{iv}{4} c_n^\dagger c_{n+2} \\ &+ \frac{iv}{4}\left(c_n^\dagger c_{n+1}\sigma_{n+2}^z + c_{n+1}^\dagger c_{n+2}\sigma_n^z\right)\Bigg] + \text{H.c.}, \end{aligned} \tag{A.7}$$

where for convenience we have left σ_n^z alone under the assumption that it represents the Jordan-Wigner transformation of Eq. (A.6). We see that the model is intrinsically interacting as the fermionic Hamiltonian contains quartic terms which arise from terms like $c_n^\dagger c_{n+1}\sigma_{n+2}^z$ after explicitly substituting in Eq. (A.6).

To analyse the behaviour of the interacting model, we apply mean field theory (MFT) to transform the Hamiltonian into an effective quadratic Hamiltonian which can be analytically diagonalised. MFT defines the fluctuation of an operator A as $\delta A = A - \langle A\rangle$, where $\langle A\rangle$ is the expectation value of the operator A with respect to the mean field ground state $|\Omega\rangle$. For a product of two operators we have

$$AB = \langle A\rangle B + A\langle B\rangle - \langle A\rangle\langle B\rangle + \delta A \delta B, \tag{A.8}$$

where the second order in fluctuations can be ignored. Applying this to the interacting terms of Eq. (A.7) where we always consider σ_n^z as one of the operators in the product of Eq. (A.7), so replace $\sigma_n^z \to \langle\sigma_n^z\rangle \equiv Z$ and $c_n^\dagger c_{n+1} \to \langle c_n^\dagger c_{n+1}\rangle \equiv \alpha$, where we have assumed translational invariance. These expectation values are done with respect to the

ground state of the mean field Hamiltonian. The Hamiltonian becomes

$$H_{\mathrm{MF}}(\alpha, Z) = \frac{1}{4}\sum_n \Bigg[-\left(u - \frac{iv}{2}Z\right) c_n^\dagger c_{n+1} - \frac{iv}{4} c_n^\dagger c_{n+2} + 4\mu c_n^\dagger c_n \Bigg] + E_0 + \mathrm{H.c.}, \tag{A.9}$$

where $\mu = v\mathrm{Im}(\alpha)/4$ is an effective chemical potential controlling the number of particles in the ground state, $E_0 = v(Z-1)\mathrm{Im}(\alpha)/8$ is a constant energy shift.

Let $|\Omega(\alpha, Z)\rangle$ be the ground state of the Hamiltonian of Eq. (A.9). Self consistency requires

$$\langle\Omega(\alpha, Z)|\sigma_n^z|\Omega(\alpha, Z)\rangle = Z \tag{A.10}$$

$$\langle\Omega(\alpha, Z)|c_n^\dagger c_{n+1}|\Omega(\alpha, Z)\rangle = \alpha \tag{A.11}$$

for all n. While these two equations have many solutions, we can single one out on physical grounds: the fully interacting Hamiltonian of Eq. (A.7) has particle-hole symmetry, $[H, U] = 0$, where U is the particle-hole transformation with $Uc_nU^\dagger = (-1)^n c_n^\dagger$ and $Uc_n^\dagger U^\dagger = (-1)^n c_n$. This symmetry implies that $\langle c_n^\dagger c_n\rangle = 1/2$ and $\langle c_n^\dagger c_{n+1}\rangle \in \mathbb{R}$ in the ground state. If we require the MFT to retain the particle-hole symmetry, then these conditions imply that $Z = \mathrm{Im}(\alpha) = 0$, and the MFT Hamiltonian becomes

$$H_{\mathrm{MF}} = \frac{1}{4}\sum_n \left(-uc_n^\dagger c_{n+1} - \frac{iv}{4} c_n^\dagger c_{n+2}\right) + \mathrm{H.c.}. \tag{A.12}$$

It was shown in Ref. [12] that this mean field limit faithfully describes the second order phase transition exhibited by the full spin model.

A.1.2 The Dirac equation on curved spacetime

We now briefly introduce the Dirac field on a curved spacetime which we shall use in the next section. Suppose we have an $N+1$-dimensional spacetime with metric $g_{\mu\nu}$ and a set of veilbein $\{e_a{}^\mu\}$ and their inverses $\{e_a{}^\mu\}$ which are related to the metric via

$$g_{\mu\nu} = e^a{}_\mu e^b{}_\nu \eta_{ab}, \quad g^{\mu\nu} = e_a{}^\mu e_b{}^\nu \eta^{ab}, \tag{A.13}$$

where $\eta_{ab} = \mathrm{diag}(1, -1, -1, \ldots, -1)$ is the Minkowski metric. The veilbein and their inverses also obey

$$e_a{}^\mu e^b{}_\mu = \delta_b^a, \quad e_a{}^\mu e^a{}_\nu = \delta_\nu^\mu. \tag{A.14}$$

Appendix A. Black hole geometry background in the chiral-spin model and Lyapunov fitting details

The veilbein $\{e_a{}^\mu\}$ are a set of vector fields that form an orthonormal basis at every point in some patch of M. The Latin indices $a, b = 0, 1, \ldots$ refer to the orthonormal frame indices, whilst the Greek indices $\mu, \nu = t, x, \ldots$ refer to the coordinate indices.

Using this, we can introduce spinor fields on a curved spacetime as a field on M which transforms as a spinor under local Lorentz transformations (transformations that act on Latin indices) and as a scalar under coordinate transformations (transformations that act on the Greek indices). The locally Lorentz invariant and coordinate invariant action for spinor field ψ of mass m on an $N+1$ dimensional spacetime M with metric $g_{\mu\nu}$ is given by [266]

$$\begin{aligned} S &= \frac{i}{2}\int_M \mathrm{d}^{N+1}x|e|\left(\bar{\psi}\gamma^\mu D_\mu\psi - \overline{D_\mu\psi}\gamma^\mu\psi + 2im\bar{\psi}\psi\right) \\ &\equiv \int_M \mathrm{d}^{N+1}x\mathcal{L}, \end{aligned} \tag{A.15}$$

where the gamma matrices $\{\gamma^\mu \equiv e^\mu_a\gamma^a\}$ are the curved space gamma matrices which obey the Clifford algebra $\{\gamma^\mu, \gamma^\nu\} = 2g^{\mu\nu}$ and are related to the local flat Minkowski space gamma matrices $\{\gamma^a\}$ which obey the flat space Clifford algebra $\{\gamma^a, \gamma^b\} = 2\eta^{ab}$. The Dirac adjoint is defined as $\bar{\psi} = \gamma^\dagger\gamma^0$ where γ^0 is the flat space gamma matrix. We also have $|e| = \det e^a{}_\mu = \sqrt{-g}$. The covariant derivative of spinors D_μ is defined via

$$D_\mu\psi = \partial_\mu\psi + \Omega_\mu\psi \tag{A.16}$$

where Ω_μ is the spin connection related to the connection of M via

$$\Omega_\mu = \frac{i}{2}\Omega_{ab\mu}\Sigma^{ab}, \quad \Sigma^{ab} = \frac{i}{4}[\gamma^a, \gamma^b] \tag{A.17}$$

and $\Omega_{ab\mu}$ are the components of the connection. For more details, see Ref. [266].

In this study we are interested in the $(1+1)$D spacetimes, in which case the spin connection vanishes from the symmetrised action. To see this, we can substitute in the covariant derivative explicitly

$$\begin{aligned} \mathcal{L} &= \frac{i}{2}|e|\left(\bar{\psi}\gamma^\mu D_\mu\psi - \overline{D_\mu\psi}\gamma^\mu\psi\right) \\ &= \frac{i}{2}|e|\left(\bar{\psi}\gamma^\mu\partial_\mu\psi - \partial_\mu\bar{\psi}\gamma^\mu\psi + \bar{\psi}\{\gamma^\mu, \Omega_\mu\}\psi\right) \end{aligned} \tag{A.18}$$

However, in $(1+1)$D, we have $\Omega_\mu \propto [\gamma^0, \gamma^1] \propto \gamma^3$, where γ^3 is the $(1+1)$D analogue of γ^5. As $\{\gamma^\mu, \gamma^3\} = 0$ for all μ, then the spin connection vanishes and we arrive at the Lagrangian [266]

$$\mathcal{L} = |e|\bar{\psi}\gamma^\mu\overleftrightarrow{\partial_\mu}\psi, \tag{A.19}$$

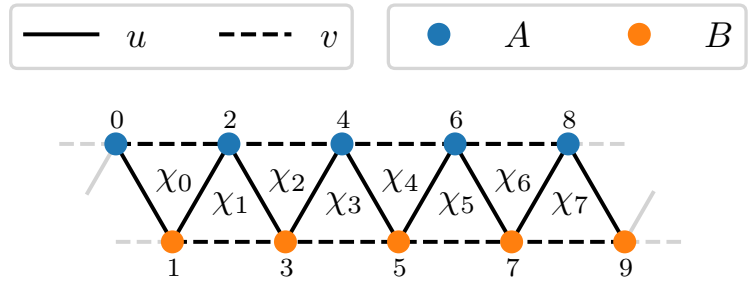

Figure A.1: To reveal the relativistic behaviour, we introduce a two-site unit cell by bicolouring the lattice.

where $A\overset{\leftrightarrow}{\partial_\mu}B = \frac{1}{2}\left(A\partial_\mu B - (\partial_\mu A)B\right)$.

Throughout this we assume that we are working with time-independent metrics, so that the vector $\xi = \partial_t$ is a time-like Killing vector which obeys $\mathcal{L}_\xi g = 0$. In order to perform canonical quantisation of this theory, we introduce the canonical momentum $\pi_a(x)$ of the field and apply the canonical commutation relations. We have

$$\pi = \frac{\partial \mathcal{L}}{\partial \dot{\psi}} = \frac{i}{2}|e|\bar{\psi}\gamma^t \tag{A.20}$$

The equal time canonical Poisson bracket reads

$$\{\psi_\alpha(t,x), \pi_\beta(t,y)\} = i\delta(x-y)\delta_{\alpha\beta} \tag{A.21}$$

where the indices α, β here refer to the spinor indices. This implies that the spinor field obeys the commutation relation

$$\{\psi_\alpha(t,x), \psi^\dagger_\beta(t,y)\} = \frac{(\gamma^0\gamma^t)^{-1}_{\alpha\beta}\delta(x-y)}{|e|}. \tag{A.22}$$

Note that the factor of $1/2$ is missing despite it being present in the canonical momentum π. This is because the canonical momentum defines a constraint on phase space, as π is linearly related to $\psi^\dagger$, which means we must employ the machinery of Dirac brackets instead of Poisson brackets to quantise this theory. It is the Dirac bracket that we upgrade to an anti-commutator using canonical quantisation. More information can be found in Ref. [267–270]. When taking this into account, the factor of $1/2$ vanishes.

A.1.3 Relativistic limit

To make the link with relativity, the lattice sites are now labelled as alternating between sub-lattices A and B by introducing a two-site unit cell, as shown in Fig. A.1. The mean field Hamiltonian of Eq. (A.12) can be re-parametrised as

$$H_{\mathrm{MF}} = \frac{1}{4}\sum_n \Big[-ua_n^\dagger(b_n + b_{n-1}) - \frac{iv}{4}(a_n^\dagger a_{n+1} + b_n^\dagger b_{n+1})\Big] + \mathrm{H.c.}, \tag{A.23}$$

where the fermionic modes a_n and b_n belong to sublattice A and B, respectively, where now n labels the unit cells. These modes obey the commutation relations $\{a_n, a_m^\dagger\} = \{b_n, b_m^\dagger\} = \delta_{nm}$, while all mixed anti-commutators vanish. The index n now labels the unit cells. We Fourier transform the fermionic modes as

$$a_n = \frac{1}{\sqrt{N}}\sum_{p\in \mathrm{B.Z.}} e^{ipan} a_p, \tag{A.24}$$

and similarly for b_n, where N is the number of unit cells in the system, a is the unit cell spacing, and B.Z. $= [0, 2\pi/a)$ is the Brillouin zone and $p = 2m\pi/L$ for $L = Na$ and integer m. The Fourier transformed Hamiltonian becomes

$$H_{\mathrm{MF}} = \sum_{p\in \mathrm{B.Z.}} \chi_p^\dagger h(p)\chi_p, \quad h(p) = \begin{pmatrix} g(p) & f(p) \\ f^*(p) & g(p) \end{pmatrix}, \tag{A.25}$$

where the two-component spinor is defined as $\chi_p = (a_p, b_p)^{\mathrm{T}}$ and the functions are given by

$$f(p) = -\frac{u}{4}(1 + e^{-iap}), \quad g(p) = \frac{v}{8}\sin(ap). \tag{A.26}$$

The dispersion relation is given by the eigenvalues of the single-particle Hamiltonian $h(p)$ which yields

$$E(p) = g(p) \pm |f(p)| = \frac{v}{8}\sin(ap) \pm \frac{u}{4}\sqrt{2 + 2\cos(ap)}. \tag{A.27}$$

In Fig. 3.2, it is seen that the parameter v has the effect of tilting the cones as it increases and one band becomes flat at the Fermi point when $|v|/2 = |u|$.

The Fermi points $\{p_i\}$, defined as the points for which $E(p_i) = 0$, are found at

$$p_0 = \frac{\pi}{a}, \quad p_\pm = \pm\frac{1}{a}\arccos\left(1 - \frac{8u^2}{v^2}\right). \tag{A.28}$$

The roots $p_\pm$ only exist if the argument of arccos is in the range $[-1, 1]$ which implies

$|v|/2 \geq |u|$ for these to appear in the dispersion. Therefore, if $|v|/2 \leq |u|$, the only Fermi point is located at $p_0 = \pi/a$ which is where the Dirac cone is located, as shown in Fig. 3.2. When the cone over-tilts, so when $|v|/2 \geq |u|$, then the additional zero-energy crossings at $p_\pm$ appear which is due to the Nielsen-Ninomiya theorem which states that the number of left- and right-movers must be equal [271, 272].

The continuum limit of a lattice model is an effective theory obtained by letting the lattice spacing $a \to 0$ in such a way that the Fermi velocity remains fixed. In this process, only the linear portion of the dispersion relation, near the Fermi points, is relevant as the non-linear portion of the dispersion goes off to infinite momentum. Therefore, the continuum limit is equivalent to restricting ourselves to a small neighbourhood of the Fermi points in momentum space. We outline this below. See Ref. [273] for more detail.

First we Taylor expand the single-particle Hamiltonian $h(p)$ about the Fermi point p_0 to first order in momentum which yields

$$h(p_0 + p) = \frac{1}{4}\left(u\sigma^y p - \frac{v}{2}\mathbb{I}p\right) \equiv e_a{}^i \alpha^a p_i, \tag{A.29}$$

The coefficients in the second equality are defined as $e_0{}^x = -v/8, e_1{}^x = u/4$, where we have absorbed a factor of a into the couplings as $au \to u$ and $av \to v$, and the Dirac matrices are $\alpha^0 = \mathbb{I}, \alpha^1 = \sigma^y$. We then project the Hamiltonian of Eq. (A.23) into a small region of momentum space centred on p_0 by truncating the summation with a cutoff $\Lambda = O(1/a)$ as

$$\begin{aligned} H &\approx \sum_{|q|<\Lambda} \chi^\dagger_{p_0+q} h(p_0+q) \chi_{p_0+q} \\ &= \sum_{|q|<\Lambda} \chi^\dagger(q) e_a{}^i \alpha^a p_i \chi(q) \end{aligned} \tag{A.30}$$

where we have defined the new momentum space fields $\chi(q) \equiv \chi_{p_0+q}$, where q measures the distance from the Fermi point p_0.

We also truncate the discrete Fourier transform for the lattice fermions from Eq. (A.24) as

$$\begin{aligned} a_n &\approx \frac{1}{\sqrt{N}} \sum_{|q|<\Lambda} e^{i(p_0+q)an} a_{p_0+q} \\ &= e^{ip_0an} \frac{1}{\sqrt{N}} \sum_{|q|<\Lambda} e^{iqan} a(q) \\ &\equiv e^{ip_0an} a(n), \end{aligned} \tag{A.31}$$

which defines a slowly-varying field $a(n)$, and similarly for b_n which is related to $b(n)$ analogously. We see that on the subspace near the ground state, the fermionic operators a_n and b_n consist of a slowly-varying field $a(n)$ and $b(n)$ respectively, with a high-frequency

oscillation $e^{ip_0 an}$ on top [273].

We then take the limit that $a \to 0$ in such a way that the rescaled couplings u and v remain finite (equivalently the Fermi velocity remains fixed) and $Na = L$ remains constant. We also define $na \to x$ which we must remember is the unit cell coordinate. The cutoff $\Lambda \to \infty$ additionally, so the summation is from $\pm\infty$. Performing this limit, real space becomes a continuum and the envelope functions $a(n)$ become

$$a(x) = \lim_{a\to 0} \frac{a(n)}{\sqrt{a}} = \frac{1}{\sqrt{L}} \sum_{q\in \text{B.Z.}} e^{iqx} a(q) \tag{A.32}$$

and similarly for $b(x)$, where now the Brillouin zone has extended to infinity as B.Z. $= [-\infty, \infty]$ with $p = 2m\pi/L$ for $m \in \mathbb{Z}$, where the re-scaling by $1/\sqrt{a}$ ensures that the limits exist and the commutation relations become continuum commutation relations. If we define the two-component spinor field $\chi(x) = (a(x), b(x))^T$, we see that this is related to the momentum space fields derived in Eq. (A.29) by a Fourier transform as

$$\chi(q) = \frac{1}{\sqrt{L}} \int_0^L \mathrm{d}x e^{-iqx} \chi(x). \tag{A.33}$$

With this result in hand, we are now able to transform the truncated Hamiltonian of Eq. (A.30) back into real space, arriving at the Hamiltonian

$$\begin{aligned} H &= \int_{\mathbb{R}} \mathrm{d}x \chi^\dagger(x) \left(-ie_a{}^i \alpha^a \overleftrightarrow{\partial_i} \right) \chi(x) \\ &\equiv \int_{\mathbb{R}} \mathrm{d}x \mathcal{H}, \end{aligned} \tag{A.34}$$

with $A\overleftrightarrow{\partial_\mu} B = \frac{1}{2}\left(A\partial_\mu B - (\partial_\mu A)B\right)$ and the Dirac $\alpha^a = (\mathbb{I}, \sigma^y)$ and $\beta = \sigma^z$. We have ignored the overall factor of $1/4$ here.

This is a Hamiltonian for the slowly-varying envelope function $\chi(x)$. The corresponding action of this theory is given by

$$\begin{aligned} S &= \int d^{1+1}x \left(i\chi^\dagger \overleftrightarrow{\partial_t} \chi - \mathcal{H} \right) \\ &= \int d^{1+1}x i\bar{\chi} e_a{}^\mu \gamma^a \chi \end{aligned} \tag{A.35}$$

where we have defined $\bar{\chi} = \chi^\dagger \gamma^0$ and the gammas are related to the alpha and beta matrices via $\gamma^0 = \beta$ and $\gamma^i = \beta\alpha^i$, where $\gamma^0 = \sigma^z$ and $\gamma^1 = -i\sigma^x$ which obey the anti-commutation relations $\{\gamma^a, \gamma^b\} = 2\eta^{ab}$, with $\eta^{ab} = \mathrm{diag}(1, -1)$. The coefficients are

given by

$$e_a{}^{\mu} = \begin{pmatrix} 1 & -v/8 \\ 0 & u/4 \end{pmatrix}, \quad e^a{}_{\mu} = \begin{pmatrix} 1 & v/(2u) \\ 0 & 4/u \end{pmatrix} \tag{A.36}$$

If we assume that the couplings are upgraded to slowly-varying functions as $u \to u(x)$ and $v \to v(x)$, then the continuum limit is still a good approximation.

This action looks very similar to the action of a Dirac field on a $(1+1)$-dimensional curved spacetime, except two subtle differences. The first is that the integration measure is missing the factor of $|e|$, so it is the flat space volume element. The second is that the fields obey flat space commutation relations

$$\{\chi_\alpha(x), \chi_\beta(y)\} = \delta_{\alpha\beta}\delta(x-y) \tag{A.37}$$

which can be obtained using Eqs. (A.32) and (A.33) and the fact that the component momentum space modes obey $\{a(p), a^\dagger(q)\} = \delta_{pq}$, and similarly for $b(p)$. Therefore, the theory in its current form describes a generalised Dirac action on a flat (1+1)-dimensional space with space-dependent coefficients.

In order to interpret this theory as a curved space theory, we introduce a new field

$$\psi = \frac{\chi}{\sqrt{|e|}} \tag{A.38}$$

then the fields obey the curved space commutation relations

$$\{\psi_\alpha(x), \psi_\beta(y)\} = \frac{\delta_{\alpha\beta}\delta(x-y)}{|e|} \tag{A.39}$$

agreeing precisely with the general commutation relations of Eq. (A.22) using the veilbein of Eq. (A.36). The action of Eq. (A.15) re-expressed in terms of the field ψ is precisely the Dirac action for a spinor on a spacetime with veilbein given in Eq. (A.36). This veilbein corresponds to the metric

$$\mathrm{d}s^2 = \left(1 - \frac{v^2}{4u^2}\right)\mathrm{d}t^2 - \frac{4v}{u^2}\mathrm{d}t\mathrm{d}x - \frac{16}{u^2}\mathrm{d}x^2. \tag{A.40}$$

If the variables u and v are upgraded to slowly-varying functions of space, then the preceding calculation is still valid and the event horizon is located at the point x_h, where $|v(x_h)|/2 = |u(x_h)|$. In the small region in which v is a slowly-varying functions of x, the coupling of different momentum modes will be small and can be ignored to a good approximation, leaving the diagonal terms $a_p^\dagger a_p$ only. This is quite standard to do in lattice model where the continuum is described by a Dirac equation [123, 273, 274]. For

coordinate dependent coefficients, this is the Gullstrand-Painlevé metric [113] also know as the *acoustic metric* which is the Schwarzschild metric of a (1+1)D black hole expressed in Gullstrand-Painlevé coordinates. This metric is referred to here as an *internal metric* of the model as it depends upon the internal couplings of the Hamiltonian and not the physical geometry of the lattice. In addition, this is a fixed classical background metric and the quantum fields have no back-reaction on the metric. Quite remarkably, the phase boundary between the regions for $|v|/2 < u$ and $|v|/2 > u$ can be interpreted as the inner and outer regions of the black hole, where the phase boundary $|u| = |v|/2$ aligns with the event horizon.

In order to transform the metric of Eq. (A.40) into the Schwarzschild metric, a coordinate transformation defined as $(t, x) \mapsto (\tau, x)$ is used, where

$$\tau(t, x) = t - \int_{x_0}^{x} \mathrm{d}z \frac{V(z)}{U^2 - V^2(z)}, \tag{A.41}$$

where we have absorbed some factors into the coupling as $u/4 \to U$ and $v/8 \to V$. This maps the metric to

$$\mathrm{d}s^2 = \left(1 - \frac{V^2(x)}{U^2(x)}\right) \mathrm{d}\tau^2 - \frac{1}{U^2(x)\left(1 - \frac{V^2(x)}{U^2(x)}\right)} \mathrm{d}x^2, \tag{A.42}$$

which takes the general form of the Schwarzschild metric, where the horizon is at the location where the metric becomes singular at $U = V$ which is equivalent to $u = v/2$.

A.2 Fitting the exponent of the Lyapunov vs temperature

In Fig. 3.5, we present the Lyapunov exponent vs temperature in two regimes: in the XY phase ($v = 1$) where the growth is quadratic, and deep in the chiral phase ($v = 8$) where the growth is shown to be linear. In this section, we explicitly show that these fitting forms are suitable in the two limits by additionally parametrising the fit of λ vs T to $a(T^b - c)$ and plotting b against N. The results are shown in Fig. A.2 where we see in XY phase, $b \approx 2$, while in the chiral phase $b \approx 1$, as one would hope. It is important to note that the results of the fit fluctuate dependent on the choice of $T_{\min}$ and $T_{\max}$ in the fitting window. To achieve this, different values have been taken for different N and v, so one must be cautious during the fitting procedure. These results, nonetheless, demonstrate that with a suitable choice of fitting window, a quadratic and linear fit are reasonable to make.

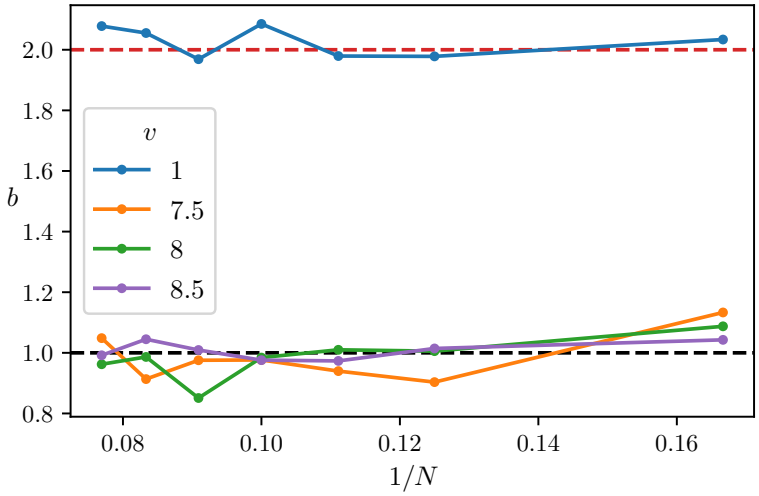

Figure A.2: For different values of v, we fit $\lambda = (a(T^b - c)$ and extract the exponent b, plotting this against $1/N$. We see in XY phase ($v = 1$), this value tends towards 2 (red dashed line) while in the chiral phase, $v > 7.5$, this value tends towards 1 (black dashed line).

Appendix B

Extensions to the quantum teleportation results

B.1 Numerical scaling

In Appendix B.1 we present relevant numerics data on the dependence of the teleportation scheme on system size, and the high temperature behaviour of the Lyapunov exponent for the chiral spin-chain model.

B.1.1 System size scaling

In this section we present results with varying system size to demonstrate the robustness of the protocol with N, expanding upon the results of Fig. 3.7 in Chapter 3. In Fig. B.1, we see that as we increase system size, the fidelity does not drop, but instead increasingly plateaus at a constant value while the scrambling speed remains constant. This indicates a level of robustness with system size, and suggests this will fidelity plateau will persist in the large N limit.

B.1.2 Lyapunov exponent in the infinite temperature limit

In Section. 3.5.2, we stated that in the infinite temperature limit, the Lyapunov exponent saturates to a value $\lambda = 0.78v$ in the Chiral model. Here we supplement that with numerical verification. Fig. B.2 demonstrates this where we see a rapid saturation to $0.78v$ with increasing T irrelevant of system size.

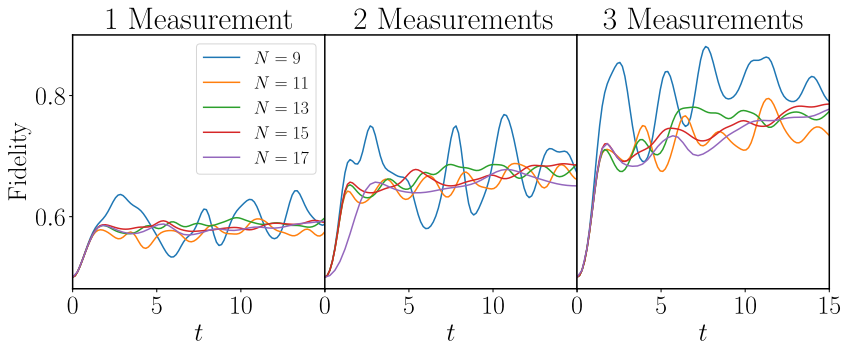

Figure B.1: A comparison of the Fidelity of teleportation with system size N using ED for $u = 1$, $v = 8$. Three panels show the 1, 2 and 3 simultaneous epr measurements respectively. We see with increasing system size, scrambling speed remains the same while the fidelity plateau becomes increasingly evident.

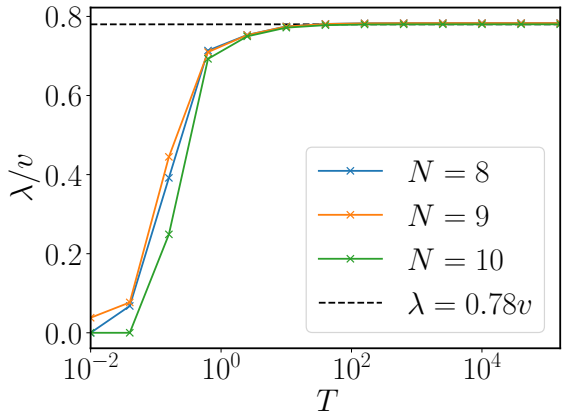

Figure B.2: The scaled Lyapunov exponent, λ/v, versus temperature, T, where colour indicates system size N. We see in the large T limit, λ/v rapidly saturates to the value $\lambda = 0.78v$ with little change with system size. Results are computed using ED.

B.2 Krylov subspace method

In this work we have employed several numerical techniques, the most notable one being a matrix-free Kyrlov subspace method used to achieve higher system sizes than would be possible with the standard exact diagonalisation method. More specifically, we do not calculate Eq. (3.7) exactly, but instead compute the following quantity

$$\tilde{C}_{|\Phi\rangle}(t) = \langle\Phi|\, e^{-\beta H/8+itH} O_l e^{-\beta H/4-itH} O_k \\ e^{-\beta H/4+itH} O_l e^{-\beta H/4-itH} O_k e^{-\beta H/8} \,|\Phi\rangle \quad \text{(B.1)}$$

where $|\Phi\rangle$ is a (normalised) Haar-random state whose components are generated from a Gaussian distribution with zero mean and unit variance. The true value of the OTOC $C(t)$ is then approximated by averaging $\tilde{C}_{|\Phi\rangle}(t)$ over several thousands of different samples of $|\Phi\rangle$. With a matrix-free representation of the Hamiltonian H, which we explain in detail below, this method allows us to eliminate the memory overhead of storing the full matrix form of the Hamiltonian, achieving a dramatic reduction of the memory requirement to that of a small number of Hilbert space vectors. The computation is based on an open-source library [275] that implements this Krylov subspace method efficiently on the GPU, and the source code is publicly available at [276].

To understand this reduction of the memory requirement, one notes that since in general the Hamiltonian is written as a sum of the product of Pauli operators

$$H = \sum_{i_1,\ldots,i_N} \lambda_{i_0\ldots i_N}\, \sigma_{i_0} \cdots \sigma_{i_N}$$

where $\lambda_{i_0\cdots i_N}$ are complex numbers and each σ_i is one of $\{I, \sigma^x, \sigma^y, \sigma^z\}$ defined on site i, it is unnecessary to store the full 2^N by 2^N dimensional matrix form of the Hamiltonian in memory. Instead, storing the coefficients $\lambda_{i_0\ldots i_N}$ is sufficient to compute the action of the Hamiltonian on a state, since the actions of each Pauli operators on the state can be trivially realised with (a combination of) swapping and scalar multiplications on the coefficients of the state vector. Starting with a state vector $|v\rangle$, using this this matrix-free action of the Hamiltonian one can build a sequence of vectors

$$|v\rangle, H|v\rangle, H^2|v\rangle, \cdots, H^n|v\rangle$$

which spans a linear subspace, known as a Krylov subspace of the full Hilbert space. Diagonalising within the Krylov subspace and iterating this process then allow one to compute the action of the exponential of the Hamiltonian on the state vector to an arbitrary degree of precision. The GPU-computing library [275] that we have employed in this project implements the restarted Krylov subspace method as described in Ref. [277]. We choose the dimension of the Krylov subspace $n = 5$ which we have found to strike a balance between computational speed and memory usage, and set the tolerance of the calculation (given by the L_2-norm of the difference of the result vectors between two iterations) to the machine precision.

Contrasting with the standard exact diagonalisation method commonly used in computing the matrix exponential, we have found that the Krylov subspace method leads to considerably faster computational time and much reduced memory requirement, while offering the same accuracy, as is shown in Fig. 3.5 where we have compared the results of either methods in the regime where both can be applied. The reduction of the storage of

a 2^N by 2^N matrix to a few 2^N-dimensional vectors allows the Krylov subspace method to reach twice the system size than is feasible with the exact diagonalisation method, given the same amount of computational resources. In general, the convergence of the Krylov subspace method depends on the norm of the operator being exponentiated, and we have found that the method takes longer time to converge as one increases N, β, and t. It is expected that the method eventually breaks down for sufficiently large system size, and our code will throw errors in this case so the user will be informed that the calculation is no longer to be trusted.

Appendix C

Further details on the many-body scarring phase diagram

C.1 Other regions of the phase diagram

Several regions of the phase diagram in Fig. 4.4 exhibit fidelity revivals that have a simple origin that can be understood without invoking QMBS. Here we explain in more detail these regions labelled (4), (5), (6) and (7). It is useful to consider the Inverse Participation Ratio (IPR), one of the traditional measures of ergodicity of the eigenfunctions introduced in the context of Anderson localisation [278]. The IPR is defined as

$$\mathrm{IPR} = \frac{1}{\sum_E |\langle E|\psi\rangle|^4}, \tag{C.1}$$

and it intuitively tells us about how many basis states $|E\rangle$ the state $|\psi\rangle$ has support on. For example, if $|\psi\rangle$ is a basis state, its IPR will be 1, while if $|\psi\rangle$ is homogeneously spread over the entire Hilbert space, the IPR will be equal to the Hilbert space dimension. Note that IPR is a basis-dependent quantity and, in our case, we have a natural choice of eigenstates $|E\rangle$ of $H_{\mathrm{PXP}}(\mu_{\mathrm{f}})$ as the basis states.

The log of IPR for μ_{i} ground states with respect to μ_{f} eigenstates is plotted in Fig. C.1. This allows us to further distinguish between different regions. For conventional $|\mathbb{Z}_2\rangle$ scarring we expect the IPR to be on the order of system size N, since the $|\mathbb{Z}_2\rangle$ state has high overlap with a band of $N+1$ scarred eigenstates of $H_{\mathrm{PXP}}(0)$ but low overlap with the rest. This is evidenced in region (1) of Fig. C.1. On the other hand, the band of scarred eigenstates associated with $|0\rangle$ state in the detuned PXP model is "tilted" to one edge of the spectrum, so we expect the IPR to be smaller. In general, the regions with high IPR are expected to be ergodic, while the least interesting regimes are characterised

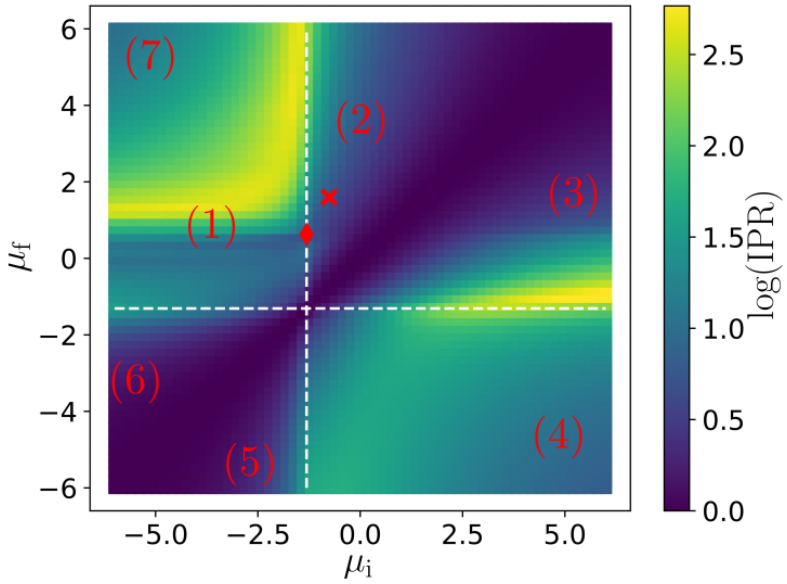

Figure C.1: Logarithm (base 10) of the IPR of the ground state of $H_{\mathrm{PXP}}(\mu_i)$ with respect to the eigenstates of $H_{\mathrm{PXP}}(\mu_f)$. All the labels have the same meaning as in Fig. 4.4. Data is obtained using exact diagonalisation in the sector with $k = 0$ momentum and $p = +1$ inversion symmetry for size $N = 26$ with PBCs.

by very low IPR, such as around the $\mu_i = \mu_f$ diagonal and in regions (5) and (6). The IPR is not as low in parts of regions (4) and (7) visible in this figure, but it decreases with increasing $|\mu_i|$ and $|\mu_f|$ as the ground state of $H_{\mathrm{PXP}}(\mu_i)$ approaches an eigenstate of $H_{\mathrm{PXP}}(\mu_f)$.

Large $|\mu_f|$ leads to fragmentation of the Hilbert space, which can effectively trap the initial state in a simple oscillating superposition [279]. For example, region (4) [i.e., $\mu_i > 0$, $-\mu_f \gg 1$] roughly corresponds to the polarised state in the strongly detuned regime, since the initial ground state has significant overlap with $|0\rangle$ for $\mu_i > 0$. In the $\mu_i \to \infty$ limit, it is expected to become the exact mirror image of region (3), given that the polarised state has the same dynamics for $\pm\mu_f$ (see Ref. [220]). Similarly, region (7) [$\mu_i < 0$, $\mu_f \gg 1$] has a simple explanation in terms of $|\mathbb{Z}^+\rangle$ state in the strongly detuned regime.

The origin of revivals in region (5) [$\mu_f < \mu_i < -1.3$] is perhaps not immediately obvious, since the initial state in that case does not have high overlap with one of the previously studied states such as $|0\rangle$ or $|\mathbb{Z}^+\rangle$. We now briefly investigate this region. The fidelity and the average number of excitations after quenching from $\mu_i = -2.5$ to $\mu_f = -6$ can be seen in Figs. C.2(a) and (b). The quenched state maintains high overlap with the $|\mathbb{Z}^+\rangle$ state, with peaks in the middle between the fidelity revivals, see Fig. C.2(a). This situation is reminiscent of the $|\bar{0}\rangle$ state in region (2), which periodically evolves

to $|0\rangle$ and back. Although it oscillates, the overlap with $|\mathbb{Z}^+\rangle$ never drops to zero. In contrast, the overlap with $|0\rangle$ is constantly zero. In Fig. C.2(b) we also see that the average occupation is remarkably stable, fluctuating only slightly around ≈ 0.47. As explained above for regions (4) and (7), such behaviour arises due to the fact that in the large-μ limit the Hilbert space becomes fragmented and the initial state has support on a small number of eigenstates that are disconnected from the rest. This can be seen in Fig. C.2(c), which shows the overlap of the initial state and the eigenstates. The fragmentation and high overlap with the ground state are apparent. Further evidence comes from the inverse participation ratio (IPR), which we find to be very low in this region, indicating overlap with only a small number of eigenstates, as will be shown below. Finally, region (6) [$\mu_\mathrm{i} < \mu_\mathrm{f} < -1.3$] has a similar phenomenology to its mirroring region (5).

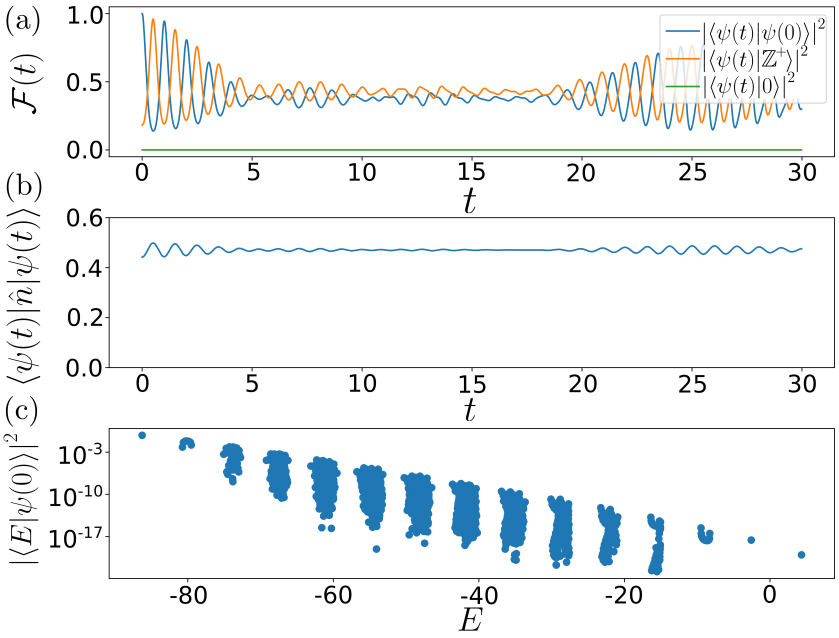

Figure C.2: Dynamics and eigenstate properties of the PXP model quenched from $\mu_\mathrm{i} = -2.5$ to $\mu_\mathrm{f} = -6$, corresponding to region (5) of the phase diagram in Fig. 4.4. (a) Fidelity of the initial state $|\psi(0)\rangle$, i.e., the ground state of $H_\mathrm{PXP}(-2.5)$, as well as the overlap with both the polarised state $|0\rangle$, and superposition state $|\mathbb{Z}^+\rangle$. (b) The average number of excitations remains nearly constant in time. (c) The overlap of the initial state with eigenstates of $H_\mathrm{PXP}(-6)$ reveals fragmentation and large projection on the ground state. Data obtained by exact diagonalisation for $N = 28$ with PBCs.

In summary, we have argued that regions (4), (7) and part of (5) correspond to regimes where μ_f has a large absolute value, leading to a simple oscillatory dynamics due to Hilbert space fragmentation, while in regions (5) and (6), $\mu_\mathrm{f} \approx \mu_\mathrm{i}$ causes the

initial state to be close to an eigenstate of the post-quench Hamiltonian. be close to an eigenstate of the post-quench Hamiltonian.

C.2 Derivation of TDVP equations of motion and quantum leakage

In this section we first derive the TDVP equations of motion and then compute the instantaneous leakage rate. These derivations follow Appendices A and C of Ref. [214].

C.2.1 Equations of motion

The TDVP equations of motion can be derived as the saddle point equations for the following Lagrangian [210, 212]:

$$\mathcal{L} = \frac{i}{2}\left(\langle\psi_{\mathrm{MPS}}|\dot{\psi}_{\mathrm{MPS}}\rangle - \langle\dot{\psi}_{\mathrm{MPS}}|\psi_{\mathrm{MPS}}\rangle\right) - \langle\psi_{\mathrm{MPS}}\,|H|\,\psi_{\mathrm{MPS}}\rangle, \tag{C.2}$$

where it will be convenient to split our Hamiltonian into two terms, $H = H_{\mathrm{PXP}} + H_{\mu}$. Unlike Ref. [214], we restrict to $K = 1$ which greatly simplifies the calculation. Throughout this section we will consider mixed MPS transfer matrices, denoted by

$$T_C^B = \sum_{\sigma} \bar{B}^{\sigma} \otimes C^{\sigma}, \tag{C.3}$$

where B and C are arbitrary MPS tensors. The MPS transfer matrix for the PXP ansatz chosen in the Chapter 4 takes the form

$$T_A^A = T = \begin{pmatrix} \cos^2\theta & 0 & 0 & 1 \\ \cos\theta\sin\theta & 0 & 0 & 0 \\ \cos\theta\sin\theta & 0 & 0 & 0 \\ \sin^2\theta & 0 & 0 & 0 \end{pmatrix}. \tag{C.4}$$

Appendix C. Further details on the many-body scarring phase diagram

The dominant left and right eigenvalues of the transfer matrix are equal to 1, and the corresponding eigenvectors are

$$|R) = \begin{pmatrix} 1 \\ \cos\theta\sin\theta \\ \cos\theta\sin\theta \\ \sin^2\theta \end{pmatrix}, \quad (L| = \begin{pmatrix} 1 & 0 & 0 & 1 \end{pmatrix}, \tag{C.5}$$

which obey $(L|R) = 1 + \sin^2\theta$. We also introduce the following shorthand for a 3-site local Hamiltonian term contracted with MPS tensors on every site:

$$\mathcal{H} = \mathcal{H}^{A,A,A}_{A,A,A} = \sum_{\sigma_i} \bar{A}^{\sigma_1}\bar{A}^{\sigma_2}\bar{A}^{\sigma_3} h^{\sigma_1,\sigma_2,\sigma_3}_{\sigma_4,\sigma_5,\sigma_6} A^{\sigma_4}A^{\sigma_5}A^{\sigma_6}. \tag{C.6}$$

Using the mixed transfer matrix expression, it is straightforward to compute

$$f = -iN\frac{\left(L\left|T_A^{\partial\phi A}\right|R\right)}{(L|R)} = N\frac{2\sin^2\theta}{\cos 2\theta - 3}, \tag{C.7}$$

$$\text{with } T_A^{\partial\phi A} = \begin{pmatrix} 0 & 0 & 0 & -i \\ 0 & 0 & 0 & 0 \\ 0 & 0 & 0 & 0 \\ 0 & 0 & 0 & 0 \end{pmatrix}. \tag{C.8}$$

Next we compute the expectation value of the Hamiltonian. We find the two terms are:

$$\langle\psi\,|H_{\mathrm{PXP}}|\,\psi\rangle = N\frac{(L\,|H_{\mathrm{PXP}}|\,R)}{(L|R)} = N\frac{2\cos^2\theta\sin\theta\sin\phi}{1+\sin^2\theta}, \tag{C.9}$$

and

$$\langle\psi\,|H_\mu|\,\psi\rangle = N\frac{(L\,|H_\mu|\,R)}{(L|R)} = N\mu\frac{\sin^2\theta}{1+\sin^2\theta}. \tag{C.10}$$

The total expectation value is given by $\langle\psi|H|\psi\rangle = \langle\psi\,|H_{\mathrm{PXP}}|\,\psi\rangle + \langle\psi\,|H_\mu|\,\psi\rangle$, which yields the energy density, Eq. (4.16) in Chapter 4.

To get the equations of motion for θ and ϕ, we need to compute

$$\eta = \partial_\theta f = -4N\frac{\sin 2\theta}{(\cos^2\theta - 3)^2} \tag{C.11}$$

From there the equations of motion are given by

$$\dot{\theta} = \frac{1}{\eta}\partial_\phi \langle\psi|H|\psi\rangle, \quad \dot{\phi} = -\frac{1}{\eta}\partial_\theta \langle\psi|H|\psi\rangle, \tag{C.12}$$

which lead to Eqs. (4.13)-(4.14) in Chapter 4.

C.2.2 Instantaneous leakage

The instantaneous leakage is given by

$$\begin{aligned}\Lambda^2(\theta) &= \||\dot{\psi}\rangle - iH|\psi\rangle\|^2 \\ &= \langle\psi\left|H^2\right|\psi\rangle_c - 2\dot{\theta}\,\mathrm{Im}\left(\langle\partial_\theta\psi \mid H\psi\rangle_c\right) \\ &+ (\dot{\theta})^2\,\mathrm{Re}\left(\langle\partial_\theta\psi \mid \partial_\theta\psi\rangle_c\right) - 2\dot{\phi}\,\mathrm{Im}\left(\langle\partial_\phi\psi \mid H\psi\rangle_c\right) \\ &+ (\dot{\phi})^2\,\mathrm{Re}\left(\langle\partial_\phi\psi \mid \partial_\phi\psi\rangle_c\right) + 2\dot{\phi}\dot{\theta}\,\mathrm{Re}\left(\langle\partial_\phi\psi \mid \partial_\theta\psi\rangle_c\right)\end{aligned} \tag{C.13}$$

Due to the gauge choice, the leakage depends on connected correlators defined as

$$\langle\partial_\theta\psi|\partial_\theta\psi\rangle_c = \langle\partial_\theta\psi|\partial_\theta\psi\rangle - \langle\partial_\theta\psi|\psi\rangle\langle\psi|\partial_\theta\psi\rangle.$$

In order to evaluate these connected correlators, we introduce the projector on the dominant subspace, $\mathcal{P} = |R)(L|/(L|R)$, and its complement $\mathcal{Q} = \mathbf{1} - \mathcal{P}$. We also introduce $\mathcal{T}$, which is obtained by re-summing the contribution of the non-dominant subspace of T in $\sum_{q=0}^{\infty} T^q$ and is defined from $\mathcal{T}^{-1} = \mathcal{Q}(\mathbf{1} - \mathcal{Q}T\mathcal{Q})^{-1}\mathcal{Q}$.

Let us now evaluate the various terms involved in the instantaneous leakage. Taking each term one by one, we find that:

$$\begin{aligned}&\langle\partial_\theta\psi \mid \partial_\theta\psi\rangle_c = \\ &= \frac{N}{(L \mid R)}\big(L \mid T^{\partial_\theta A}_{\partial_\theta A} + T^{A}_{\partial_\theta A}\mathcal{T}^{-1}T^{\partial_\theta A}_{A} \\ &+ T^{\partial_\theta A}_{A}\mathcal{T}^{-1}T^{A}_{\partial_\theta A} - T^{A}_{\partial_\theta A}\mathcal{P}T^{\partial_\theta A}_{A} \mid R\big),\end{aligned} \tag{C.14}$$

which after a straightforward calculation evaluates to

$$\langle\partial_\theta\psi|\partial_\theta\psi\rangle_c = \frac{N}{1+\sin^2\theta}. \tag{C.15}$$

Turning our attention to the term $\langle\partial_\theta\psi|H|\psi\rangle_c$, we find that this evaluates to

$$\frac{N}{(L \mid R)}\left(L\left|\mathcal{H}_{\partial_\theta A} + \mathcal{H}\mathcal{T}^{-1}T^{A}_{\partial_\theta A} + T^{A}_{\partial_\theta A}\mathcal{T}^{-1}\mathcal{H} - 3\mathcal{H}\mathcal{P}T^{A}_{\partial_\theta A}\right| R\right) \tag{C.16}$$

This yields

$$\langle \partial_\theta \psi | H | \psi \rangle_c = -iN \cos\theta \cos\phi + N \frac{\cos\theta \sin\theta}{\left(1+\sin^2\theta\right)^2} \dot{\phi}. \tag{C.17}$$

As we are only interested in the imaginary part, we can discard the second term and are left with

$$\mathrm{Im}\left(\langle \partial_\theta \psi | H | \psi \rangle_c\right) = -N \cos\theta \cos\phi = \frac{N}{1+\sin^2\theta} \dot{\theta}. \tag{C.18}$$

The expressions containing the derivatives with respect to ϕ can be calculated similarly. Starting with $\langle \partial_\phi \psi | \partial_\phi \psi \rangle_c$ which we compute as

$$\begin{aligned} &\frac{N}{(L \mid R)} \big(L \big| T^{\partial_\phi A}_{\partial_\phi A} + T^{A}_{\partial_\phi A} \mathcal{T}^{-1} T^{\partial_\phi A}_{A} \\ &+ T^{\partial_\phi A}_{A} \mathcal{T}^{-1} T^{A}_{\partial_\phi A} - T^{A}_{\partial_\phi A} \mathcal{P} T^{\partial_\phi A}_{A} \big| R \big) \end{aligned} \tag{C.19}$$

Evaluating this term, we find

$$\langle \partial_\phi \psi | \partial_\phi \psi \rangle_c = N \frac{\cos^2\theta \sin^2\theta}{\left(1+\sin^2\theta\right)^3}. \tag{C.20}$$

The next term to compute is the cross-term

$$\begin{aligned} \langle \partial_\phi \psi | \partial_\theta \psi \rangle_c = \frac{N}{(L \mid R)} \big(L \big| T^{\partial_\phi A}_{\partial_\theta A} + T^{A}_{\partial_\theta A} \mathcal{T}^{-1} T^{\partial_\phi A}_{A} \\ + T^{\partial_\phi A} \mathcal{T}^{-1} T_{\partial_\theta A} - T_{\partial_\theta A} \mathcal{P} T^{\partial_\phi A} \big| R \big). \end{aligned} \tag{C.21}$$

The result after evaluating Eq. (C.21) is

$$\langle \partial_\phi \psi | \partial_\theta \psi \rangle_c = -iN \frac{\cos\theta \sin\theta}{\left(1+\sin^2\theta\right)^2}, \tag{C.22}$$

however, because its real part is identically zero, we get no contribution from this term. We now compute $\langle \partial_\phi \psi | H | \psi \rangle_c$ as

$$\begin{aligned} \langle \partial_\phi \psi | H | \psi \rangle_c = \frac{N}{(L \mid R)} \big(L \big| \mathcal{H}_{\partial_\phi A} + \mathcal{H} \mathcal{T}^{-1} T^{A}_{A \partial_\phi A} \\ + T^{A}_{\partial_\phi A} \mathcal{T}^{-1} \mathcal{H} - 3 \mathcal{H} \mathcal{P} T_{\partial_\phi A} \big| R \big). \end{aligned} \tag{C.23}$$

We find this can be expressed as:

$$\langle \partial_\phi \psi | H | \psi \rangle_c = N \cos\theta \cos\phi + iN \frac{\cos^2\theta \sin^2\theta}{\left(1+\sin^2\theta\right)^3} \dot{\phi} \tag{C.24}$$

We now move onto the terms involving the square of the Hamiltonian, H^2. The connected correlator in this case is

$$\left\langle \psi \left| H^2 \right| \psi \right\rangle_c = N \frac{\left(L \left| \mathcal{H}^{(2)} + 2\mathcal{H}\mathcal{T}^{-1}\mathcal{H} - 5\mathcal{H}\mathcal{P}\mathcal{H} \right| R\right)}{(L \mid R)}. \tag{C.25}$$

where $\mathcal{H}^{(2)}$ is $\mathcal{H}$ evaluated for a two-local Hamiltonian terms that overlap on one, two or three sites. Evaluating this expression, we obtain

$$\left\langle \psi \left| H^2 \right| \psi \right\rangle_c = \frac{N \sin^6\theta}{1+\sin^2\theta} + \frac{N \cos^2\theta \sin^2\theta (\dot{\phi})^2}{\left(1+\sin^2\theta\right)^3} + \frac{N(\dot{\theta})^2}{1+\sin^2\theta}.$$

Substituting each of these into the equation for the leakage, we finally arrive at:

$$\Lambda^2 = N \frac{\sin^6\theta}{1+\sin^2\theta}$$

Rescaling this by the system size yields the intensive expression for the leakage γ^2, Eq. (4.15), quoted in Chapter4.

C.3 Preparation of states in the TDVP manifold

Here we demonstrate that states belonging to the TDVP manifold, ψ_{MPS}, can be mapped ground states of the PXP model with a suitably generalised chemical potential term and unit-cell modulated phase pulse. In a recent work [258], a method of "optimal steering" has been devised to smoothly prepare a class of PXP ground states based on the minimisation of quantum leakage along the trajectory.

We follow a simpler approach and numerically optimise the overlap

$$\left| \langle \psi_{\mathrm{MPS}}(\{\mathbf{x}\}) | \Psi(\mathbf{w}) \rangle \right|^2, \tag{C.26}$$

where $|\Psi(\mathbf{w})\rangle$ is the ground state of the PXP model with a K-site periodic density modulation,

$$H(\mathbf{w}) = \sum_{j=0}^{N-1} P_{j-1} X_j P_{j+1} + \sum_{j=0}^{N-1} w_j n_j, \tag{C.27}$$

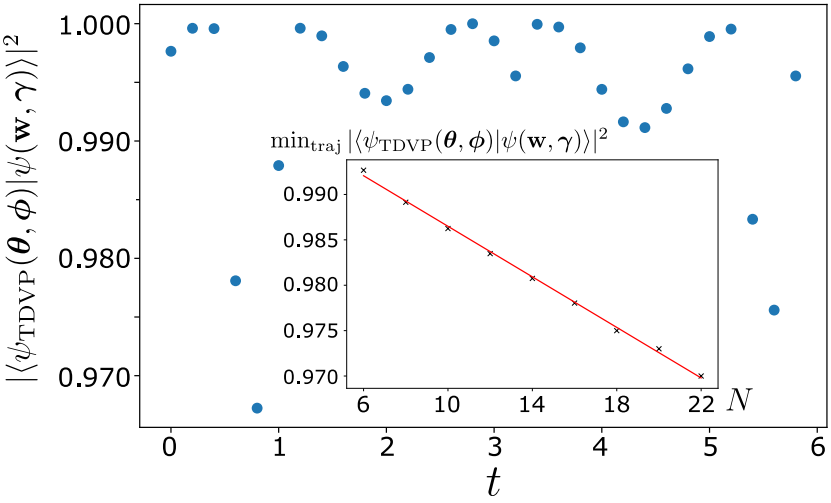

Figure C.3: Preparing the states along a particular $K = 2$ TDVP trajectory (defined in the text) using the ansatz in Eqs. (C.27)-(C.28). A set of states on the trajectory up to time $t = 6$ are variationally approximated in system sizes $N = 6-18$, finding the optimal parameters $\mathbf{w}$, $\boldsymbol{\gamma}$. The optimised parameters are then extrapolated to size $N = 22$ and the resulting overlap with the TDVP states is plotted, illustrating the success of the optimisation (overlap is $> 97\%$ along the entire trajectory). Inset shows the scaling of the overlap for the most poorly approximated point on the trajectory as a function of system size N. The overlap decays slowly and its extrapolation yields high overlap for this point even in large systems (e.g., overlap $\sim 90\%$ at size $N \sim 50$).

where $\mathbf{w} = (w_1, w_2, \ldots, w_j, \ldots, w_K)$ is a generalisation of the chemical potential term that is periodic (with period K) but takes different values for different atoms within the unit cell. The Hamiltonian $H(\mathbf{w})$ reduces to the PXP Hamiltonian with uniform chemical potential in Eq. (4.2) for $K = 1$.

Crucially, in order to prepare the states in larger TDVP manifolds with unit cells $K \geq 2$, we found it necessary to act on the ground state of Eq. (C.27) with a unit-cell modulated phase pulse:

$$\Theta(\boldsymbol{\gamma}) = \prod_{j=0}^{N/K-1} e^{-i\gamma_K Z_{Kj+(K-1)}} \cdots e^{-i\gamma_2 Z_{Kj+1}} e^{-i\gamma_1 Z_{Kj}}, \tag{C.28}$$

where Z_i denotes the usual Pauli-Z matrix on site i and $\gamma_1, \ldots, \gamma_K$ are variational parameters in addition to $\mathbf{w}$. Extensive numerical sampling in system sizes $N \leq 20$ confirms that the ansatz in Eqs. (C.27)-(C.28) allows for an accurate approximation of states in the TDVP manifold after optimising for $(\mathbf{w}, \boldsymbol{\gamma})$ for both the $K = 1$ and $K = 2$ TDVP manifold.

As a test case, we choose a particularly interesting TDVP trajectory which starts at $(\theta_1, \theta_2, \phi_1, \phi_2)$=(1.25$\pi$,2.985,0.166,0.188). This trajectory was derived in Ref. [214] within a $K = 2$ TDVP ansatz and it belongs to a regular region of the manifold, giving rise to oscillations in the fidelity. We choose this trajectory to show that the ansatz can capture trajectories of interest in larger manifolds as it is already proven to be sufficient in Fig 4.7(b) for the simpler $K = 1$ manifold with accuracy $> 90\%$.

We optimise for 30 states evenly spaced along this TDVP trajectory between time $t = 0$ and $t = 6$ in system sizes ranging from $N = 6$ to $N = 18$. The optimisation yields an overlap close to 1 for all the points on the trajectory and a set of optimal (w_1, w_2) and (γ_1, γ_2) for different N. Over the range of N, we found $\boldsymbol{\gamma}$ changes little so we do not re-optimise this in larger N but simply take the average from smaller sizes. On the other hand, we find $\mathbf{w}$ for different values of N fits well the empirical formula $w_j = ae^{bN+c} + d$, where a, b, c and d are fitting parameters depending on w_1 and w_2. With this information, we can calculate (w_1, w_2), (γ_1, γ_2) for larger system sizes via extrapolation.

The resulting overlap in system size $N = 22$ is shown in Fig. C.3. We see that the ansatz successfully captures the entire trajectory (up to 97% overlap in this system size). In the inset of Fig. C.3 the minimum overlap found along the trajectory is plotted as a function of system size, showing that it decays very slowly and allows to prepare the TDVP states on the trajectory with accuracy of 90% or better in large systems $N \sim 50$.

C.4 Single mode approximation

In Sec. 4.5 we have discussed the revivals from the critical ground state based on the structure of the low energy spectrum at $\mu_\mathrm{f} = 0.633$. In this section we provide more details of this analysis, in particular on the range of μ that it can be applied to. Ref. [224] showed that for $\mu_\mathrm{f} = 0$, the scarred states throughout the spectrum could be well approximated as a collection of magnons with momentum π. Here, we show that this analysis also holds for $\mu_\mathrm{f} \approx 0.6$, especially in the low-energy part of the spectrum. In turn, the ground state at $\mu_\mathrm{i} = \mu_\mathrm{c} = -1.31$ can be understood as mainly being a superposition of these multi-magnon states.

In Fig. C.4 one can see the low-energy spectrum resolved by momentum for three different values of μ_f. The data for the overlap of the same eigenstates with the ground state at $\mu_\mathrm{f} = \mu_\mathrm{c} = -1.31$ is also plotted in Fig. C.5. Note that, as this ground state has $k = 0$, only the eigenstates with the same momentum value will have a non-zero overlap. For too small values of μ, the one-magnon states merge into the two-magnon continuum near $k = 0$, causing the band to bend downwards. As a consequence, the non-interacting magnon pairs approximation is less accurate for $k \neq \pi$, and the critical ground state has

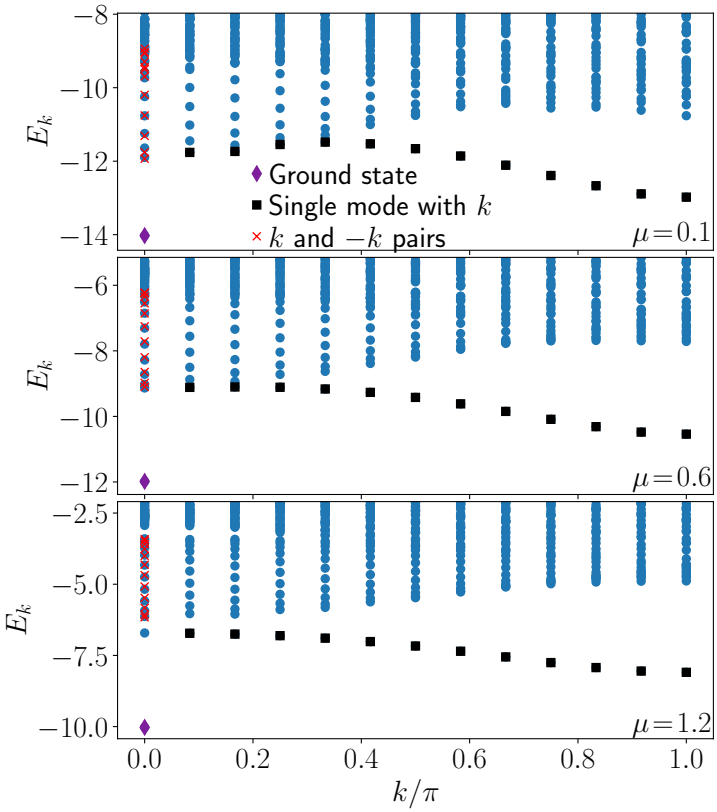

Figure C.4: Low-energy spectrum of the PXP model for three values of μ. The red crosses correspond to the energies of a non-interacting pair of excitations with momenta k and $-k$. For $\mu = 0.1$, the first band merges with the two-magnon continuum. For $\mu = 1.2$, the first excited state with $k = 0$ has an energy that differs from that of two non-interacting magnons. Data is for system size $N = 24$ with PBCs.

increased overlap with them. On top of this, the band being far from flat at the edges means that the towers of states are not sharp, i.e., states near the top of the towers have a non-negligible energy difference. As their energy separation from the ground state is roughly twice that of a single-magnon with momentum k, the flatter the band the more similar in energy the states will be.

For $\mu_{\mathrm{f}} \approx 0.6$, the single-magnon band barely touches the two-magnon continuum. The magnon-pair approximation now holds well for all values of k. Consequently, one can see that the overlap of the critical ground state with two-magnon states built out of magnons with momentum $k \neq \pi$ is very low. Among these, the states with the highest overlap are the ones made from magnons with momentum close to 0 or π. As the band is flat near these points, they have approximately the same energy as the scarred states and so do not lead to dephasing until late times.

Finally, when μ_{f} becomes too large, the nature of the excitations changes and the π

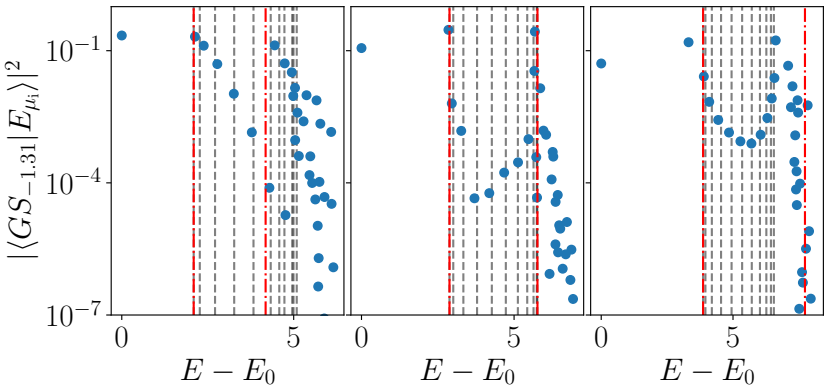

Figure C.5: Overlap between the ground sate at $\mu_i = \mu_c = -1.31$ and the low-energy eigenstates of the PXP model with various values of μ for $N = 24$ and PBCs. The states are the same as in Fig. C.4 with $k = 0$, and panels correspond to $\mu_f = 0.1$, 0.6 and 1.2 respectively (from left to right). The red lines correspond to the expected energy of two and four magnons with momentum π on top of the ground state. The grey line correspond to the expected energy of two magnons with momentum k and $-k$ on top of the ground state. Due to the flatness of the band and the weak interactions between magnons, the towers of states are sharper around $\mu = 0.633$.

magnons no longer describe the elementary excitations in the system. Indeed, for $\mu_f \gg 1$, the ground state is simply the polarised state and the excitations are just a single flip 1 on top of the background of 0. So the first excited state with $k = 0$ is simply a symmetric superposition of the the state $|100\cdots0\rangle$ and its translations. As any kind of excitation with $k = \pi$ will need at least one 1 site, adding two of them that are non-interacting will never lead to the correct excited state at $k = 0$. This can already be seen for $\mu_f = 1.2$ in the bottom panel of Fig. C.4, as the lowest red cross – corresponding to the expected energy of two non-interacting magnons – is far above the actual first excited state with $k = 0$. This again impacts the sharpness of the towers of states, especially the spacing between the first and second excited state, which grows with μ_f.

C.5 Experimental protocol for a scarring phase diagram

We believe it important to address the experimental observation of the phase diagram in Fig. 4.4. The key step is the preparation of the PXP ground state in Eq. (4.2), as typically quenches and observable measurements are already available on current quantum hardware. The protocol below is directly applicable to Rydberg atom arrays [17], however it can also be adapted to ultracold bosons in a tilted optical lattice, where the chemical potential μ maps to the energy mismatch between the Hubbard interaction and electric field which induces a tilt potential [27].

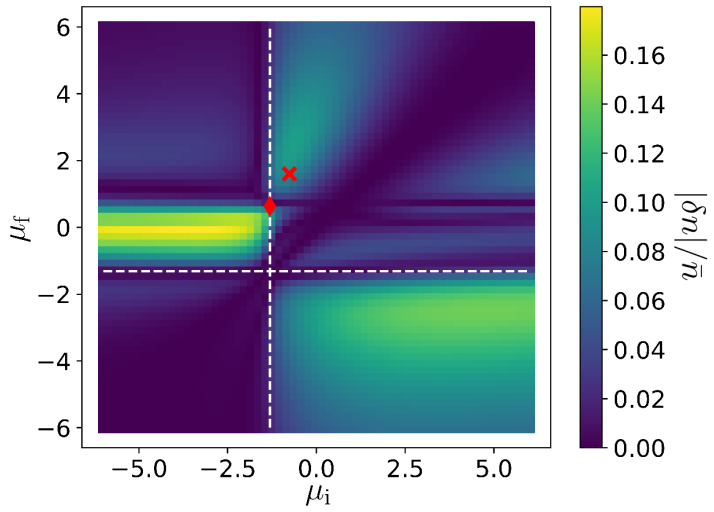

Figure C.6: The norm of the scaled difference of the number of excitations between the diagonal and canonical ensembles when quenching the initial ground state of $H_{\mathrm{PXP}}(\mu_{\mathrm{i}})$ to $H_{\mathrm{PXP}}(\mu_{\mathrm{f}})$. All the labels are the same as in Fig. 4.4. Data is obtained using exact diagonalisation in the momentum $k = 0$ and $p = +1$ inversion symmetry sector for system size $N = 28$ with PBCs.

Ground state preparation is accomplished via a "ramping" procedure utilised in related experiments [16,46,196,280,281]. This assumes fine control of the chemical potential that is varied in time, $\mu = \mu(t)$. Taking the chemical potential very large, $\mu \to \pm\infty$, one can prepare $|0\rangle$ and $|\mathbb{Z}_2\rangle$ states. Starting in one of these states, one can then ramp to a desired ground state in the interior of our phase diagram in Fig. 4.4 by evolving with a time-dependent PXP Hamiltonian, $H_{\mathrm{PXP}}(\mu(t))$, where $\mu(t)$ is appropriately parametrised for an adiabatic evolution, as specified below. The adiabaticity implies that the ramping will not be able to prepare the critical ground state after a finite time in the thermodynamic limit. Therefore, with finite resources, we can only hope to approach the critical point from different gapped regions of the phase diagram. We start the ramp either in $|\mathbb{Z}_2\rangle$ or $|0\rangle$, depending on whether we are in a ordered ($\mu < \mu_{\mathrm{c}}$) or disordered ($\mu > \mu_{\mathrm{c}}$) phase, respectively.

Specifically, we make use of the following ramp

$$\mu(t) = \frac{A}{(t-B)^2} - \frac{A}{(t-C)^2} + \mu_{\mathrm{c}}, \tag{C.29}$$

where A, B, and C are tunable parameters. One particularly successful choice was found to be $A = \mp 40$, when ramping from $|0\rangle$ or $|\mathbb{Z}_2\rangle$, respectively, $B = 30$, and $C = -0.1$. An example of this ramping curve is plotted in the inset of Fig. C.8(b). We include μ_{c} due to the need for a much slower ramp as the gap between the ground state and

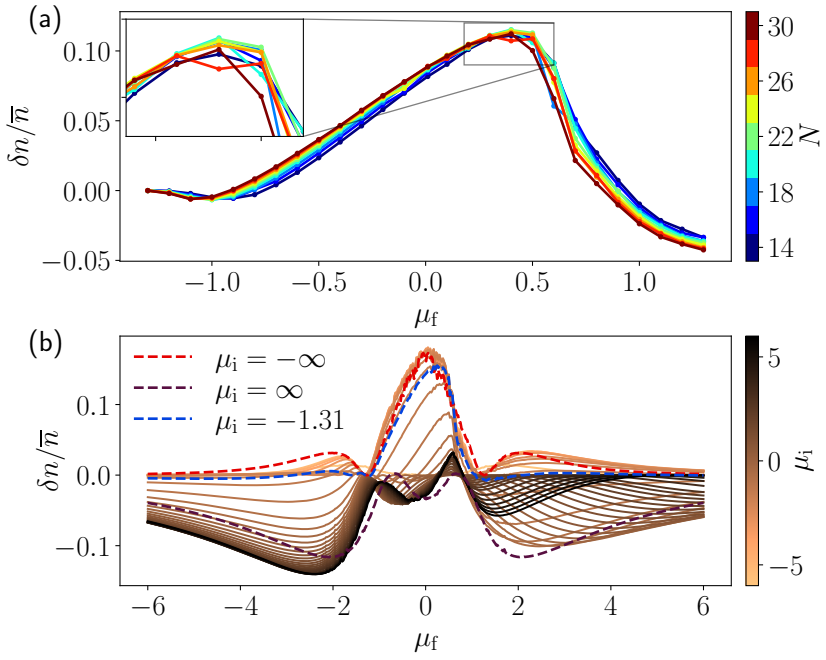

Figure C.7: Scaled difference of the expectation values between the diagonal and canonical ensembles. (a) For $\mu_i = \mu_c = -1.31$, there is a large difference around $\mu_f = 0.5$ that does not vary much with system size. Notably, we also see that to the left of that point the difference between the ensembles increases with system size. (b) Cross cuts through the phase diagram with a fixed value of μ_i indicated on the colour bar. The middle peak corresponds to region (1), while the two negative peaks on the bottom right correspond to regions (2) and (3), from left to right respectively. Data is obtained by exact diagonalisation for system size $N = 26$ with PBCs.

first excited state closes in the vicinity of the EPT point. After specifying the ramp and the initial state, we evolve by the PXP Hamiltonian in the presence of chemical potential, Eq. (C.29), until some time t. The evolution time is determined by numerically minimising $1 - |\langle\psi(t)|\mathrm{GS}(\mu_{\mathrm{target}})\rangle|^2$, where $|\mathrm{GS}(\mu_{\mathrm{target}})\rangle$ is the state we are trying to prepare.

Fig. C.8(a) illustrates the success of the ramping procedure. For system sizes ranging from $N = 6$ to $N = 14$, we have ramped to prepare the ground states from $\mu = \pm 6$, in increments $\delta\mu = 0.5$, towards the critical point, $\mu_c = -1.31$. Fig. C.8(b) shows the time that the ramp took for each ground state. We see the ramp time is insensitive to system size in gapped regions of the phase diagram, while it sharply increases near μ_c and exhibits strong fluctuations with N. For fixed ramp parameters, we expect it will take an infinite amount of time to prepare the critical ground state in the $N \to \infty$ limit.

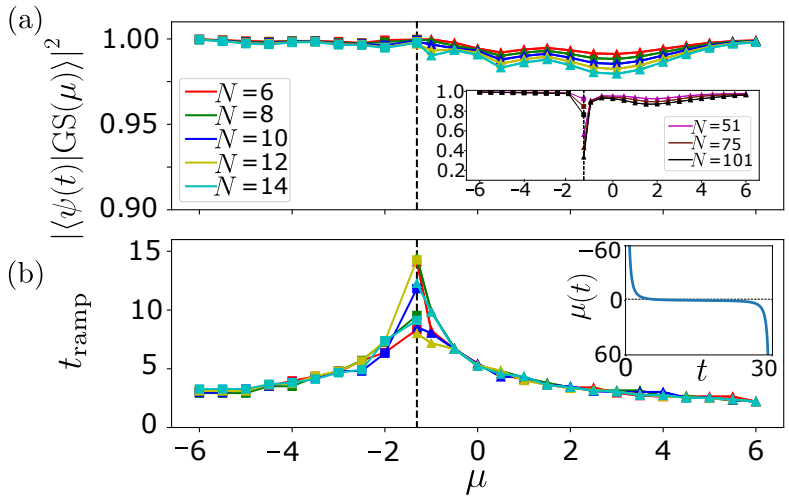

Figure C.8: (a) The success of preparing the PXP ground state at chemical potential μ by ramping the chemical potential according to Eq. (C.29). The total ramp time is varied for each point to maximise the overlap, which is plotted on the y-axis. For $\mu > \mu_c$, the initial state is $|0\rangle$ (square symbols), while for $\mu < \mu_c$ we start the ramp in the $|\mathbb{Z}_2\rangle$ state (triangles). Separate optimisations were performed for different system sizes N, shown in the same plot. Black dashed line (in all the panels) denotes the critical point μ_c. Inset: using the optimal parameters and average ramping time determined in smaller sizes in the main panel, we prepare the ground states for the same values of μ in much larger system sizes $N = 51, 75, 101$. The preparation in this case was done using the MPS method with time step $\delta t = 0.025$ and maximum bond dimension $\chi = 128$. While in the gapped phases the preparation remains successful, there is a visible drop near the critical point. (b) Total ramp time t_{ramp} returned by the optimisations in the main panel (a). Inset shows the ramping curve $\mu(t)$ in Eq. (C.29). We observe an increase of the ramp time and strong finite-size fluctuations at the critical point. The data in the main panels (a) and (b) was computed using exact diagonalisation in k=0 momentum and p=+1 inversion symmetry sector with PBCs.

Finally, to verify our preparation scheme in large systems, we repeated the preparation of the detuned PXP ground states for system sizes of $N = 51, 75$ and 101 using MPS simulations with bond dimension $\chi = 128$ and the the ramping protocol in Eq. (C.29), with the same A, B, C parameters. The inset of Fig. C.8(a) demonstrates that the ramping continues to successfully reproduce the desired ground state with high fidelity, with the exception of the critical point where we see a clear drop in overlap with the target state. This suggests the ramping procedure is a viable method for generating desired ground states even in large systems. With this in hand, along with the already existing capabilities to quench with a detuned PXP Hamiltonian and conduct measurements of local observables [16, 17], all the tools are, in principle, available to reconstruct the dynamical phase diagram in Fig. 4.4. In particular, local fidelity measurements [27] can

be used to approximate the numerically computed global fidelity in Fig. 4.4(a). This would allow to experimentally verify the persistence of QMBS across the phase diagram and its robustness near the critical point.

Appendix D

Further details on Gaussification in the Rydberg model

D.1 Motivating the choice of operators in the Wick decomposition

We motivate the choice of $\hat{A}$, $\hat{B}$, $\hat{C}$, $\hat{D}$ in Eq. (5.4), which yielded results qualitatively similar to the interaction distance across the three phases of the diagram. These operators must be single-site fermionic to provide a valid four-point Wick's decomposition. In order to express these operators in terms of Pauli matrices, we employ the Jordan-Wigner transformation. This allows us to reinterpret the fermionic creation and annihilation operators at site j as spin-raising and lowering operators, multiplied by the string $\prod_{k<j} \sigma_k^z$. This ensures the fermionic commutation relationship still holds.

We conducted an exhaustive search to verify Wick's decomposition in the UV model in Eq. (5.1), specifically where the Wick value in the $\mathbb{Z}_3$ state exceeds that in $\mathbb{Z}_2$ state. Interestingly, no two-point Pauli correlations that can indicate Gaussianity in the model were found. This unique feature arises from the Rydberg blockade mechanism, setting it apart from other models, such as the $\mathbb{Z}_2$ phases in the transverse field Ising model.

However, several Wick's decompositions involving 3-point local Pauli decompositions successfully quantify Gaussianity. We discuss a specific choice here: $\hat{A} = f_1^\dagger$, $\hat{B} = f_1$, $\hat{C} = f_2^\dagger$, $\hat{D} = f_3$. The left-hand side of Eq. (5.4), $\langle n_1 \sigma_2^+ \sigma_3^- \rangle$, invariably vanishes for the model due to the Rydberg blockade in the case of $\mathbb{Z}_2$ and due to the action of σ_3^- on the spin-down state in the $\mathbb{Z}_3$ regime. Thus the difference in Gaussianity originates from the right-hand side. To further exemplify and understand this, take both the GHZ state, $|\mathrm{GHZ}\rangle = (|000\rangle + |111\rangle)/\sqrt{2}$, (which is a macroscopic superposition like $|\mathbb{Z}_2\rangle$) and the W state, $|\mathrm{W}\rangle = (|100\rangle + |010\rangle + |001\rangle)/\sqrt{3}$ (similar to $|\mathbb{Z}_3\rangle$) for $N = 3$.

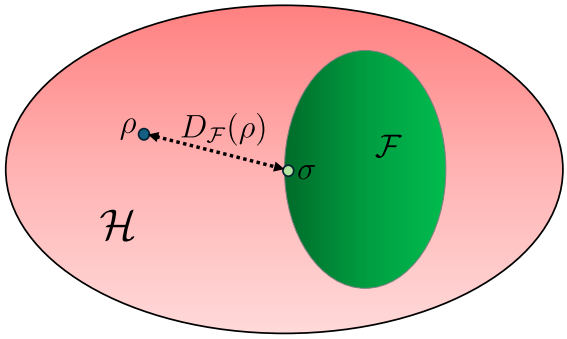

Figure D.1: An illustration of the definition of the interaction distance, $D_{\mathcal{F}}(\rho)$ of a density matrix ρ. The full Hilbert space, $\mathcal{H}$, is coloured in red while the subset of free density matrices, $\mathcal{F}$, is coloured in green. The interaction distance locates the closest free density matrix σ to quantify the interactions of ρ. Reproduced from Ref. [246].

For both states, due to the definition of the spin ladder operators and the form of the superpositions, $\langle n_1\sigma_2^+\sigma_3^-\rangle$ and $\langle\sigma_1^+\sigma_2^+\rangle\langle\sigma_1^-\sigma_2^z\sigma_3^-\rangle$ are zero. This leaves the $\langle n_1\rangle\langle\sigma_2^+\sigma_3^-\rangle$ and $\langle\sigma_1^-\sigma_2^+\rangle\langle\sigma_1^+\sigma_2^z\sigma_3^-\rangle$ components which consist of simple particle hopping terms (with no n_1 constraint unlike in $\langle n_1\sigma_2^+\sigma_3^-\rangle$). Both of these terms are still found to be 0 in the case of GHZ but non-zero in the W-state due to the fact that we can change from one translated pair to another by simply flipping two spins – something not possible in the GHZ state due to the macroscopic superposition. This natural distinction between the GHZ and W-state due to simple particle hopping motivates this choice of $\hat{A}$-$\hat{D}$ for these states. Recomputing the diagram using purely these two distinguishing hopping terms yields a result that qualitatively matches the interaction distance diagram in Fig. 5.2.

D.2 Further background on the interaction distance

In Section. 5.4.1, we made use of the interaction distance to provide a complementary measure of Gaussianity. In this section, we supplement this by providing a more detailed background of the interaction distance as a novel measurement. The interaction distance, $D_{\mathcal{F}}(\rho)$ in Eq. (5.6), is a tool that allows one to quantify the "freedom" of a quantum many-body state by simply analysing its entanglement structure. By doing so, it has found success in several models like the Ising chain or String-Net models [242, 246, 247]. This is done by comparing the entanglement spectrum with the nearest free entanglement spectrum in the Hilbert space through a variational algorithm.

The interaction distance of a density matrix, ρ, is more rigorously is defined as

$$D_{\mathcal{F}}(\rho) = \min_{\sigma\in\mathcal{F}} D(\rho,\sigma) = \min_{\sigma\in\mathcal{F}} \frac{1}{2}\,\mathrm{tr}\sqrt{(\rho-\sigma)^2} \tag{D.1}$$

where $\mathcal{F}$ denotes the manifold of free density matrices. This equation is diagrammatically illustrated in Fig. D.1. That is to say, the interaction distance is the shortest distance of ρ from $\mathcal{F}$.

This eventually breaks down to that of Eq. (5.6) as the manifold F can be quantified in terms of the entanglement of the reduced density matrices. It was shown in Ref. [248] that the spectrum of eigenvalues of the reduced density matrix encapsulates more complete information about the system and its interactions than the von Neumann entropy. This spectrum is defined as $\epsilon_k = -\ln \rho_k$ where ρ_k are the eigenvalues (or Schmidt values) of ρ. Within this entanglement Hilbert space defined by the entanglement spectrum, there is then a manifold containing the density matrices that arise from taking the subsystem of a free-fermion system. For a more detailed overview, and for access to the variational software used, see Ref. [246].

The interaction distance exhibits several useful properties, one of which is that $0 < D_{\mathcal{F}} < 3 - 2\sqrt{2}$ [247]. The saturation of this bound allows one to quantify a "maximally interacting" state in contrast to a free state (when $D_{\mathcal{F}} = 0$). Interestingly, it also obeys finite size scaling around critical points much like local observables are expected to around second-order phase transitions [242]. The interaction distance also captures non-perturbative effects in the system as it allows one to define the effective description of a system in terms of non-linear functions of original modes.

Bibliography

[1] J. M. Deutsch. Quantum statistical mechanics in a closed system. *Phys. Rev. A*, 43:2046, Feb 1991.

[2] Mark Srednicki. Chaos and quantum thermalization. *Phys. Rev. E*, 50:888, Aug 1994.

[3] Rahul Nandkishore and David A. Huse. Many-body localization and thermalization in quantum statistical mechanics. *Annual Review of Condensed Matter Physics*, 6(1):15–38, 2015.

[4] Christian Gogolin and Jens Eisert. Equilibration, thermalisation, and the emergence of statistical mechanics in closed quantum systems. *Rep. Prog. Phys.*, 79(5):056001, apr 2016.

[5] Takashi Mori, Tatsuhiko N Ikeda, Eriko Kaminishi, and Masahito Ueda. Thermalization and prethermalization in isolated quantum systems: a theoretical overview. *Journal of Physics B: Atomic, Molecular and Optical Physics*, 51(11):112001, may 2018.

[6] S. W. Hawking. Particle Creation by Black Holes. *Advanced Series in Astrophysics and Cosmology*, 8:85–106, June 1993.

[7] Robert M. Wald. The thermodynamics of black holes. *Living Reviews in Relativity*, 4(1), July 2001.

[8] A. I. Larkin and Yu. N. Ovchinnikov. Quasiclassical method in the theory of superconductivity. *SOVIET PHYSICS JETP*, 28:1200, 1969.

[9] Stephen H. Shenker and Douglas Stanford. Black holes and the butterfly effect. *Journal of High Energy Physics*, 2014(3), March 2014.

[10] A. Kitaev. Fundamental physics prize symposium, 2014.

[11] Juan Maldacena, Stephen H. Shenker, and Douglas Stanford. A bound on chaos. *Journal of High Energy Physics*, 2016(8):106, Aug 2016.

[12] Matthew D. Horner, Andrew Hallam, and Jiannis K. Pachos. Chiral spin-chain interfaces exhibiting event-horizon physics. *Phys. Rev. Lett.*, 130:016701, Jan 2023.

[13] Ewan Forbes, Matthew D. Horner, Andrew Hallam, Joseph Barker, and Jiannis K. Pachos. Exploring interacting chiral spin chains in terms of black hole physics. *Phys. Rev. B*, 108:245142, Dec 2023.

[14] Patrick Hayden and John Preskill. Black holes as mirrors: quantum information in random subsystems. *Journal of High Energy Physics*, 2007(09):120–120, September 2007.

[15] Henning Labuhn, Daniel Barredo, Sylvain Ravets, Sylvain de Léséleuc, Tommaso Macrì, Thierry Lahaye, and Antoine Browaeys. Tunable two-dimensional arrays of single Rydberg atoms for realizing quantum Ising models. *Nature*, 534:667, Jun 2016.

[16] Hannes Bernien, Sylvain Schwartz, Alexander Keesling, Harry Levine, Ahmed Omran, Hannes Pichler, Soonwon Choi, Alexander S. Zibrov, Manuel Endres, Markus Greiner, Vladan Vuletić, and Mikhail D. Lukin. Probing many-body dynamics on a 51-atom quantum simulator. *Nature*, 551(7682):579–584, Nov 2017.

[17] D. Bluvstein, A. Omran, H. Levine, A. Keesling, G. Semeghini, S. Ebadi, T. T. Wang, A. A. Michailidis, N. Maskara, W. W. Ho, S. Choi, M. Serbyn, M. Greiner, V. Vuletić, and M. D. Lukin. Controlling quantum many-body dynamics in driven Rydberg atom arrays. *Science*, 371(6536):1355–1359, 2021.

[18] C. J. Turner, A. A. Michailidis, D. A. Abanin, M. Serbyn, and Z. Papic. Weak ergodicity breaking from quantum many-body scars. *Nat. Phys.*, 14:745, 2018.

[19] C. J. Turner, A. A. Michailidis, D. A. Abanin, M. Serbyn, and Z. Papić. Quantum scarred eigenstates in a Rydberg atom chain: Entanglement, breakdown of thermalization, and stability to perturbations. *Phys. Rev. B*, 98:155134, Oct 2018.

[20] Maksym Serbyn, Dmitry A Abanin, and Zlatko Papić. Quantum many-body scars and weak breaking of ergodicity. *Nature Physics*, 17(6):675–685, 2021.

[21] Zlatko Papić. *Weak Ergodicity Breaking Through the Lens of Quantum Entanglement*, pages 341–395. Springer International Publishing, Cham, 2022.

[22] Sanjay Moudgalya, B Andrei Bernevig, and Nicolas Regnault. Quantum many-body scars and Hilbert space fragmentation: a review of exact results. *Reports on Progress in Physics*, 85(8):086501, jul 2022.

[23] Soonwon Choi, Christopher J. Turner, Hannes Pichler, Wen Wei Ho, Alexios A. Michailidis, Zlatko Papić, Maksym Serbyn, Mikhail D. Lukin, and Dmitry A. Abanin. Emergent su(2) dynamics and perfect quantum many-body scars. *Phys. Rev. Lett.*, 122:220603, Jun 2019.

[24] Kieran Bull, Jean-Yves Desaules, and Zlatko Papić. Quantum scars as embeddings of weakly broken Lie algebra representations. *Phys. Rev. B*, 101:165139, Apr 2020.

[25] Eric J. Heller. Bound-state eigenfunctions of classically chaotic Hamiltonian systems: Scars of periodic orbits. *Phys. Rev. Lett.*, 53:1515–1518, Oct 1984.

[26] Paul Niklas Jepsen, Yoo Kyung 'Eunice' Lee, Hanzhen Lin, Ivana Dimitrova, Yair Margalit, Wen Wei Ho, and Wolfgang Ketterle. Long-lived phantom helix states in Heisenberg quantum magnets. *Nature Physics*, 18(8):899–904, Aug 2022.

[27] Guo-Xian Su, Hui Sun, Ana Hudomal, Jean-Yves Desaules, Zhao-Yu Zhou, Bing Yang, Jad C. Halimeh, Zhen-Sheng Yuan, Zlatko Papić, and Jian-Wei Pan. Observation of many-body scarring in a Bose-Hubbard quantum simulator. *Phys. Rev. Res.*, 5:023010, Apr 2023.

[28] Pengfei Zhang, Hang Dong, Yu Gao, Liangtian Zhao, Jie Hao, Jean-Yves Desaules, Qiujiang Guo, Jiachen Chen, Jinfeng Deng, Bobo Liu, Wenhui Ren, Yunyan Yao, Xu Zhang, Shibo Xu, Ke Wang, Feitong Jin, Xuhao Zhu, Bing Zhang, Hekang Li, Chao Song, Zhen Wang, Fangli Liu, Zlatko Papić, Lei Ying, H. Wang, and Ying-Cheng Lai. Many-body Hilbert space scarring on a superconducting processor. *Nature Physics*, oct 2022.

[29] Zhiyuan Yao, Lei Pan, Shang Liu, and Hui Zhai. Quantum many-body scars and quantum criticality. *Phys. Rev. B*, 105:125123, Mar 2022.

[30] M. Gluza, C. Krumnow, M. Friesdorf, C. Gogolin, and J. Eisert. Equilibration via Gaussification in Fermionic Lattice Systems. *Phys. Rev. Lett.*, 117:190602, Nov 2016.

[31] Aydin Deger, Aiden Daniel, Zlatko Papić, and Jiannis K. Pachos. Persistent non-gaussian correlations in out-of-equilibrium rydberg atom arrays. *PRX Quantum*, 4(4), December 2023.

[32] Federico Carollo. Non-Gaussian dynamics of quantum fluctuations and mean-field limit in open quantum central spin systems, 2023.

[33] Samuel L. Braunstein and Peter van Loock. Quantum information with continuous variables. *Rev. Mod. Phys.*, 77:513–577, Jun 2005.

[34] Daniel E. Browne, Jens Eisert, Stefan Scheel, and Martin B. Plenio. Driving non-Gaussian to Gaussian states with linear optics. *Phys. Rev. A*, 67:062320, Jun 2003.

[35] Nicolas C. Menicucci, Peter van Loock, Mile Gu, Christian Weedbrook, Timothy C. Ralph, and Michael A. Nielsen. Universal quantum computation with continuous-variable cluster states. *Phys. Rev. Lett.*, 97:110501, Sep 2006.

[36] J. Heersink, Ch. Marquardt, R. Dong, R. Filip, S. Lorenz, G. Leuchs, and U. L. Andersen. Distillation of squeezing from non-gaussian quantum states. *Phys. Rev. Lett.*, 96:253601, Jun 2006.

[37] Julien Niset, Jaromír Fiurášek, and Nicolas J. Cerf. No-Go Theorem for Gaussian Quantum Error Correction. *Phys. Rev. Lett.*, 102:120501, Mar 2009.

[38] R. M. Gomes, A. Salles, F. Toscano, P. H. Souto Ribeiro, and S. P. Walborn. Quantum entanglement beyond Gaussian criteria. *Proceedings of the National Academy of Sciences*, 106(51):21517–21520, 2022/12/27 2009.

[39] A. Mari and J. Eisert. Positive Wigner Functions Render Classical Simulation of Quantum Computation Efficient. *Phys. Rev. Lett.*, 109:230503, Dec 2012.

[40] Mattia Walschaers, Claude Fabre, Valentina Parigi, and Nicolas Treps. Entanglement and Wigner Function Negativity of Multimode Non-Gaussian States. *Phys. Rev. Lett.*, 119:183601, Oct 2017.

[41] Daiqin Su, Casey R. Myers, and Krishna Kumar Sabapathy. Conversion of Gaussian states to non-Gaussian states using photon-number-resolving detectors. *Phys. Rev. A*, 100:052301, Nov 2019.

[42] Young-Sik Ra, Adrien Dufour, Mattia Walschaers, Clément Jacquard, Thibault Michel, Claude Fabre, and Nicolas Treps. Non-Gaussian quantum states of a multimode light field. *Nature Physics*, 16(2):144–147, 2020.

[43] Mattia Walschaers. Non-Gaussian Quantum States and Where to Find Them. *PRX Quantum*, 2:030204, Sep 2021.

[44] M. Hebenstreit, R. Jozsa, B. Kraus, S. Strelchuk, and M. Yoganathan. All Pure Fermionic Non-Gaussian States Are Magic States for Matchgate Computations. *Phys. Rev. Lett.*, 123:080503, Aug 2019.

[45] Jitendra K. Verma, Lukáš Lachman, and Radim Filip. Direct detection of quantum non-Gaussian light from a dispersively coupled single atom. *Quantum*, 6:660, February 2022.

[46] Alexander Keesling, Ahmed Omran, Harry Levine, Hannes Bernien, Hannes Pichler, Soonwon Choi, Rhine Samajdar, Sylvain Schwartz, Pietro Silvi, Subir Sachdev, Peter Zoller, Manuel Endres, Markus Greiner, Vladan Vuletić, and Mikhail D. Lukin. Quantum Kibble–Zurek mechanism and critical dynamics on a programmable Rydberg simulator. *Nature*, 568(7751):207–211, 2019.

[47] A. Omran, H. Levine, A. Keesling, G. Semeghini, T. T. Wang, S. Ebadi, H. Bernien, A. S. Zibrov, H. Pichler, S. Choi, J. Cui, M. Rossignolo, P. Rembold, S. Montangero, T. Calarco, M. Endres, M. Greiner, V. Vuletić , and M. D. Lukin. Generation and manipulation of Schrödinger cat states in Rydberg atom arrays. *Science*, 365(6453):570–574, aug 2019.

[48] Subir Sachdev and Jinwu Ye. Gapless spin-fluid ground state in a random quantum Heisenberg magnet. *Phys. Rev. Lett.*, 70:3339–3342, May 1993.

[49] Juan Maldacena and Douglas Stanford. Remarks on the Sachdev-Ye-Kitaev model. *Phys. Rev. D*, 94:106002, Nov 2016.

[50] A Kitaev. A simple model of quantum holography, talk at KITP. *University of California, Santa Barbara USA*, 7, 2015.

[51] Alexei Kitaev and S. Josephine Suh. The soft mode in the Sachdev-Ye-Kitaev model and its gravity dual. *Journal of High Energy Physics*, 2018(5), May 2018.

[52] Joseph Polchinski and Vladimir Rosenhaus. The spectrum in the Sachdev-Ye-Kitaev model. *Journal of High Energy Physics*, 2016(4):1–25, April 2016.

[53] Wenbo Fu and Subir Sachdev. Numerical study of fermion and boson models with infinite-range random interactions. *Phys. Rev. B*, 94:035135, Jul 2016.

[54] Anushya Chandran, Thomas Iadecola, Vedika Khemani, and Roderich Moessner. Quantum Many-Body Scars: A Quasiparticle Perspective. *Annual Review of Condensed Matter Physics*, 14(1):443–469, mar 2023.

[55] L. Landau and E. Lifshitz. *Statistical Physics*, volume 5. Eslsevier Science, 2013.

[56] H Muller-kirsten. *Basics Of Statistical Physics*. World Scientific Publishing Company, second edition, 2013.

[57] Luca D'Alessio, Yariv Kafri, Anatoli Polkovnikov, and Marcos Rigol. From quantum chaos and eigenstate thermalization to statistical mechanics and thermodynamics. *Advances in Physics*, 65(3):239–362, May 2016.

[58] B. Sutherland. *Beautiful Models: 70 Years of Exactly Solved Quantum Many-body Problems*. World Scientific, 2004.

[59] Dmitry A. Abanin, Ehud Altman, Immanuel Bloch, and Maksym Serbyn. Colloquium: Many-body localization, thermalization, and entanglement. *Rev. Mod. Phys.*, 91:021001, May 2019.

[60] Madan Lal Mehta. *Random matrices*, volume 142. Elsevier, 2004.

[61] O. Bohigas, M. J. Giannoni, and C. Schmit. Characterization of chaotic quantum spectra and universality of level fluctuation laws. *Phys. Rev. Lett.*, 52:1–4, Jan 1984.

[62] Eugene P. Wigner. On the distribution of the roots of certain symmetric matrices. *Annals of Mathematics*, 67(2):325–327, 1958.

[63] Freeman J. Dyson. A Brownian-Motion Model for the Eigenvalues of a Random Matrix. *Journal of Mathemetical Physics*, 3:1191—-1198, 1962.

[64] Vadim Oganesyan and David A. Huse. Localization of interacting fermions at high temperature. *Phys. Rev. B*, 75:155111, Apr 2007.

[65] Y. Y. Atas, E. Bogomolny, O. Giraud, and G. Roux. Distribution of the Ratio of Consecutive Level Spacings in Random Matrix Ensembles. *Phys. Rev. Lett.*, 110:084101, Feb 2013.

[66] A. M. Lyapunov. Ausgewählte Abhandlungen. Redaktion von V. I. Smirnov. Kommentare von S. N. Bernstejn, L. N. Sretenskij und N. G. Cetaev. (Akademie der Wissenschaften der UdSSR, Klassiker der Wissenschaft) Moskau: Verlag der Akademie der Wissenschaften der UdSSR. 540 S. (1948)., 1948.

[67] A. M. Lyapunov. Lectures on theoretical mechanics. Akademiya Nauk Ukrainskoĭ SSR. Institut Matematiki. Kiev: "Naukova Dumka". 632 p. R. 5.40 (1982)., 1982.

[68] Stephen H. Shenker and Douglas Stanford. Stringy effects in scrambling, 2015.

[69] Pavan Hosur, Xiao-Liang Qi, Daniel A. Roberts, and Beni Yoshida. Chaos in quantum channels. *Journal of High Energy Physics*, 2016(2), February 2016.

[70] Yasuhiro Sekino and L. Susskind. Fast scramblers. *Journal of High Energy Physics*, 2008(10):065, oct 2008.

[71] Yunxiang Liao and Victor Galitski. Nonlinear sigma model approach to many-body quantum chaos: Regularized and unregularized out-of-time-ordered correlators. *Phys. Rev. B*, 98:205124, Nov 2018.

[72] R J Lewis-Swan, A Safavi-Naini, J J Bollinger, and A M Rey. Unifying scrambling, thermalization and entanglement through measurement of fidelity out-of-time-order correlators in the dicke model. *Nature Communications*, 10(1):1581, April 2019.

[73] Bryce Kobrin, Zhenbin Yang, Gregory D. Kahanamoku-Meyer, Christopher T. Olund, Joel E. Moore, Douglas Stanford, and Norman Y. Yao. Many-Body Chaos in the Sachdev-Ye-Kitaev Model. *Physical Review Letters*, 126(3), January 2021.

[74] Kristan Jensen. Chaos in AdS_2 Holography. *Phys. Rev. Lett.*, 117:111601, Sep 2016.

[75] Julius Engelsöy, Thomas G. Mertens, and Herman Verlinde. An investigation of AdS2 backreaction and holography. *Journal of High Energy Physics*, 2016(7), July 2016.

[76] Juan Maldacena, Douglas Stanford, and Zhenbin Yang. Conformal symmetry and its breaking in two-dimensional nearly anti-de Sitter space. *Progress of Theoretical and Experimental Physics*, 2016(12):12C104, 11 2016.

[77] Daniel Jafferis, Alexander Zlokapa, Jose Lykken, David K Kolchmeyer, Samantha I Davis, Nikolai Lauk, Hartmut Neven, and Maria Spiropulu. Traversable wormhole dynamics on a quantum processor. *Nature*, 612(7938):51–55, December 2022.

[78] Patrick W O'Connor and Eric J Heller. Quantum localization for a strongly classically chaotic system. *Phys. Rev. Lett.*, 61(20):2288–2291, November 1988.

[79] Sanjay Moudgalya, Nicolas Regnault, and B. Andrei Bernevig. Entanglement of exact excited states of Affleck-Kennedy-Lieb-Tasaki models: Exact results, many-body scars, and violation of the strong eigenstate thermalization hypothesis. *Phys. Rev. B*, 98:235156, Dec 2018.

[80] Daniel K. Mark, Cheng-Ju Lin, and Olexei I. Motrunich. Unified structure for exact towers of scar states in the Affleck-Kennedy-Lieb-Tasaki and other models. *Phys. Rev. B*, 101:195131, May 2020.

[81] Berislav Buča, Joseph Tindall, and Dieter Jaksch. Non-stationary coherent quantum many-body dynamics through dissipation. *Nature Communications*, 10(1):1730, Apr 2019.

[82] Marko Medenjak, Berislav Buča, and Dieter Jaksch. Isolated Heisenberg magnet as a quantum time crystal. *Phys. Rev. B*, 102:041117(R), Jul 2020.

[83] Sanjay Moudgalya, Abhinav Prem, Rahul Nandkishore, Nicolas Regnault, and B Andrei Bernevig. Thermalization and its absence within Krylov subspaces of a constrained Hamiltonian. *arXiv e-prints*, Oct 2019.

[84] Naoto Shiraishi and Takashi Mori. Systematic construction of counterexamples to the eigenstate thermalization hypothesis. *Phys. Rev. Lett.*, 119:030601, Jul 2017.

[85] Michael Schecter and Thomas Iadecola. Weak ergodicity breaking and quantum many-body scars in spin-1 XY magnets. *Phys. Rev. Lett.*, 123:147201, Oct 2019.

[86] Sanjay Moudgalya, B. Andrei Bernevig, and Nicolas Regnault. Quantum many-body scars in a Landau level on a thin torus. *Phys. Rev. B*, 102:195150, Nov 2020.

[87] Seulgi Ok, Kenny Choo, Christopher Mudry, Claudio Castelnovo, Claudio Chamon, and Titus Neupert. Topological many-body scar states in dimensions one, two, and three. *Phys. Rev. Research*, 1:033144, Dec 2019.

[88] Kieran Bull, Ivar Martin, and Z. Papić. Systematic construction of scarred many-body dynamics in 1D lattice models. *Phys. Rev. Lett.*, 123:030601, Jul 2019.

[89] Ana Hudomal, Ivana Vasić, Nicolas Regnault, and Zlatko Papić. Quantum scars of bosons with correlated hopping. *Communications Physics*, 3(1):99, Jun 2020.

[90] Hongzheng Zhao, Joseph Vovrosh, Florian Mintert, and Johannes Knolle. Quantum many-body scars in optical lattices. *Phys. Rev. Lett.*, 124:160604, Apr 2020.

[91] Naoyuki Shibata, Nobuyuki Yoshioka, and Hosho Katsura. Onsager's scars in disordered spin chains. *Phys. Rev. Lett.*, 124:180604, May 2020.

[92] Nicholas O'Dea, Fiona Burnell, Anushya Chandran, and Vedika Khemani. From tunnels to towers: Quantum scars from Lie algebras and q-deformed Lie algebras. *Phys. Rev. Research*, 2:043305, Dec 2020.

[93] Sanjay Moudgalya, Edward O'Brien, B. Andrei Bernevig, Paul Fendley, and Nicolas Regnault. Large classes of quantum scarred Hamiltonians from matrix product states. *Phys. Rev. B*, 102:085120, Aug 2020.

[94] Jean-Yves Desaules, Ana Hudomal, Christopher J. Turner, and Zlatko Papić. Proposal for realizing quantum scars in the tilted 1D Fermi-Hubbard model. *Phys. Rev. Lett.*, 126:210601, May 2021.

[95] Jean-Yves Desaules, Ana Hudomal, Debasish Banerjee, Arnab Sen, Zlatko Papić, and Jad C. Halimeh. Prominent quantum many-body scars in a truncated Schwinger model. *Phys. Rev. B*, 107:205112, May 2023.

[96] Jean-Yves Desaules, Debasish Banerjee, Ana Hudomal, Zlatko Papić, Arnab Sen, and Jad C. Halimeh. Weak ergodicity breaking in the Schwinger model. *Phys. Rev. B*, 107:L201105, May 2023.

[97] Jean-Yves Desaules, Kieran Bull, Aiden Daniel, and Zlatko Papić. Hypergrid subgraphs and the origin of scarred quantum walks in many-body Hilbert space. *Phys. Rev. B*, 105:245137, Jun 2022.

[98] Christopher M. Langlett, Zhi-Cheng Yang, Julia Wildeboer, Alexey V. Gorshkov, Thomas Iadecola, and Shenglong Xu. Rainbow scars: From area to volume law. *Phys. Rev. B*, 105:L060301, Feb 2022.

[99] S M Morsink and R B Mann. Black hole radiation of Dirac particles in 1+1 dimensions. *Classical and Quantum Gravity*, 8(12):2257, dec 1991.

[100] Charles H. Bennett, Gilles Brassard, Claude Crépeau, Richard Jozsa, Asher Peres, and William K. Wootters. Teleporting an unknown quantum state via dual classical and einstein-podolsky-rosen channels. *Phys. Rev. Lett.*, 70:1895–1899, Mar 1993.

[101] Dik Bouwmeester, Jian-Wei Pan, Klaus Mattle, Manfred Eibl, Harald Weinfurter, and Anton Zeilinger. Experimental quantum teleportation. *Nature*, 390(6660):575–579, December 1997.

[102] D. Boschi, S. Branca, F. De Martini, L. Hardy, and S. Popescu. Experimental realization of teleporting an unknown pure quantum state via dual classical and einstein-podolsky-rosen channels. *Phys. Rev. Lett.*, 80:1121–1125, Feb 1998.

[103] Beni Yoshida and Alexei Kitaev. Efficient decoding for the hayden-preskill protocol, 2017.

[104] Beni Yoshida and Norman Y. Yao. Disentangling scrambling and decoherence via quantum teleportation. *Phys. Rev. X*, 9:011006, Jan 2019.

[105] K. A. Landsman, C. Figgatt, T. Schuster, N. M. Linke, B. Yoshida, N. Y. Yao, and C. Monroe. Verified quantum information scrambling. *Nature*, 567(7746):61–65, March 2019.

[106] Sepehr Nezami, Henry W. Lin, Adam R. Brown, Hrant Gharibyan, Stefan Leichenauer, Grant Salton, Leonard Susskind, Brian Swingle, and Michael Walter. Quantum Gravity in the Lab. II. Teleportation by Size and Traversable Wormholes. *PRX Quantum*, 4:010321, Feb 2023.

[107] Adam R. Brown, Hrant Gharibyan, Stefan Leichenauer, Henry W. Lin, Sepehr Nezami, Grant Salton, Leonard Susskind, Brian Swingle, and Michael Walter. Quantum gravity in the lab. i. teleportation by size and traversable wormholes. *PRX Quantum*, 4:010320, Feb 2023.

[108] Christian D'Cruz and Jiannis K. Pachos. Chiral phase from three-spin interactions in an optical lattice. *Physical Review A*, 72(4), October 2005.

[109] Dimitris I. Tsomokos, Juan José García-Ripoll, Nigel R. Cooper, and Jiannis K. Pachos. Chiral entanglement in triangular lattice models. *Physical Review A*, 77(1), January 2008.

[110] T. Giamarchi. *Quantum Physics in One Dimension*. Oxford University Press, 2003.

[111] E. Miranda. Introduction to Bosonization. *Brazilian Journal of Physics*, 33(1), March 2002.

[112] Sreemayee Aditya and Diptiman Sen. Bosonization study of a generalized statistics model with four fermi points. *Phys. Rev. B*, 103:235162, Jun 2021.

[113] Grigory E. Volovik. *The Universe in a Helium Droplet*. Oxford University Press, 02 2009.

[114] G.E. Volovik and K. Zhang. Lifshitz Transitions, Type-II Dirac and Weyl Fermions, Event Horizon and All That. *J. Low Temp. Phys.*, 189:276–299, Oct 2017.

[115] G.E. Volovik and P. Huhtala. Fermionic microstates within the Painlevé-Gullstrand black hole. *J. Exp. Theor. Phys.*, 94:853–861, May 2002.

[116] G.E. Volovik. Black hole and Hawking radiation by type-II Weyl fermions. *Jetp Lett.*, 104:645–648, Nov 2016.

[117] Christophe De Beule, Solofo Groenendijk, Tobias Meng, and Thomas L. Schmidt. Artificial event horizons in Weyl semimetal heterostructures and their non-equilibrium signatures. *SciPost Phys.*, 11:095, 2021.

[118] Corentin Morice, Ali G. Moghaddam, Dmitry Chernyavsky, Jasper van Wezel, and Jeroen van den Brink. Synthetic gravitational horizons in low-dimensional quantum matter. *Phys. Rev. Res.*, 3:L022022, Jun 2021.

[119] Viktor Könye, Corentin Morice, Dmitry Chernyavsky, Ali G. Moghaddam, Jeroen van den Brink, and Jasper van Wezel. Horizon physics of quasi-one-dimensional tilted Weyl cones on a lattice. *Phys. Rev. Res.*, 4:033237, Sep 2022.

[120] Andreas Haller, Suraj Hegde, Chen Xu, Christophe De Beule, Thomas L. Schmidt, and Tobias Meng. Black hole mirages: Electron lensing and Berry curvature effects in inhomogeneously tilted Weyl semimetals. *SciPost Phys.*, 14:119, 2023.

[121] Maulik K. Parikh and Frank Wilczek. Hawking radiation as tunneling. *Phys. Rev. Lett.*, 85:5042–5045, Dec 2000.

[122] Run-Qiu Yang, Hui Liu, Shining Zhu, Le Luo, and Rong-Gen Cai. Simulating quantum field theory in curved spacetime with quantum many-body systems. *Phys. Rev. Research*, 2:023107, Apr 2020.

[123] Daniel Sabsovich, Paul Wunderlich, Victor Fleurov, Dmitry I. Pikulin, Roni Ilan, and Tobias Meng. Hawking fragmentation and Hawking attenuation in Weyl semimetals. *Phys. Rev. Research*, 4:013055, Jan 2022.

[124] Daan Maertens, Nick Bultinck, and Karel Van Acoleyen. Hawking radiation on the lattice from Floquet and local Hamiltonian quench dynamics. *Phys. Rev. B*, 109:014309, Jan 2024.

[125] Lotte Mertens, Ali G. Moghaddam, Dmitry Chernyavsky, Corentin Morice, Jeroen van den Brink, and Jasper van Wezel. Thermalization by a synthetic horizon. *Phys. Rev. Res.*, 4:043084, Nov 2022.

[126] Michael Stone. An analogue of Hawking radiation in the quantum Hall effect. *Classical and Quantum Gravity*, 30(8):085003, mar 2013.

[127] Jeff Steinhauer. Observation of quantum Hawking radiation and its entanglement in an analogue black hole. *Nature Physics*, 12(10):959–965, aug 2016.

[128] Arkadiusz Kosior, Maciej Lewenstein, and Alessio Celi. Unruh effect for interacting particles with ultracold atoms. *SciPost Phys.*, 5:61, 2018.

[129] A. Roldán-Molina, Alvaro S. Nunez, and R. A. Duine. Magnonic black holes. *Phys. Rev. Lett.*, 118:061301, Feb 2017.

[130] Javier Rodríguez-Laguna, Leticia Tarruell, Maciej Lewenstein, and Alessio Celi. Synthetic Unruh effect in cold atoms. *Phys. Rev. A*, 95:013627, Jan 2017.

[131] A. Retzker, J. I. Cirac, M. B. Plenio, and B. Reznik. Methods for Detecting Acceleration Radiation in a Bose-Einstein Condensate. *Phys. Rev. Lett.*, 101:110402, Sep 2008.

[132] Shan Guan, Zhi-Ming Yu, Ying Liu, Gui-Bin Liu, Liang Dong, Yunhao Lu, Yugui Yao, and Shengyuan A. Yang. Artificial gravity field, astrophysical analogues, and topological phase transitions in strained topological semimetals. *npj Quantum Materials*, 2(1):23, 2017.

[133] Hang Liu, Jia-Tao Sun, Chenchen Song, Huaqing Huang, Feng Liu, and Sheng Meng. Fermionic Analogue of High Temperature Hawking Radiation in Black Phosphorus. *Chinese Physics Letters*, 37(6):067101, 2020.

[134] Huaqing Huang, Kyung-Hwan Jin, and Feng Liu. Black-hole horizon in the Dirac semimetal $Zn_2In_2S_5$. *Phys. Rev. B*, 98:121110, Sep 2018.

[135] Jaewon Kim, Xiangyu Cao, and Ehud Altman. Scrambling versus relaxation in Fermi and non-Fermi liquids. *Physical Review B*, 102(8), August 2020.

[136] Nicolas Regnault and Rahul Nandkishore. Floquet thermalization: Symmetries and random matrix ensembles. *Phys. Rev. B*, 93:104203, Mar 2016.

[137] A. Hallam, J. G. Morley, and A. G. Green. The Lyapunov spectra of quantum thermalisation. *Nature Communications*, 10(1), June 2019.

[138] Étienne Lantagne-Hurtubise, Stephan Plugge, Oguzhan Can, and Marcel Franz. Diagnosing quantum chaos in many-body systems using entanglement as a resource. *Phys. Rev. Res.*, 2:013254, Mar 2020.

[139] Zehua Tian, Yiheng Lin, Uwe R. Fischer, and Jiangfeng Du. Testing the upper bound on the speed of scrambling with an analogue of Hawking radiation using trapped ions. *The European Physical Journal C*, 82(3), March 2022.

[140] W. G.. Baber. The contribution to the electrical resistance of metals from collisions between electrons. *Phys. Rev. X*, 1937.

[141] Zhi Wang, Meng Huang, Jianzhou Zhao, Cong Chen, Haoliang Huang, Xiangqi Wang, Ping Liu, Jianlin Wang, Junxiang Xiang, Chao Feng, Zengming Zhang, Xudong Cui, Yalin Lu, Shengyuan A. Yang, and Bin Xiang. Fermi liquid behavior and colossal magnetoresistance in layered $MoOCl_2$. *Phys. Rev. Mater.*, 4:041001, Apr 2020.

[142] Douglas Stanford. Many-body chaos at weak coupling. *Journal of High Energy Physics*, 2016(10), October 2016.

[143] Debanjan Chowdhury and Brian Swingle. Onset of many-body chaos in the $O(N)$ model. *Phys. Rev. D*, 96:065005, Sep 2017.

[144] Sumilan Banerjee and Ehud Altman. Solvable model for a dynamical quantum phase transition from fast to slow scrambling. *Physical Review B*, 95(13), April 2017.

[145] Ji-Gang Ren, Ping Xu, Hai-Lin Yong, Liang Zhang, Sheng-Kai Liao, Juan Yin, Wei-Yue Liu, Wen-Qi Cai, Meng Yang, Li Li, Kui-Xing Yang, Xuan Han, Yong-Qiang Yao, Ji Li, Hai-Yan Wu, Song Wan, Lei Liu, Ding-Quan Liu, Yao-Wu Kuang, Zhi-Ping He, Peng Shang, Cheng Guo, Ru-Hua Zheng, Kai Tian, Zhen-Cai Zhu, Nai-Le Liu, Chao-Yang Lu, Rong Shu, Yu-Ao Chen, Cheng-Zhi Peng, Jian-Yu Wang, and Jian-Wei Pan. Ground-to-satellite quantum teleportation. *Nature*, 549(7670):70–73, August 2017.

[146] Hiroki Takesue, Shellee D Dyer, Martin J Stevens, Varun Verma, Richard P Mirin, and Sae Woo Nam. Quantum teleportation over 100 km of fiber using highly efficient superconducting nanowire single-photon detectors. *Optica*, 2(10):832–835, 2015.

[147] Qi-Chao Sun, Yang-Fan Jiang, Ya-Li Mao, Li-Xing You, Wei Zhang, Wei-Jun Zhang, Xiao Jiang, Teng-Yun Chen, Hao Li, Yi-Dong Huang, et al. Entanglement swapping over 100 km optical fiber with independent entangled photon-pair sources. *Optica*, 4(10):1214–1218, 2017.

[148] Raju Valivarthi, Samantha I Davis, Cristián Peña, Si Xie, Nikolai Lauk, Lautaro Narváez, Jason P Allmaras, Andrew D Beyer, Yewon Gim, Meraj Hussein, et al. Teleportation systems toward a quantum internet. *PRX Quantum*, 1(2):020317, 2020.

[149] Xiao-Min Hu, Yu Guo, Bi-Heng Liu, Chuan-Feng Li, and Guang-Can Guo. Progress in quantum teleportation. *Nature Reviews Physics*, 5(6):339–353, 2023.

[150] Lakshya Agarwal, Christopher M. Langlett, and Shenglong Xu. Long-range bell states from local measurements and many-body teleportation without time reversal. *Physical Review Letters*, 130(2), January 2023.

[151] S. W. Hawking. Gravitational radiation from colliding black holes. *Phys. Rev. Lett.*, 26:1344–1346, May 1971.

[152] J D Bekenstein. Black holes and the second law. *Lettere al Nuovo Cimento (1971-1985)*, 4(15):737–740, August 1972.

[153] Jacob D. Bekenstein. Black holes and entropy. *Phys. Rev. D*, 7:2333–2346, Apr 1973.

[154] J M Bardeen, B Carter, and S W Hawking. The four laws of black hole mechanics. *Communications in Mathematical Physics*, 31(2):161–170, June 1973.

[155] Jacob D. Bekenstein. Generalized second law of thermodynamics in black-hole physics. *Phys. Rev. D*, 9:3292–3300, Jun 1974.

[156] S W Hawking. Black hole explosions? *Nature*, 248(5443):30–31, March 1974.

[157] S. W. Hawking. Black holes and thermodynamics. *Phys. Rev. D*, 13:191–197, Jan 1976.

[158] Rishabh Jha, Salvatore R. Manmana, and Stefan Kehrein. Page curve and entanglement dynamics in an interacting fermionic chain, 2025.

[159] A. Deger et al. XXXX.XXXXX. To appear shortly.

[160] Aiden Daniel, Tanmay Bhore, Jiannis K. Pachos, Chang Liu, and Andrew Hallam. Quantum teleportation between simulated binary black holes, 2025.

[161] Don N. Page. Average entropy of a subsystem. *Phys. Rev. Lett.*, 71:1291–1294, Aug 1993.

[162] Don N. Page. Is black-hole evaporation predictable? *Phys. Rev. Lett.*, 44:301–304, Feb 1980.

[163] Yoshifumi Nakata and Masaki Tezuka. Hayden-preskill recovery in hamiltonian systems. *Physical Review Research*, 6(2), April 2024.

[164] Joaquin F. Rodriguez-Nieva, Cheryne Jonay, and Vedika Khemani. Quantifying quantum chaos through microcanonical distributions of entanglement. *Phys. Rev. X*, 14:031014, Jul 2024.

[165] M. C. Bañuls, J. I. Cirac, and M. B. Hastings. Strong and weak thermalization of infinite nonintegrable quantum systems. *Phys. Rev. Lett.*, 106:050405, Feb 2011.

[166] Hyungwon Kim and David A. Huse. Ballistic spreading of entanglement in a diffusive nonintegrable system. *Phys. Rev. Lett.*, 111:127205, Sep 2013.

[167] Anna Keselman, Laimei Nie, and Erez Berg. Scrambling and Lyapunov exponent in spatially extended systems. *Phys. Rev. B*, 103:L121111, Mar 2021.

[168] P. Bocchieri and A. Loinger. Quantum recurrence theorem. *Phys. Rev.*, 107:337–338, Jul 1957.

[169] Ian C. Percival. Almost periodicity and the quantal h theorem. *Journal of Mathematical Physics*, 2(2):235–239, 1961.

[170] J. H. Eberly, N. B. Narozhny, and J. J. Sanchez-Mondragon. Periodic spontaneous collapse and revival in a simple quantum model. *Phys. Rev. Lett.*, 44:1323–1326, May 1980.

[171] Gerhard Rempe, Herbert Walther, and Norbert Klein. Observation of quantum collapse and revival in a one-atom maser. *Phys. Rev. Lett.*, 58:353–356, Jan 1987.

[172] John A. Yeazell, Mark Mallalieu, and C. R. Stroud. Observation of the collapse and revival of a Rydberg electronic wave packet. *Phys. Rev. Lett.*, 64:2007–2010, Apr 1990.

[173] T. Baumert, V. Engel, C. Röttgermann, W.T. Strunz, and G. Gerber. Femtosecond pump—probe study of the spreading and recurrence of a vibrational wave packet in Na_2. *Chemical Physics Letters*, 191(6):639 – 644, 1992.

[174] M. Brune, F. Schmidt-Kaler, A. Maali, J. Dreyer, E. Hagley, J. M. Raimond, and S. Haroche. Quantum Rabi oscillation: A direct test of field quantization in a cavity. *Phys. Rev. Lett.*, 76:1800–1803, Mar 1996.

[175] David L. Aronstein and C. R. Stroud. Fractional wave-function revivals in the infinite square well. *Phys. Rev. A*, 55:4526–4537, Jun 1997.

[176] R. W. Robinett and S. Heppelmann. Quantum wave-packet revivals in circular billiards. *Phys. Rev. A*, 65:062103, May 2002.

[177] Markus Greiner, Olaf Mandel, Theodor W. Hänsch, and Immanuel Bloch. Collapse and revival of the matter wave field of a Bose-Einstein condensate. *Nature*, 419(6902):51–54, 2002.

[178] Sebastian Will, Thorsten Best, Ulrich Schneider, Lucia Hackermüller, Dirk-Sören Lühmann, and Immanuel Bloch. Time-resolved observation of coherent multi-body interactions in quantum phase revivals. *Nature*, 465(7295):197–201, 2010.

[179] Thomas Schweigler, Valentin Kasper, Sebastian Erne, Igor Mazets, Bernhard Rauer, Federica Cataldini, Tim Langen, Thomas Gasenzer, Jürgen Berges, and Jörg Schmiedmayer. Experimental characterization of a quantum many-body system via higher-order correlations. *Nature*, 545(7654):323–326, 2017.

[180] Marc Dubois, Gautier Lefebvre, and Patrick Sebbah. Quantum revival for elastic waves in thin plate. *The European Physical Journal Special Topics*, 226(7):1593–1601, 2017.

[181] Bernhard Rauer, Sebastian Erne, Thomas Schweigler, Federica Cataldini, Mohammadamin Tajik, and Jörg Schmiedmayer. Recurrences in an isolated quantum many-body system. *Science*, 360(6386):307–310, 2018.

[182] Ana Hudomal, Jean-Yves Desaules, Bhaskar Mukherjee, Guo-Xian Su, Jad C. Halimeh, and Zlatko Papić. Driving quantum many-body scars in the PXP model. *Phys. Rev. B*, 106:104302, Sep 2022.

[183] Paul Fendley, K. Sengupta, and Subir Sachdev. Competing density-wave orders in a one-dimensional hard-boson model. *Phys. Rev. B*, 69:075106, Feb 2004.

[184] Igor Lesanovsky and Hosho Katsura. Interacting Fibonacci anyons in a Rydberg gas. *Phys. Rev. A*, 86:041601(R), Oct 2012.

[185] Adrian Feiguin, Simon Trebst, Andreas W. W. Ludwig, Matthias Troyer, Alexei Kitaev, Zhenghan Wang, and Michael H. Freedman. Interacting anyons in topological quantum liquids: The golden chain. *Phys. Rev. Lett.*, 98:160409, Apr 2007.

[186] Anders W. Sandvik, Adolfo Avella, and Ferdinando Mancini. Computational studies of quantum spin systems. In *AIP Conference Proceedings*. AIP, 2010.

[187] Jung-Hoon Jung and Jae Dong Noh. Guide to exact diagonalization study of quantum thermalization. *Journal of the Korean Physical Society*, 76(8):670–683, April 2020.

[188] Cheng-Ju Lin and Olexei I. Motrunich. Exact quantum many-body scar states in the Rydberg-blockaded atom chain. *Phys. Rev. Lett.*, 122:173401, Apr 2019.

[189] Keita Omiya and Markus Müller. Quantum many-body scars in bipartite Rydberg arrays originating from hidden projector embedding. *Phys. Rev. A*, 107:023318, Feb 2023.

[190] Cheng-Ju Lin, Anushya Chandran, and Olexei I. Motrunich. Slow thermalization of exact quantum many-body scar states under perturbations. *Phys. Rev. Research*, 2:033044, Jul 2020.

[191] Ian Mondragon-Shem, Maxim G. Vavilov, and Ivar Martin. Fate of quantum many-body scars in the presence of disorder. *PRX Quantum*, 2:030349, Sep 2021.

[192] Marko Ljubotina, Jean-Yves Desaules, Maksym Serbyn, and Zlatko Papić. Superdiffusive Energy Transport in Kinetically Constrained Models. *Phys. Rev. X*, 13:011033, Mar 2023.

[193] Subir Sachdev, K. Sengupta, and S. M. Girvin. Mott insulators in strong electric fields. *Phys. Rev. B*, 66:075128, Aug 2002.

[194] T. M. R. Byrnes, P. Sriganesh, R. J. Bursill, and C. J. Hamer. Density matrix renormalization group approach to the massive Schwinger model. *Phys. Rev. D*, 66:013002, Jul 2002.

[195] E. Rico, T. Pichler, M. Dalmonte, P. Zoller, and S. Montangero. Tensor Networks for Lattice Gauge Theories and Atomic Quantum Simulation. *Phys. Rev. Lett.*, 112:201601, May 2014.

[196] Bing Yang, Hui Sun, Robert Ott, Han-Yi Wang, Torsten V. Zache, Jad C. Halimeh, Zhen-Sheng Yuan, Philipp Hauke, and Jian-Wei Pan. Observation of gauge invariance in a 71-site Bose–Hubbard quantum simulator. *Nature*, 587(7834):392–396, Nov 2020.

[197] Maarten Van Damme, Jad C. Halimeh, and Philipp Hauke. Gauge-symmetry violation quantum phase transition in lattice gauge theories. *arXiv e-print*, 2020.

[198] Sidney Coleman. More about the massive Schwinger model. *Annals of Physics*, 101(1):239–267, 1976.

[199] Federica M. Surace, Paolo P. Mazza, Giuliano Giudici, Alessio Lerose, Andrea Gambassi, and Marcello Dalmonte. Lattice gauge theories and string dynamics in Rydberg atom quantum simulators. *Phys. Rev. X*, 10:021041, May 2020.

[200] Sho Sugiura, Tomotaka Kuwahara, and Keiji Saito. Many-body scar state intrinsic to periodically driven system. *Phys. Rev. Research*, 3:L012010, Feb 2021.

[201] Bhaskar Mukherjee, Sourav Nandy, Arnab Sen, Diptiman Sen, and K. Sengupta. Collapse and revival of quantum many-body scars via Floquet engineering. *Phys. Rev. B*, 101:245107, Jun 2020.

[202] Bhaskar Mukherjee, Arnab Sen, Diptiman Sen, and K. Sengupta. Dynamics of the vacuum state in a periodically driven Rydberg chain. *Phys. Rev. B*, 102:075123, Aug 2020.

[203] Kaoru Mizuta, Kazuaki Takasan, and Norio Kawakami. Exact Floquet quantum many-body scars under Rydberg blockade. *Phys. Rev. Research*, 2:033284, Aug 2020.

[204] N. Maskara, A. A. Michailidis, W. W. Ho, D. Bluvstein, S. Choi, M. D. Lukin, and M. Serbyn. Discrete time-crystalline order enabled by quantum many-body scars: Entanglement steering via periodic driving. *Phys. Rev. Lett.*, 127:090602, Aug 2021.

[205] Pierre-Gabriel Rozon, Michael J. Gullans, and Kartiek Agarwal. Constructing quantum many-body scar Hamiltonians from Floquet automata. *Phys. Rev. B*, 106:184304, Nov 2022.

[206] Han-Yi Wang, Wei-Yong Zhang, Zhiyuan Yao, Ying Liu, Zi-Hang Zhu, Yong-Guang Zheng, Xuan-Kai Wang, Hui Zhai, Zhen-Sheng Yuan, and Jian-Wei Pan. Interrelated thermalization and quantum criticality in a lattice gauge simulator. *Phys. Rev. Lett.*, 131:050401, Aug 2023.

[207] Cheng Peng and Xiaoling Cui. Bridging quantum many-body scars and quantum integrability in Ising chains with transverse and longitudinal fields. *Phys. Rev. B*, 106:214311, Dec 2022.

[208] E.J. Heller. *The Semiclassical Way to Dynamics and Spectroscopy*. Princeton University Press, 2018.

[209] E. J. Heller. Wavepacket dynamics and quantum chaology. In *Chaos and quantum physics*, volume 52. North-Holland: Amsterdam, 1991.

[210] P. A. M. Dirac. Note on exchange phenomena in the Thomas atom. *Mathematical Proceedings of the Cambridge Philosophical Society*, 26(3):376–385, 1930.

[211] P. Kramer and M. Saraceno. *Geometry of the Time-Dependent Variational Principle in Quantum Mechanics*. Lecture Notes in Physics. Springer Berlin Heidelberg, 1981.

[212] Jutho Haegeman, J. Ignacio Cirac, Tobias J. Osborne, Iztok Pižorn, Henri Verschelde, and Frank Verstraete. Time-dependent variational principle for quantum lattices. *Phys. Rev. Lett.*, 107:070601, Aug 2011.

[213] Wen Wei Ho, Soonwon Choi, Hannes Pichler, and Mikhail D. Lukin. Periodic orbits, entanglement, and quantum many-body scars in constrained models: Matrix product state approach. *Phys. Rev. Lett.*, 122:040603, Jan 2019.

[214] A. A. Michailidis, C. J. Turner, Z. Papić, D. A. Abanin, and M. Serbyn. Slow quantum thermalization and many-body revivals from mixed phase space. *Phys. Rev. X*, 10:011055, Mar 2020.

[215] C. J. Turner, J.-Y. Desaules, K. Bull, and Z. Papić. Correspondence principle for many-body scars in ultracold Rydberg atoms. *Phys. Rev. X*, 11:021021, Apr 2021.

[216] Alexios A. Michailidis, Marko Žnidarič, Mariya Medvedyeva, Dmitry A. Abanin, Tomaž Prosen, and Z. Papić. Slow dynamics in translation-invariant quantum lattice models. *Phys. Rev. B*, 97:104307, Mar 2018.

[217] Luca D'Alessio, Yariv Kafri, Anatoli Polkovnikov, and Marcos Rigol. From quantum chaos and eigenstate thermalization to statistical mechanics and thermodynamics. *Advances in Physics*, 65(3):239, 2016.

[218] Jutho Haegeman, Christian Lubich, Ivan Oseledets, Bart Vandereycken, and Frank Verstraete. Unifying time evolution and optimization with matrix product states. *Phys. Rev. B*, 94:165116, Oct 2016.

[219] David Pérez-García, Frank Verstraete, Michael M. Wolf, and J. Ignacio Cirac. Matrix product state representations. *Quantum Inf. Comput.*, 7(5):401–430, 2007.

[220] Aiden Daniel, Andrew Hallam, Jean-Yves Desaules, Ana Hudomal, Guo-Xian Su, Jad C. Halimeh, and Zlatko Papić. Bridging quantum criticality via many-body scarring. *Physical Review B*, 107(23), June 2023.

[221] Shane P. Kelly, Eddy Timmermans, and S.-W. Tsai. Thermalization and its breakdown for a large nonlinear spin. *Phys. Rev. A*, 102:052210, Nov 2020.

[222] M. R. Lambert, Shan-Wen Tsai, and Shane P. Kelly. Quantum memory at an eigenstate phase transition in a weakly chaotic model. *Phys. Rev. A*, 106:012206, Jul 2022.

[223] Pasquale Calabrese and John Cardy. Entanglement entropy and quantum field theory. *Journal of Statistical Mechanics: Theory and Experiment*, 2004(06):P06002, 2004.

[224] Thomas Iadecola, Michael Schecter, and Shenglong Xu. Quantum many-body scars from magnon condensation. *Phys. Rev. B*, 100:184312, Nov 2019.

[225] Cheng-Ju Lin and Olexei I. Motrunich. Quasiparticle explanation of the weak-thermalization regime under quench in a nonintegrable quantum spin chain. *Phys. Rev. A*, 95:023621, Feb 2017.

[226] Shane Dooley. Robust quantum sensing in strongly interacting systems with many-body scars. *PRX Quantum*, 2:020330, May 2021.

[227] Jean-Yves Desaules, Francesca Pietracaprina, Zlatko Papić, John Goold, and Silvia Pappalardi. Extensive multipartite entanglement from su(2) quantum many-body scars. *Phys. Rev. Lett.*, 129:020601, Jul 2022.

[228] Shane Dooley, Silvia Pappalardi, and John Goold. Entanglement enhanced metrology with quantum many-body scars. *Phys. Rev. B*, 107:035123, Jan 2023.

[229] G. C. Wick. The evaluation of the collision matrix. *Phys. Rev.*, 80:268–272, Oct 1950.

[230] Marek Gluza, Thomas Schweigler, Mohammadamin Tajik, João Sabino, Federica Cataldini, Frederik S. Møller, Si-Cong Ji, Bernhard Rauer, Jörg Schmiedmayer, Jens Eisert, and Spyros Sotiriadis. Mechanisms for the emergence of Gaussian correlations. *SciPost Phys.*, 12:113, 2022.

[231] Thomas Schweigler, Marek Gluza, Mohammadamin Tajik, Spyros Sotiriadis, Federica Cataldini, Si-Cong Ji, Frederik S. Møller, João Sabino, Bernhard Rauer, Jens Eisert, and Jörg Schmiedmayer. Decay and recurrence of non-Gaussian correlations in a quantum many-body system. *Nature Physics*, 17(5):559–563, May 2021.

[232] Michael E. Peskin and Daniel V. Schroeder. *An Introduction to quantum field theory*. Addison-Wesley, Reading, USA, 1995.

[233] M. Cramer, C. M. Dawson, J. Eisert, and T. J. Osborne. Exact relaxation in a class of nonequilibrium quantum lattice systems. *Phys. Rev. Lett.*, 100:030602, Jan 2008.

[234] M Cramer and J Eisert. A quantum central limit theorem for non-equilibrium systems: exact local relaxation of correlated states. *New Journal of Physics*, 12(5):055020, may 2010.

[235] Anatoli Polkovnikov, Krishnendu Sengupta, Alessandro Silva, and Mukund Vengalattore. Colloquium: Nonequilibrium dynamics of closed interacting quantum systems. *Rev. Mod. Phys.*, 83:863–883, Aug 2011.

[236] Antoine Browaeys and Thierry Lahaye. Many-body physics with individually controlled Rydberg atoms. *Nature Physics*, 16(2):132–142, Feb 2020.

[237] Rhine Samajdar, Soonwon Choi, Hannes Pichler, Mikhail D. Lukin, and Subir Sachdev. Numerical study of the chiral $\mathbb{Z}_3$ quantum phase transition in one spatial dimension. *Phys. Rev. A*, 98:023614, Aug 2018.

[238] Michael Rader and Andreas M. Lauchli. Floating phases in one-dimensional rydberg ising chains. *arXiv e-print*, 2019.

[239] Natalia Chepiga and Frédéric Mila. Floating phase versus chiral transition in a 1d hard-boson model. *Phys. Rev. Lett.*, 122:017205, Jan 2019.

[240] R J Baxter. Hard hexagons: exact solution. *Journal of Physics A: Mathematical and General*, 13(3):L61, mar 1980.

[241] Kevin Slagle, David Aasen, Hannes Pichler, Roger S. K. Mong, Paul Fendley, Xie Chen, Manuel Endres, and Jason Alicea. Microscopic characterization of ising conformal field theory in rydberg chains. *Phys. Rev. B*, 104:235109, Dec 2021.

[242] Christopher J. Turner, Konstantinos Meichanetzidis, Zlatko Papić, and Jiannis K. Pachos. Optimal free descriptions of many-body theories. *Nature Communications*, 8(1):14926, 2017.

[243] Jiannis K. Pachos and Zlatko Papic. Quantifying the effect of interactions in quantum many-body systems. *SciPost Phys. Lect. Notes*, page 4, 2018.

[244] Gabriel Matos, Andrew Hallam, Aydin Deger, Zlatko Papić, and Jiannis K. Pachos. Emergence of gaussianity in the thermodynamic limit of interacting fermions. *Phys. Rev. B*, 104:L180408, Nov 2021.

[245] Jiannis K. Pachos and Chrysoula Vlachou. Quantifying fermionic interactions from the violation of Wick's theorem. *Quantum*, 6:840, October 2022.

[246] Interaction Distance: A New Way of Studying Strongly Correlated Systems . `https://theory.leeds.ac.uk/interaction-distance/`.

[247] Konstantinos Meichanetzidis, Christopher J. Turner, Ashk Farjami, Zlatko Papić, and Jiannis K. Pachos. Free-fermion descriptions of parafermion chains and string-net models. *Phys. Rev. B*, 97:125104, Mar 2018.

[248] Hui Li and F. D. M. Haldane. Entanglement spectrum as a generalization of entanglement entropy: Identification of topological order in non-abelian fractional quantum Hall effect states. *Phys. Rev. Lett.*, 101:010504, Jul 2008.

[249] Ingo Peschel. Calculation of reduced density matrices from correlation functions. *Journal of Physics A: Mathematical and General*, 36(14):L205, 2003.

[250] Masahito Ueda. Quantum equilibration, thermalization and prethermalization in ultracold atoms. *Nature Reviews Physics*, 2(12):669–681, Dec 2020.

[251] Immanuel Bloch, Jean Dalibard, and Wilhelm Zwerger. Many-body physics with ultracold gases. *Rev. Mod. Phys.*, 80:885–964, Jul 2008.

[252] Marton Kormos, Mario Collura, Gabor Takács, and Pasquale Calabrese. Real-time confinement following a quantum quench to a non-integrable model. *Nature Physics*, 13(3):246–249, 2017.

[253] I-Chi Chen and Thomas Iadecola. Emergent symmetries and slow quantum dynamics in a rydberg-atom chain with confinement. *Phys. Rev. B*, 103:214304, Jun 2021.

[254] Igor Lesanovsky. Many-body spin interactions and the ground state of a dense rydberg lattice gas. *Phys. Rev. Lett.*, 106:025301, Jan 2011.

[255] Jonathan Wurtz, Alexei Bylinskii, Boris Braverman, Jesse Amato-Grill, Sergio H. Cantu, Florian Huber, Alexander Lukin, Fangli Liu, Phillip Weinberg, John Long, Sheng-Tao Wang, Nathan Gemelke, and Alexander Keesling. Aquila: Quera's 256-qubit neutral-atom quantum computer, 2023.

[256] Benjamin J. Brown, Daniel Loss, Jiannis K. Pachos, Chris N. Self, and James R. Wootton. Quantum memories at finite temperature. *Rev. Mod. Phys.*, 88:045005, Nov 2016.

[257] Suraj Goel, Matthew Reynolds, Matthew Girling, Will McCutcheon, Saroch Leedumrongwatthanakun, Vatshal Srivastav, David Jennings, Mehul Malik, and Jiannis K. Pachos. Unveiling the non-abelian statistics of $d(s_3)$ anyons via photonic simulation, 2023.

[258] Marko Ljubotina, Barbara Roos, Dmitry A. Abanin, and Maksym Serbyn. Optimal steering of matrix product states and quantum many-body scars. *PRX Quantum*, 3:030343, Sep 2022.

[259] Jie Ren, Andrew Hallam, Lei Ying, and Zlatko Papić. ScarFinder: a detector of optimal scar trajectories in quantum many-body dynamics, 2025.

[260] Berislav Buča. Unified Theory of Local Quantum Many-Body Dynamics: Eigenoperator Thermalization Theorems. *Physical Review X*, 13(3), August 2023.

[261] Narayan Mohanta. Chiral pair density wave as a precursor of the pseudogap in kagome superconductors. *Phys. Rev. B*, 108:L220507, Dec 2023.

[262] Ping Gao and Daniel Louis Jafferis. A Traversable Wormhole Teleportation Protocol in the SYK Model, 2021.

[263] Thomas Schuster, Bryce Kobrin, Ping Gao, Iris Cong, Emil T. Khabiboulline, Norbert M. Linke, Mikhail D. Lukin, Christopher Monroe, Beni Yoshida, and Norman Y. Yao. Many-body quantum teleportation via operator spreading in the traversable wormhole protocol. *Phys. Rev. X*, 12:031013, Jul 2022.

[264] Joseph Lykken, Alexander Zlokapa, Samantha I. Davis, David K. Kolchmeyer, Hartmut Neven, Maria Spiropulu, and QCCFP Collaboration. Long-range wormhole teleportation, 2024.

[265] Piers Coleman. *Introduction to Many-Body Physics*. Cambridge University Press, 2015.

[266] M. Nakahara. *Geometry, Topology and Physics*. Taylor & Francis Group, Abingdon, England, 2nd edition, 2003.

[267] Max Bañados and Ignacio Reyes. A short review on Noether's theorems, gauge symmetries and boundary terms. *International Journal of Modern Physics D*, 25(10):1630021, August 2016.

[268] P.A.M. Dirac. *Lectures on Quantum Mechanics*. Belfer Graduate School of Science, monograph series. Dover Publications, 2001.

[269] Mark Srednicki. *Quantum Field Theory*. Cambridge University Press, 2007.

[270] J Barcelos-Neto, Ashok Das, and W Scherer. Canonical quantization of constrained systems. *Acta Phys. Polon. B*, 18(4):269, 1987.

[271] H.B. Nielsen and M. Ninomiya. A no-go theorem for regularizing chiral fermions. *Physics Letters B*, 105(2):219–223, 1981.

[272] H.B. Nielsen and M. Ninomiya. Absence of neutrinos on a lattice: (II). Intuitive topological proof. *Nuclear Physics B*, 193(1):173–194, 1981.

[273] Eduardo Fradkin. *Field theories of condensed matter physics*. Cambridge University Press, 2013.

[274] Omri Golan and Ady Stern. Probing topological superconductors with emergent gravity. *Physical Review B*, 98(6), August 2018.

[275] Chang Liu. `REAPERS`: a reasonably performant simulator for qubit systems. `https://github.com/cl91/REAPERS`,, 2024.

[276] Chang Liu. Computing the otoc for the chiral spin model of the black hole. `https://github.com/cl91/otoc-chiral`,, 2024.

[277] Michael Eiermann and Oliver G. Ernst. A restarted krylov subspace method for the evaluation of matrix functions. *SIAM Journal on Numerical Analysis*, 44(6):2481–2504, 2006.

[278] B Kramer and A MacKinnon. Localization: theory and experiment. *Reports on Progress in Physics*, 56(12):1469, dec 1993.

[279] Sebastian Scherg, Thomas Kohlert, Pablo Sala, Frank Pollmann, Bharath Hebbe Madhusudhana, Immanuel Bloch, and Monika Aidelsburger. Observing non-ergodicity due to kinetic constraints in tilted Fermi-Hubbard chains. *Nature Communications*, 12(1):4490, Jul 2021.

[280] Zhao-Yu Zhou, Guo-Xian Su, Jad C. Halimeh, Robert Ott, Hui Sun, Philipp Hauke, Bing Yang, Zhen-Sheng Yuan, Jürgen Berges, and Jian-Wei Pan. Thermalization dynamics of a gauge theory on a quantum simulator. *Science*, 377(6603):311–314, 2022.

[281] Jad C. Halimeh, Ian P. McCulloch, Bing Yang, and Philipp Hauke. Tuning the Topological θ-Angle in Cold-Atom Quantum Simulators of Gauge Theories. *PRX Quantum*, 3:040316, Nov 2022.